

Radon Background Studies for the SuperNEMO Experiment

Fang Xie

A dissertation submitted in partial fulfillment
of the requirements for the degree of
Doctor of Philosophy
of
University College London.

Department of Physics and Astronomy
University College London

10th March 2021

I, Fang Xie, confirm that the work presented in this thesis is my own. Where information has been derived from other sources, I confirm that this has been indicated in the work.

Abstract

SuperNEMO is a neutrinoless double beta decay ($0\nu 2\beta$) experiment, aiming to reach a half-life sensitivity of 10^{26} years corresponding to an effective Majorana neutrino mass of $\langle m_{\beta\beta} \rangle < 40 - 100$ meV. The sensitivity target has posed a significant challenge of radiopurity for both the detector design and the construction process.

One of the major backgrounds of the SuperNEMO detector is due to Radon, of which the decay daughter ^{214}Bi (from ^{222}Rn) presents a major challenge due its high Q_β values and ability to mimic a double beta decay process. Two radon emanation chambers have been built to be used in conjunction with an electrostatic detector to measure the detector components and construction materials. The chambers have been used to carry out ^{222}Rn emanation assays for multiple samples of detector components and materials for the SuperNEMO and LZ experiments with a sensitivity of 0.09 - 0.19 mBq at 90% Confidence Level (C.L.). The ^{222}Rn contamination of the tracker gas is required to be less than 0.15 mBq/m³. This activity is beyond the sensitivity of current best radon detectors. Therefore a “Radon Concentration Line” was designed and built at UCL. This facility can deliver a concentrated gas sample to the detector, and for the SuperNEMO tracker gas it can reach a sensitivity of $< 5 \mu\text{Bq}/\text{m}^3$ (at 90% C.L.). Radon emanation measurements of fully instrumented SuperNEMO tracker sub-modules have been performed showing that the challenging ^{222}Rn background requirements have been met.

The SuperNEMO Demonstrator sensitivity to its radon backgrounds has been studied via Monte Carlo simulations. Using a $1e1\alpha$ event topology it is shown that the ^{214}Bi target contamination originated from ^{222}Rn (4 mBq in the tracker volume of 15 m^3) can be measured with a 5% precision within 12 days of data taking.

Impact Statement

The main impact of this work on the field of physics is the better understanding of the background of the SuperNEMO neutrinoless double beta searching experiment.

The $0\nu2\beta$ is a rare process forbidden by the Standard Model (SM). A $0\nu2\beta$ search experiment can provide a precise measurement of the absolute neutrino mass. It is also a powerful tool to investigate lepton number violation and the only practical way to assess the nature of the neutrinos (either they are Dirac or Majorana particles). It can, therefore, provide unique information about the physics beyond the SM.

To achieve a better sensitivity, the background of the experiment must be minimised and well-studied. One of the major backgrounds of the SuperNEMO detector is due to radon. The UCL radon emanation measurement facility has been developed and used to measure the ultra-low-level radon of the detector components, construction materials and the completed quarter tracker for the SuperNEMO experiment. The results of radon measurements carried out by the author are now used by the SuperNEMO collaboration to build the background model in simulation and analysis. The facility is also used to measure samples for other rare event searching experiment such as LZ. In analysis work of this thesis, the SuperNEMO Demonstrator sensitivity to its radon backgrounds has been studied via Monte Carlo simulations. The author has made some optimisation of analysis cuts which is widely used in the collaboration.

Beyond physics, the ultra-low-level radon measurement technique developed for this project can also be applied to other fields such as environment and geographic research on monitoring the environmental radon contamination and making an earthquake prediction.

Acknowledgements

First and foremost, I would like to express my extreme gratitude to my supervisor, Ruben Saakyan, without whose guidance this thesis would not have been possible. As annoying as it may be, always knowing the answer to any question I might pose, no matter how obscure, is undoubtedly a beneficial trait to have as a supervisor.

Thanks are also owed to the Chinese Scholarship Council for funding my PhD, allowing me to pursue research in a field I love. I hope to give back to society even more than it has invested in me.

Besides, my thanks go to David Waters and Cheryl Patrick, for much constructive help on analysis techniques and radon measurements - I am sure I would have spent a lot more time groping in the dark without this guiding influence. Away from a computer screen and back in the real world, I am indebted to Xin Ran Liu and Derek Attree for their technical expertise and for their patience as I attempted to develop basic engineering skills. Without him, none of the real 'screw-driver' physics in this thesis would have been remotely functional.

I must thank my fellow SuperNEMO collaborators, who made my four years such a pleasure. Many thanks to my fellow PhD students and D109 inhabitants, especially Ashwin Chopra, Vincenzo Monachello, Dan Quill, Ricky Nathvani, David Yallup, Wei Liu and Joanna Huang, without you, the process would have been a painful one. Special thanks to Hiu Fung Wong, for your companionship and helps throughout the four years. You are the best friend I could ask for.

The love and support of my family have always been a comforting presence, not only for this PhD but for my entire life. Thank you, father, I miss you. And dear mamma, thank you for your incredible support, for your care, for the time you dedicated to raising me to the absolute best of your ability, and for your love. This is for you. I love you.

To my sweetheart Ziwen Pan,

I love you for everything, for your unfailing love, for your understanding and for your support through the toughest moments of my life. You are the best thing that has ever happened to me.

Contents

1	Introduction	24
1.0.1	Author's contribution	26
2	Neutrino Phenomenology	28
2.1	Standard Model Neutrinos	28
2.1.1	Discovery of the Neutrino	28
2.1.2	The Standard Model	29
2.1.3	Neutrino Interactions	30
2.1.4	Neutrino Flavours	31
2.2	Neutrino Oscillations	32
2.2.1	Oscillations Phenomenology	33
2.2.2	Oscillations in Matter	36
2.2.3	Oscillations Parameters	36
2.3	Neutrino Mass	37
2.3.1	Dirac Mass	38
2.3.2	Majorana Mass	39

	<i>Contents</i>	10
2.3.3	See-Saw Mechanism	39
2.4	Neutrino Mass Constraints From Experiments	41
2.4.1	Tritium Decay Experiment	41
2.4.2	Cosmology	42
2.4.3	Double Beta Decay	43
2.5	Outstanding Questions	43
2.5.1	Number of Neutrinos	44
2.5.2	Absolute Neutrino Mass	44
2.5.3	Neutrino Mass Ordering	45
2.5.4	CP violation	46
2.5.5	Dirac or Majorana	46
3	Double Beta Decay	48
3.1	Beta Decay	48
3.2	Two Neutrino Double Beta Decay	49
3.3	Neutrinoless Double Beta Decay	51
3.4	Nuclear Matrix Elements	55
3.4.1	Interacting Shell Model	55
3.4.2	Quasiparticle Random Phase Approximation	56
3.4.3	Interacting Boson Model	56
3.4.4	Projected Hartree-Fock-Bogoluibov Method	56

	<i>Contents</i>	11
3.4.5	Energy Density Functional Method	56
3.4.6	Comparison of different NME calculations	57
4	Current Status of Double Decay Experiments	59
4.1	Detector Design Considerations	59
4.1.1	Isotopes	61
4.1.2	Radio-purity	61
4.1.3	Location	63
4.1.4	Shielding	63
4.1.5	Energy Resolution	64
4.2	Detector Technologies of Various $0\nu 2\beta$ Experiments	64
4.2.1	Semiconductor Experiments	64
4.2.2	Scintillator Experiments	67
4.2.3	Bolometer Experiments	70
4.2.4	Time Projection Chamber Experiments	71
4.2.5	Tracker-Calorimeter Experiments	73
4.3	Summary of the Current and Next Generation Experiments	74
5	The SuperNEMO Experiment	76
5.1	SuperNEMO Baseline Design	76
5.2	Source Foil	78
5.3	Tracker	78

	<i>Contents</i>	12
5.4	Calorimeter	79
5.5	Readout Electronics and Data Acquisition System	80
5.6	Shielding	81
5.6.1	Radon Shielding	81
5.6.2	Anti-radon Factory	82
5.6.3	Passive Shielding	82
5.7	General Analysis Techniques	83
5.7.1	The SuperNEMO software	83
5.7.2	Sample Simulation and Reconstruction	85
5.7.3	Alpha Finder	91
6	Radon and SuperNEMO Sensitivity	95
6.1	The SuperNEMO Backgrounds	95
6.1.1	Internal Background	96
6.1.2	External Background	96
6.1.3	Radon Background	98
6.2	The Property of Radon	98
6.3	Radon in SuperNEMO	101
6.4	Gas Flow Suppression of Radon in Tracker	101
7	Radon Detection	105
7.1	Electrostatic Detector	105

	<i>Contents</i>	13
7.1.1	Detector Signal	107
7.1.2	Detector Efficiency Calibration	107
7.1.3	Detector Background and Anti-Radon Bag	111
7.1.4	Analysis Method	115
7.2	Sensitivity of the Radon Detector	116
7.2.1	Normal Approximation	118
7.2.2	Detector Sensitivity	120
7.3	Emanation Chambers	122
7.3.1	Background of the Emanation Chambers	124
7.3.2	Radon Harboursing Hypothesis	126
7.4	Radon Concentration Line	126
7.4.1	Setup of the RnCL	128
7.4.2	Calibration	129
7.4.3	Sensitivity of RnCL	132
7.5	J-trap	134
8	Radon Emanation Measurements	137
8.1	Sample Measurements	137
8.1.1	Feedthrough Emanation Measurements	138
8.1.2	A List of Sample Emanation Measurements	139
8.2	Gas System Measurement	140

- 8.2.1 Removing Ethanol 141
- 8.2.2 Flowthrough Measurement 142
- 8.2.3 Spike Measurement 143
- 8.2.4 RnCL Measurement 145
- 8.3 Quarter Tracker (the C-Section) Measurements 147
 - 8.3.1 Measurement Starting Point 148
 - 8.3.2 Anti-radon Tent 150
 - 8.3.3 Procedures of the C-Section Measurement 150
 - 8.3.4 C-Section Activity Extracting 151
 - 8.3.5 C-Section Measurement Results 152

9 SuperNEMO Demonstrator Sensitivity to Radon Background Measurement 154

- 9.1 Radon as SuperNEMO Background 155
- 9.2 Radon Background Sensitivity Estimation 156
 - 9.2.1 Event Topology 156
 - 9.2.2 Event Number Estimation 158
 - 9.2.3 Activity 158
 - 9.2.4 Samples 159
 - 9.2.5 Alpha Track Length Distribution 160
 - 9.2.6 Pseudo-experiments 164
 - 9.2.7 Activity Measurement 165

<i>Contents</i>	15
-----------------	----

9.2.8 Sensitivity Dependence on the Exposure Time	165
---	-----

10 Conclusions	168
-----------------------	------------

Bibliography	171
---------------------	------------

List of Figures

2.1	The Standard Model of elementary particles	30
2.2	Two charged current and two neutral current neutrino interactions via which it is possible to detect neutrinos	31
2.3	Combined LEP cross-section measurements for $e^+e^- \rightarrow hadrons$ around the Z^0 resonance	32
2.4	Sample spectrum for tritium decay	42
2.5	Normal and inverted mass ordering of absolute neutrino masses . .	45
2.6	The effective Majorana mass $\langle m_{\beta\beta} \rangle$ as a function of the lightest neutrino mass m_{light}	46
3.1	Predictions of the SEMF for an even value of A	50
3.2	Feynman diagram for $2\nu 2\beta$	50
3.3	Feynman diagram from $0\nu 2\beta$ for the neutrino mass mechanism . .	53
3.4	Distribution of the sum of electron energies for $2\nu 2\beta$ and $0\nu 2\beta$. . .	53
3.5	Feynman diagram from $0\nu 2\beta$ using a right handed weak current . .	54
3.6	Angular and energy distributions for the mass mechanism and right-handed currents decay modes	54

3.7	$0\nu 2\beta$ NME for the neutrino mass mechanism, calculated with five different approaches	58
4.1	A list of the world major underground laboratories	63
4.2	Energy spectrum showing the results from KamLAND-Zen	68
5.1	Exploded view of the SuperNEMO demonstrator	77
5.2	Sketch of a tracker Geiger cell from transverse view	79
5.3	Tracker construction	79
5.4	An optical module of the calorimeter	80
5.5	Schematic of the SuperNEMO readout electronics	81
5.6	SuperNEMO demonstrator module in the Anti - Radon tent and all external shielding	83
5.7	Visualisation of a simulated $2\nu 2\beta$ event in the SuperNEMO demonstrator from the top view	86
5.8	Visualisation of $2\nu 2\beta$ event from the top view, with information from the Calibrated Data bank	87
5.9	SuperNEMO software pipeline	88
5.10	Visualisation of a $2\nu 2\beta$ event from the top view, with information from the Tracker Clustering Data bank	88
5.11	Visualisation of a $2\nu 2\beta$ event from the top view, with information from the Track Trajectory Data bank	89
5.12	Visualisation of a $2\nu 2\beta$ event from the top view, with information from the Particle Track Data bank	90

5.13 A sketch of particle topologies in the SuperNEMO detector 92

5.14 Visualisation of a $1e1\alpha$ event where the α hits 3 tracker cells 93

5.15 Visualisation of a $1e1\alpha$ event where the α hits 2 tracker cells 94

5.16 Visualisation of a $1e1\alpha$ event where the α hits only one tracker cells 94

6.1 Three dominant processes via the β -decay isotope contamination
in the source foil 97

6.2 Three dominant processes of production of two electrons from an
external particle interacting with the source foil 97

6.3 Decay chain of ^{238}U and ^{232}Th 99

6.4 The simplified decay scheme for the decay of ^{214}Bi 99

6.5 The simplified decay scheme for the decay of ^{208}Tl 100

6.6 SuperNEMO sensitivity as a function of exposure for different
radon activities inside the tracker 102

6.7 The radon suppression factor as a function of gas flow rate 104

7.1 The electrostatic detector and its schematic 106

7.2 Response of the DAQ system for various input frequencies 108

7.3 The energy spectrum during the detector detection efficiency cal-
ibration run 109

7.4 Event rates of ^{214}Po and ^{218}Po during the spike method detector de-
tection efficiency calibration run 110

7.5 The energy spectrum during a typical low-activity measurement . . 111

7.6	Event rates of ^{214}Po and ^{218}Po during a typical detector background run	112
7.7	Electrostatic detector background (left). B is the background rate in the detector. The environmental radon level measured by RAD7 during the last six days (right). A is the detected radon progeny (^{214}Po) activity in RAD7.	114
7.8	Radon detector housed in the anti-radon bag	114
7.9	The four types of events identified at the filtering stage	116
7.10	A typical signal event (black) with the pulse fitting function (red) superimposed	117
7.11	Probability distributions for signal and signal-and-background hypotheses	118
7.12	Activities of different isotopes in the ^{222}Rn decay chain with respect to time after introducing 1 mBq of ^{222}Rn into a detector with 0.1 mBq background	121
7.13	MDA for the electrostatic detector as a function of the measurement time	122
7.14	The second emanation chamber fully assembled at MSSL	123
7.15	Schematic of the gas line with the emanation chamber connected	123
7.16	Event rates of ^{214}Po and ^{218}Po during the background measurement of the second chamber	125
7.17	Three Black Mamba Measurement Results	127
7.18	The setup of Radon Concentration Line in real-life	129

7.19 Schematic diagram of the setup during a flowthrough calibration of the RnC 131

7.20 Typical ^{214}Po rates measured in the detector during the trapping stage of the RnCL flowthrough calibration measurement 131

7.21 Typical ^{214}Po rates measured in the detector during the trapping and transfer stage of the RnCL flowthrough calibration measurement 132

7.22 Radon activity inside the carbon trap during the flowthrough calibration of RnCL 133

7.23 Calibration results of trapping efficiency and the trapping and transfer efficiency (blue) of the RnCL 133

7.24 The Sensitivity (MDA) of RnCL for the C-Section measurement . . . 134

7.25 The schematic of the J-trap developed at CPPM 135

8.1 The insertion of feedthroughs into the emanation chamber 138

8.2 Event rates of ^{214}Po during the first feedthrough radon emanation measurement 139

8.3 Event rates of ^{214}Po during the second feedthrough radon emanation measurement 140

8.4 The gas system in real-life 141

8.5 Event rates of ^{214}Po during the radon emanation measurement of the gas system using the flowthrough method 143

8.6 Event rates of ^{214}Po and ^{218}Po during the spike method radon emanation measurement of the gas system 144

8.7 The system setup for the RnCL method measurement of the gas system 145

8.8	A C-Section (quarter tracker) under construction in the cleanroom lab at MSSL	147
8.9	Activity inside the C-Section whilst flushing at 14 lpm prior to the radon measurement	149
8.10	C2 in the annti-radon tent during the measurement	150
8.11	Results from the radon emanation measurements of the completed C2	152
9.1	Beta decay of ^{214}Bi and ^{208}Tl	155
9.2	An event on the first layer of tracker was extrapolated to the foil during reconstruction	157
9.3	The alpha track length distributions of three components	164
9.4	Fit of a pseudo-experiment	165
9.5	Distribution of the ^{214}Bi activities	166
9.6	Relative error on the radon content measurement in the Super-NEMO tracker as a function of the exposure (measurement time) using $1e1\alpha$ channel for the case of a 25 Gauss magnetic field	167
9.7	Relative error on the radon content measurement in the Super-NEMO tracker as a function of the exposure (measurement time) using $1e1\alpha$ channel for the case of no magnetic field	167

List of Tables

2.1	Current best estimates for neutrino mixing parameters from a global fit	37
2.2	Experiments contributing to the present determination of the oscillation parameters	37
2.3	Unknown properties of the neutrino that can be observed using the four main experimental technique	44
4.1	Details of isotopes commonly used in $0\nu 2\beta$ experiments	62
4.2	Summary of current $0\nu 2\beta$ experiments	74
4.3	Summary of future $0\nu 2\beta$ experiments	75
7.1	The results of the last three spike method detection efficiency calibrations	109
7.2	Electrostatic radon detector detection efficiency calibration results using different carrier gases	111
7.3	Measurements of gas cylinders of helium and nitrogen	136

8.1	The results of radon emanation measurements from detector components and construction materials of SuperNEMO and the LZ experiment	140
8.2	Summary of C-Section Measurement result	153
9.1	^{214}Bi and ^{208}Tl activities in the detector region	159
9.2	$1e1\alpha$ channel cut flow of the selection efficiency for 25 Gauss magnetic field Tracker ^{214}Bi from source bulk	161
9.3	$1e1\alpha$ channel cut flow of the selection efficiency for 25 Gauss magnetic field Tracker ^{214}Bi from source surface	161
9.4	$1e1\alpha$ channel cut flow of the selection efficiency for 25 Gauss magnetic field Tracker ^{214}Bi from field wire surface	162
9.5	$1e1\alpha$ channel cut flow of the selection efficiency for no magnetic field Tracker ^{214}Bi from source bulk	162
9.6	$1e1\alpha$ channel cut flow of the selection efficiency for no magnetic field Tracker ^{214}Bi from source surface	163
9.7	$1e1\alpha$ channel cut flow of the selection efficiency for no magnetic field Tracker ^{214}Bi from field wire surface	163

Chapter 1

Introduction

For many years, the Standard Model (SM) of particle physics has been the most successful theory of elementary particle physics and tested precisely. The discovery of Higgs Boson has further validated it.

However, in the neutrino sector, many repeated experimental observations of neutrino oscillations, where neutrinos change from one flavour to another, indicate that the SM can not tell the full story. The flavour mixing and the associated non-zero mass is not unambiguously incorporated in the SM, thus leading to physics beyond the SM. Neutrino oscillation experiments cannot answer all the questions about the properties of neutrinos, such as the absolute mass and the origin of the neutrino mass.

Neutrinos can be either Dirac or Majorana fermions due to neutrinos carrying no electric charge. If neutrinos are Dirac particles, their anti-particles would be distinctive; however, if neutrinos are Majorana particles, they would be the anti-particles of themselves. Neutrinoless double beta decay ($0\nu 2\beta$) is the only practical way of studying neutrinos' Dirac or Majorana nature. In this hypothesised process, two double beta decays happen simultaneously, emitting two electrons without accompanying neutrinos; thus, it is forbidden in the SM due to lepton number violation. The observation of the process can confirm neutrinos are Majorana particles, and its decay rate can be used to extract the absolute mass

(model dependent) of neutrino.

The SuperNEMO experiment is an ultra-low-background tracker-calorimeter experiment designed to search for $(0\nu 2\beta)$ decay of various isotopes with a capability to reach half-life sensitivity of 10^{26} years corresponding to an effective Majorana neutrino mass of $\langle m_{\beta\beta} \rangle < 40 - 100$ meV.

This design allows one to measure the energy of the particles with the calorimeter, as well as to reconstruct the trajectory of the charged particles with the tracker. This unique technique provides a powerful background rejection through the 3D topology of each event. In addition, it can shed light on the mechanism behind lepton number violation in $0\nu 2\beta$ due to its unique ability to provide information on the individual electrons' energy spectra and their angular distribution. The first module, SuperNEMO Demonstrator, contains 7 kg of source isotope ^{82}Se . Other isotopes, such as ^{100}Mo , are also considered for the future. Importantly, because the source and the detector are separated, this technology allows many different isotopes to be investigated.

The background is one of the main concerns for a rare events search experiment, such as searching for the $0\nu 2\beta$ decay. Radon as a radioactive gas from the Uranium (U) and Thorium (Th) decay series, can enter the detector by diffusion, emanation, and contamination, and thus provide a significant background to searching for the $0\nu 2\beta$ decay as their progenies ^{214}Bi and ^{208}Tl undergo β decays with high Q_β values, that are sufficiently large to mimic a $0\nu 2\beta$ decay.

All detector components and construction materials are screened and selected using techniques such as radon emanation measurement, HPGe gamma ray spectroscopy, and mass spectrometry. This screening can not only help to monitor the radiopurity of the materials but also offer a better understanding of the background contribution from different parts of the detector. The measured activities can be fed into the simulations to estimate the number of expected background events during the measurement.

All rare-event searching experiments, including double beta decay and direct dark matter searching experiments require such techniques. The SuperNEMO experiment is aiming to achieve a zero background regime in the region of interest, which requires the radon level inside the detector need to be less than 150 mBq/m³. To address these challenges a dedicated radon detector and a radon concentration line (RnCL) have been developed and deployed for radiopurity assays at UCL.

The demonstrator sensitivity to its radon background in the tracker has been studied. Analysis tools have been developed to allow the identification of event topologies. Specific topologies and variables are chosen to optimise the measurement of the main background. These variables are used to fit background contributions in a large number of pseudo-experiments in order to estimate the statistical and systematic uncertainties of different exposure times.

1.0.1 Author's contribution

Radon detector:

- Measurements of detector efficiency and background.
- Commissioning of an upgraded Radon detector.
- Reducing detector background by a factor of 3 with a dedicated system of nitrogen purging.
- Updating and maintaining the data acquisition system.

Radon concentration line:

- Measurements of the trapping and transfer efficiencies of the system.
- Designing a new RnCL to measure radon emanation under cryogenic temperature.

Radon emanation chambers:

- Assembly, test and commissioning of the second radon emanation chamber.
- Measurements of the intrinsic background of the second radon emanation chamber.
- Cross-calibration with other institutions using Viton rings.

Radon measurements:

- The third quarter-sections of the SuperNEMO tracker.
- SuperNEMO gas mixing and delivery system.
- Radon emanation measurements of components and materials for the SuperNEMO and LZ experiments.

Radon background Monte Carlo studies with the SuperNEMO Demonstrator detector:

- Tracker radon background sensitivity estimation via $1e1\alpha$ topology.
- Optimisation of analysis cuts.

Presentation of the collaboration's work at Neutrino2018 (poster), IOP2018 (talk), NuPhys2016 (poster).

Chapter 2

Neutrino Phenomenology

2.1 Standard Model Neutrinos

2.1.1 Discovery of the Neutrino

In 1930, Pauli hypothesised an additional particle named the neutron, as "a desperate remedy" to conserve energy, momentum, and spin [1] to solve the continuous electron energy spectrum of beta decay which was firstly observed in 1914. The particle was renamed as the neutrino by Fermi [2] in 1933 to avoid confusion with a recently discovered particle by Chadwick. Bethe and Peierls expanded Pauli's theory and showed that this new particle interacts very weakly [3]. Due to this property, the existence of the neutrino was not experimentally confirmed for over a quarter-century until 1956 when Reines and Cowan [4] first observed inverse beta decay at the Savannah River nuclear reactor, using two large tanks of water doped with cadmium chloride sandwiched between scintillator tanks, which gave a unique signature of an anti-neutrino interaction.

$$\bar{\nu} + p \rightarrow n + e^+ \tag{2.1}$$

Later in 1959, Davis and Harmer [5] looked for a similar reaction using anti-

neutrinos and found that it does not occur, which indicated that the neutrino and anti-neutrino are different particles.

$$\bar{\nu} + n \rightarrow p + e^{-} \quad (2.2)$$

According to a rule introduced by Konopinski and Mahmoud in 1953 [6], the lepton number for the electron, the muon, the tau, and the neutrino is $L = +1$, and the lepton number for the corresponding antiparticle is $L = -1$. In 1957, Goldhaber's experiment established neutrino helicity [7], resulting in the discovery that neutrinos are left-handed (LH) while anti-neutrinos are right handed (RH). Therefore, two properties can be used to distinguish neutrinos and anti-neutrinos: lepton number and the helicity.

2.1.2 The Standard Model

The Standard Model (SM) of particle physics is a theory describing interactions of all three types of elementary particles, including leptons, quarks, and their mediators, as shown in Figure 2.1. These elementary particles are classified as either fermions or bosons by spin.

Fermions are elementary particles with spin $1/2$. In the SM, there are 12 kinds of fermions, each with an associated antiparticle (see Figure 1.1). According to their interaction, these fermions are composed into two sectors: leptons and quarks, which both can be classified into three generations. All the six leptons interact through the weak force and the three charged leptons, electron, muon and tau, interact through the electromagnetic force as well.

Particles with integer spin are bosons. There are three forces in the SM, and each of them has an associated elementary boson that mediates the interactions: the strong force is mediated by the gluon, the electromagnetic force is mediated by the photon, and the weak force is mediated by W^+ , W^- and Z . The Higgs Boson is a massive boson with no intrinsic spin, which can explain the mass generation

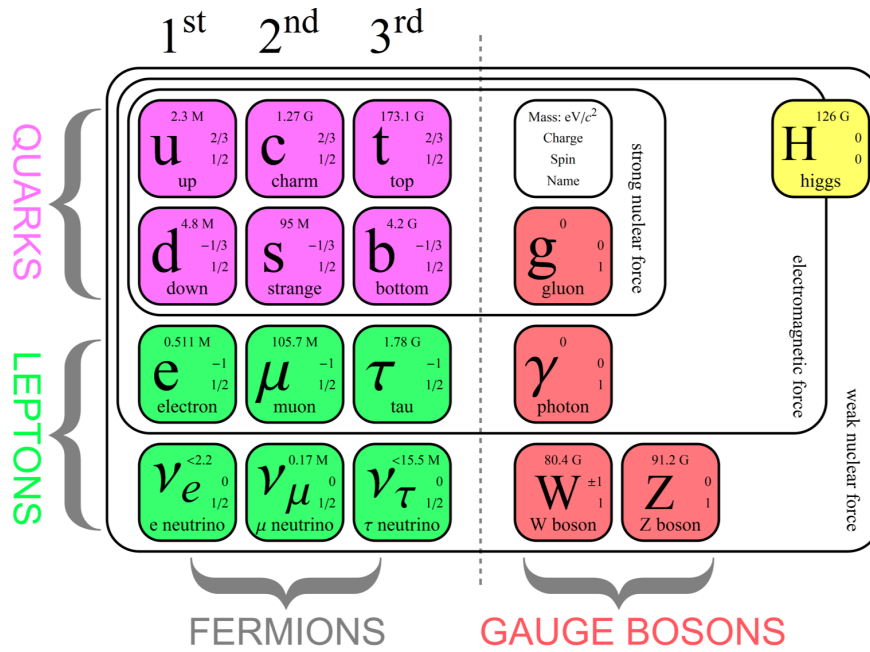


Figure 2.1: The Standard Model of elementary particles [8].

mechanism for bosons and fermions. The confirmation of the existence of Higgs Boson has completed the SM [9].

2.1.3 Neutrino Interactions

In the SM, neutrinos can interact only via the weak force, either through Charged Current (CC) interactions with the exchange of a W^\pm boson, or Neutral Current (NC) interactions involving the exchange of Z^0 boson, as shown in Figure 2.2.

To observe these interactions, considerably large-scale detectors are required as the cross-sections are extremely small. In neutrino detectors, neutrinos scatter off nucleons or atomic electrons, and can therefore be detected through the recoil (or disintegration) of the target. For CC interactions, the outgoing lepton may also be observed, such that the flavour of the incoming neutrino can be determined.

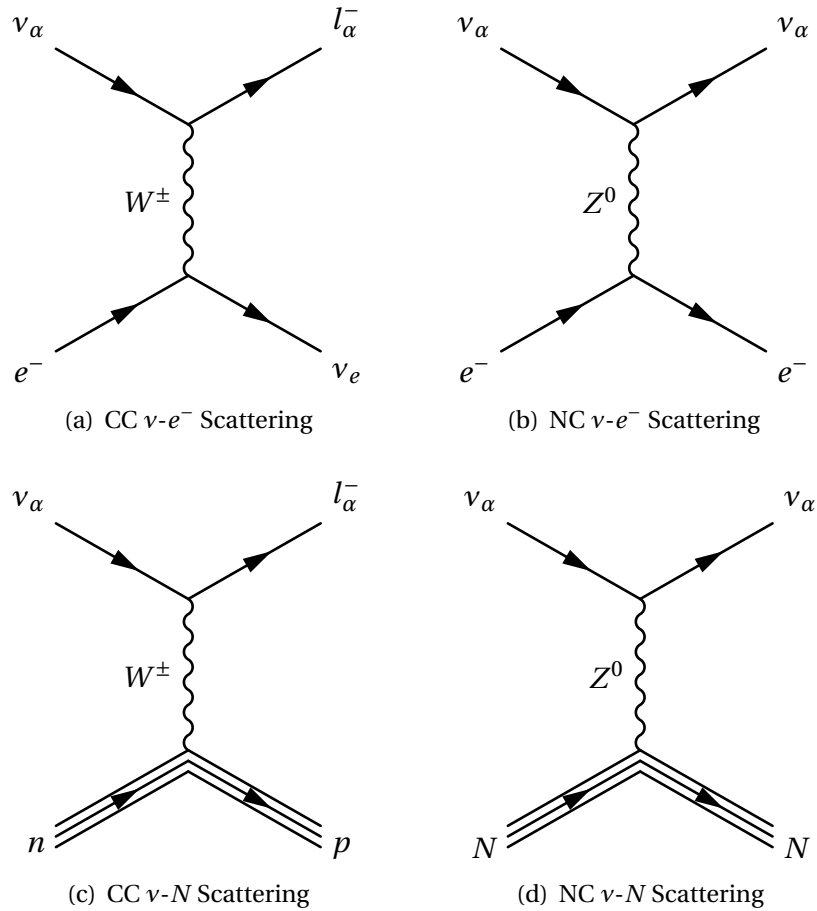


Figure 2.2: Two charged current and two neutral current neutrino interactions via which it is possible to detect neutrinos. l is a lepton, and α is the flavour of the lepton which can be an electron, muon, or tau particle.

2.1.4 Neutrino Flavours

It was first experimentally confirmed that there was more than one flavour of the neutrino in 1962. A research group from Brookhaven National Laboratory observed the unambiguous signature of a CC interaction with an outgoing muon [10]. However, it was not until 2000 when the DOUNT collaboration reported the direct detection of the third flavour of neutrino, ν_τ .

To date, three generations of neutrinos have been directly detected, ν_e , ν_μ and ν_τ , corresponding to three generations of charged leptons e , μ and τ . The number of active light neutrinos has been studied by four experiments at the LEP collider [11]. By measuring the width of Z^0 decay, the combined results from the four

experiments show there are only three generations of neutrinos, as shown in Figure 2.3. However, the study is not sensitive to the sterile neutrinos, which are

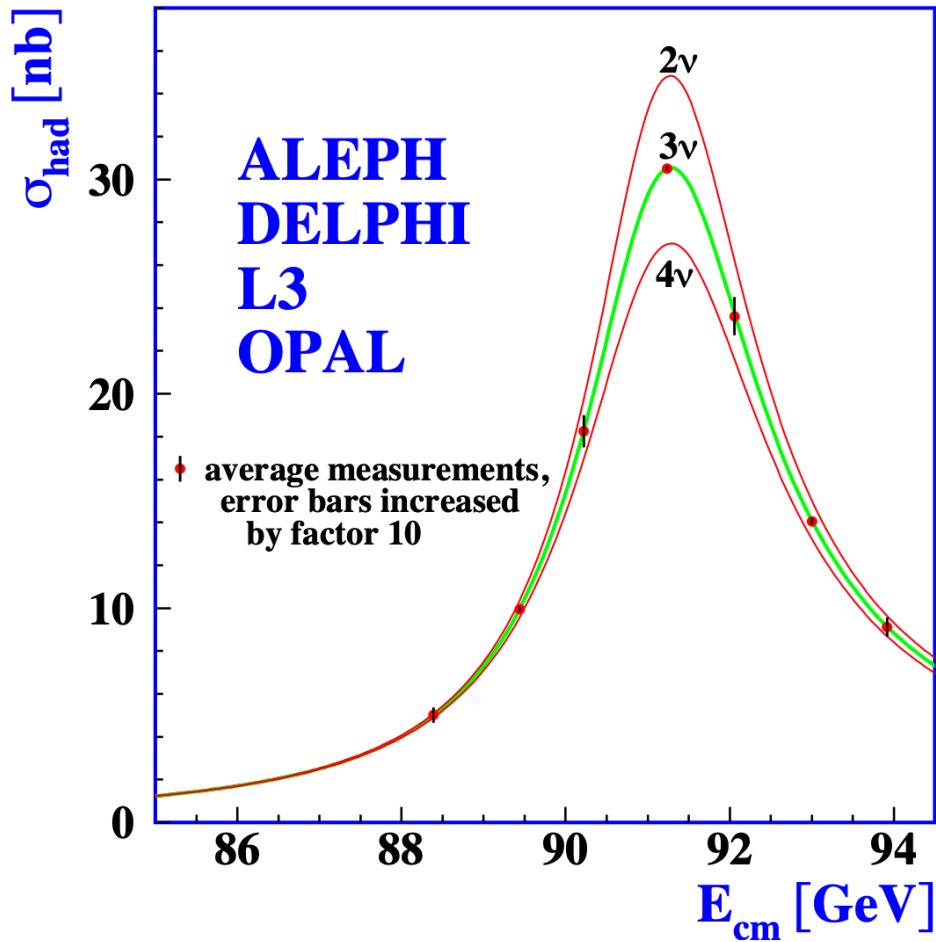


Figure 2.3: Combined LEP cross-section measurements for $e^+e^- \rightarrow \text{hadrons}$ around the Z^0 resonance. $N_\nu = 3$ is clearly favoured [11].

hypothetical particles not included in the SM [11].

2.2 Neutrino Oscillations

Bahcall proposed a complete solar model to quantify the energy radiated from various fusion reactions occurring in the sun, including the energy carried by neutrinos. To validate the solar model proposed by J. Bahcall, the Homestake experiment led by American chemist Ray Davis measured neutrinos from the sun, using 100,000 gallons of cleaning perchloroethylene fluid. The detector was

only sensitive to the CC interaction of electron neutrinos (Figure 2.2(c)). Their first results published in 1968 [12] were surprising in that the number of detected neutrinos were only one-third of the theoretical prediction, which became known as the "solar neutrino problem". In the following 30 years, about 2,000 solar neutrinos have been detected, but the conclusion remained unchanged.

There were many explanations for this, and one of the explanations was that the solar neutrinos oscillate. In this scenario, the ν_e from the sun become ν_μ and ν_τ . However, due to the relatively low energy of solar neutrino, it is not sufficient to produce μ or τ in the final state. Thus the Homestake experiment was only sensitive to ν_e .

The theory was first postulated by Pontecorvo, that neutrinos are not massless and as such could oscillate between different flavours [13, 14]. It was then further extended by Maki, Nakagawa, Sakata in 1962 [15].

It was not until 2001, when the Sudbury Neutrino Observatory (SNO) measured the solar neutrino flux in both the CC and NC channels [16] to obtain evidence of the disappearance of electron neutrinos, that the "solar neutrino problem" was finally solved. Their results showed that the number of detected neutrinos was consistent with Bahcall's solar models. The Kamiokande experiment performed the measurement of the solar neutrino flux independently. It also measured a significantly lower incoming solar neutrino flux, compared to the predicted value [17].

2.2.1 Oscillations Phenomenology

The reason why neutrinos oscillate is that neutrinos produced by weak interactions are not mass eigenstates. For neutrinos, the flavours are ν_e , ν_μ , ν_τ , and the mass eigenstates are ν_1 , ν_2 , ν_3 . The neutrino flavour eigenstate $|\nu_\alpha\rangle$ under weak interaction can be expressed as a linear superposition of the neutrino mass eigenstates $|\nu_i\rangle$. The relationship between them can be described by the

Pontecorvo-Maki-Nakagawa-Sakata (PMNS) matrix, U , which is a unitary matrix similar to the Cabibo-Kobayashi-Masukawa (CKM) matrix for quarks:

$$|\nu_\alpha\rangle = \sum_i U_{\alpha i}^* |\nu_i\rangle, \quad (2.3)$$

$$U = \begin{array}{c} \text{Atmospheric} \\ \left(\begin{array}{ccc} 1 & 0 & 0 \\ 0 & c_{23} & s_{23} \\ 0 & -s_{23} & c_{23} \end{array} \right) \end{array} \begin{array}{c} \text{Cross-mixing} \\ \left(\begin{array}{ccc} c_{13} & 0 & s_{13}e^{-i\delta} \\ 0 & 1 & 0 \\ -s_{13}e^{i\delta} & 0 & c_{13} \end{array} \right) \end{array} \begin{array}{c} \text{Solar} \\ \left(\begin{array}{ccc} c_{12} & s_{12} & 0 \\ -s_{12} & c_{12} & 0 \\ 0 & 0 & 1 \end{array} \right) \end{array} D_M, \quad (2.4)$$

where $c_{ij} \equiv \cos\theta_{ij}$, $s_{ij} \equiv \sin\theta_{ij}$, θ_{ij} is a mixing angle which defines the degree of mixing between mass states i and j , and δ is the CP-violating phase. All mixing angles θ_{ij} have been determined experimentally in the reactor and accelerator experiments. The last measured parameter, θ_{13} , has a non-zero value, thus gives access to the neutrino CP-violating phase.

Furthermore, if the neutrino is a Majorana particle, the additional Majorana CP-violating phases ϕ_1 and ϕ_2 , are included in the diagonal matrix D_M :

$$D_M = \begin{pmatrix} e^{i\phi_1} & 0 & 0 \\ 0 & e^{i\phi_2} & 0 \\ 0 & 0 & 1 \end{pmatrix}. \quad (2.5)$$

The evolution of a mass eigenstate $|\nu_i\rangle$ over space and time obeys the Schrödinger equation, such that, in natural units:

$$|\nu_i(t)\rangle = e^{-i(E_i t - p_i L)} |\nu_i(0)\rangle, \quad (2.6)$$

where t is time, and E_i and p_i refer to the energy and momentum of neutrinos in the lab frame. Assuming that the mass of neutrinos is negligible compared to the

energy, and $t \approx L$:

$$E_i = \sqrt{p_i^2 + m_i^2} = p_i + \frac{m_i^2}{2p_i}, \quad (2.7)$$

and therefore:

$$|\nu_i(t)\rangle \approx e^{-i(m_i^2/2p_i)L} |\nu_i(0)\rangle. \quad (2.8)$$

Considering $E \approx p$ for a relativistic neutrino of flavour, the equation of propagation becomes:

$$|\nu_\alpha(L)\rangle \approx \sum_i U_{\alpha i} e^{-i(m_i^2/2E)L} |\nu_i\rangle = \sum_{i,\beta} U_{\alpha i} U_{\beta i}^* e^{-i(m_i^2/2E)L} |\nu_\beta\rangle. \quad (2.9)$$

If we then consider a neutrino flavour transition from α to β , the transition amplitude can be written in terms of the distance travelled:

$$A(\alpha \rightarrow \beta)(L) = \sum_{i,\beta} U_{\alpha i} U_{\beta i}^* e^{-i(m_i^2/2E)L}. \quad (2.10)$$

Thus the probability of transition can be written as:

$$P(\alpha \rightarrow \beta)(L) = |A(\alpha \rightarrow \beta)(L)|^2 = \left| \sum_{i,\beta} U_{\alpha i} U_{\beta i}^* e^{-i(m_i^2/2E)L} \right|^2. \quad (2.11)$$

Considering a simplified two neutrino case, in a vacuum, the probability of a neutrino changing from flavour α to β is given by:

$$P(\alpha \rightarrow \beta)(L) = \sin^2(2\theta_{ij}) \sin^2\left(\Delta m_{ij}^2 \frac{1.27L}{E}\right), \quad (2.12)$$

where L is in km, E is in GeV, Δm_{ij} is in eV, and Δm_{ij}^2 is the mass mixing splitting between the two neutrino mass eigenstates $|\nu_i\rangle$ and $|\nu_j\rangle$ and is defined as:

$$\Delta m_{ij}^2 \equiv m_i^2 - m_j^2. \quad (2.13)$$

Therefore, the probability of oscillation is determined by the parameters in the PMNS matrix and mass splittings. Since the probability depends only on Δm_{ij}^2 , measuring the oscillations parameters does not give an answer to the absolute neutrino mass.

2.2.2 Oscillations in Matter

All neutrino flavours can interact with matter (protons, neutrons and electrons) through the NC interaction, this is identical for all flavours and so would not affect the oscillation probabilities between them. However, ν_e interact with electrons in matter via the CC interaction, exchanging W^\pm . This effect, known as the Mikheyev-Smirnov-Wolfenstein (MSW) effect, is proportional to the electron density and the energy of the neutrino and modifies the expression for the neutrino oscillation probability [18].

2.2.3 Oscillations Parameters

In the past few decades, flavour oscillations of solar, atmospheric, reactor, and accelerator neutrinos have been studied to determine the value of the PMNS matrices parameters. The latest best-fit limits of the three mixing angles and two mass-squared differences are summarised in Table 2.2.

The neutrino oscillation experiments are only sensitive to the squared mass differences ($\Delta m_{ji}^2 = \Delta m_j^2 - \Delta m_i^2$). Current oscillation experiments have measured two of the squared mass differences, Δm_{21}^2 and Δm_{32}^2 . As a consequence, there are two possible mass ordering status: the normal ordering (NO, $\Delta m_{31}^2 > 0$) and the inverse ordering (IO, $\Delta m_{31}^2 < 0$), see Section 2.5.3. The PMNS mixing matrix also contains at least one CP-violating phase, see Section 2.5.4, and there will be two more if neutrinos are Majorana fermions. The Dirac CP-violating phase can be measured by accelerator experiments or atmospheric experiments.

Parameter	Ordering	Best-fit	3σ range
$\sin^2 \theta_{12}/10^{-1}$	Normal/Inverse	3.10	2.75 - 3.50
$\sin^2 \theta_{23}/10^{-1}$	Normal	5.58	4.27 - 6.09
$\sin^2 \theta_{23}/10^{-1}$	Inverse	5.63	4.30 - 6.12
$\sin^2 \theta_{13}/10^{-2}$	Normal	2.241	2.046 - 2.440
$\sin^2 \theta_{13}/10^{-2}$	Inverse	2.261	2.066 - 2.461
$\Delta m_{21}^2/10^{-5} eV^2$	Normal/Inverse	7.39	6.79 - 8.01
$\Delta m_{32}^2/10^{-3} eV^2$	Normal	2.449	2.358 - 2.544
$\Delta m_{32}^2/10^{-3} eV^2$	Inverse	2.509	2.603 - 2.416

Table 2.1: Current best estimates for neutrino mixing parameters from a global fit [19], Δm^2 defined as $m_3^2 - (m_1^2 + m_2^2)/2$ [20].

Experiment	Dominant	Important
Solar Experiments	θ_{12}	$\Delta m_{21}^2, \theta_{13}$
Reactor long baseline (LBL)	Δm_{21}^2	θ_{12}, θ_{13}
Reactor medium baseline (MBL)	$\Delta m_{31}^2, \Delta m_{32}^2$	
Atmospheric Experiments		$\Delta m_{31}^2, \Delta m_{32}^2, \theta_{13}, \delta_{CP}$
Accel LBL $\nu_\nu, \bar{\nu}_\nu$, Disapp	$\Delta m_{31}^2, \Delta m_{32}^2, \theta_{23}$	
Accel LBL $\nu_e, \bar{\nu}_e$ App	δ_{CP}	θ_{13}, θ_{23}

Table 2.2: Experiments contributing to the present determination of the oscillation parameters [20].

2.3 Neutrino Mass

The observation of the neutrino oscillation has provided clear evidence that neutrinos have non-zero mass. Several attempts on extending the SM to include the neutrino mass have been studied. Two distinct mass terms were considered for addition to the SM, depending on the nature of neutrinos. The first one is the Dirac mass term, where the neutrino is treated as a Dirac particle, the same as other SM fermions. The second is the Majorana mass term, where the neutrino is regarded as its own antiparticle. A combination of both Dirac and Majorana

mass is also considered.

2.3.1 Dirac Mass

In the SM, neutrinos are all LH particles, which interact weakly. To allow a massive neutrino, the RH neutrino can be added to the SM as an extension, which is sterile since experiments show it does not participate in the weak interaction.

Similar to the way that other charged leptons and quarks acquire mass in the SM, via the introduction of the RH field, the Dirac neutrino mass term can be added through the coupling of LH and RH fields with the Higgs field.

Although the minimum extension to the SM is introducing only one RH field, it is more natural to include three RH field singlets $\nu_{e,R}$, $\nu_{\mu,R}$ and $\nu_{\tau,R}$ corresponding the three generations.

The Lagrangian for a massive Dirac neutrino in the simplified, single-flavour case is:

$$\mathcal{L}_D = -\frac{1}{2}m_D(\bar{\nu}_L\nu_R + \bar{\nu}_R\nu_L) + \text{h.c.} \quad (2.14)$$

where m_D is a constant mass term that represents the Yukawa coupling between the neutrino and Higgs fields, and h.c. is the Hermitian conjugate of the first two terms. The neutrino and anti-neutrino fermionic field are both composed of two chiral fields:

$$\nu = \nu_L + \nu_R, \bar{\nu} = \bar{\nu}_L + \bar{\nu}_R. \quad (2.15)$$

Here, neutrinos and anti-neutrinos are fundamentally different particles. This method seems like a small and natural extension to the SM; however, several drawbacks arise. Firstly, it introduces a sterile neutrino which cannot be directly experimentally detected. Secondly, it does not answer why the Higgs-neutrino Yukawa coupling needs to be extremely small. The coupling constant will be $< 10^{-12}$, corresponding to the neutrino mass < 1 eV, which is $> 10^9$ times lower than the coupling constant for τ , and $> 10^6$ times smaller than the one for e .

2.3.2 Majorana Mass

It is possible to form a non-zero mass term by charge-conjugating the RH field and contracting it with itself, as the neutrino is neutral and it does not need to conserve charge. In 1936, Ettore Majorana proposed a new type of mass term, known as Majorana mass [21], in which the two chiral fields ν_L and ν_R are considered to be non-independent. The charge conjugation is the same as the arbitrary phase as:

$$\nu_R^c = C\nu_R \equiv i\gamma^2\nu_R, \quad (2.16)$$

where C is the charge conjugation operator. In the Majorana case, only two of the four components in the Dirac case are needed, and Majorana neutrino is its own anti-neutrino:

$$\nu = \nu_L + \nu_L^C, \nu^C = \nu. \quad (2.17)$$

The Lagrangian for the Majorana neutrino is:

$$\mathcal{L}_M = -\frac{1}{2}m_R\overline{\nu_R^c}\nu_R + \text{h.c.}, \quad (2.18)$$

where m_R is a constant Majorana mass term and h.c. is the Hermitian conjugate. It should be noted that in the Equation 2.18, lepton number is not conserved as the incoming neutrino is destroyed and an outgoing anti-neutrino is created. Thus, the existence of Majorana mass term implies lepton number violation, including neutrinoless double beta decay.

2.3.3 See-Saw Mechanism

It is possible to bring Dirac and Majorana descriptions together to explain the small mass of neutrinos, where the Lagrangian is:

$$\begin{aligned}
\mathcal{L}_{M+D} &= \mathcal{L}_D + \mathcal{L}_M \\
&= -\frac{1}{2}m_D(\overline{\nu}_L\nu_R + \overline{\nu}_R\nu_L) - \frac{1}{2}m_R\overline{\nu}_R^c\nu_R + \text{h.c.} \\
&= -\frac{1}{2}\begin{pmatrix} \overline{\nu}_L & \overline{\nu}_R^c \end{pmatrix} \mathcal{M} \begin{pmatrix} \nu_L^c \\ \nu_R \end{pmatrix} + \text{h.c.},
\end{aligned} \tag{2.19}$$

where \mathcal{M} is given by:

$$\mathcal{M} = \begin{pmatrix} 0 & m_D \\ m_D & m_R \end{pmatrix}. \tag{2.20}$$

It should be noted that the neutrino states in Equation 2.19 are weak eigenstates rather than mass eigenstates which can be found by diagonalising the \mathcal{M} . The eigenvalues of \mathcal{M} can be derived from Equation 2.20:

$$m_{1,2} = \frac{1}{2}m_R \pm \frac{1}{2}\sqrt{m_R^2 + 4m_D^2}. \tag{2.21}$$

Since the SM does not have any requirement on the value of the right-hand Majorana term, m_R can be very large, where $m_R \gg m_D$. In this scenario, the two reduced eigenstates are:

$$\begin{aligned}
m_1 &\approx m_R, \\
m_2 &\approx \frac{m_D^2}{m_R}.
\end{aligned} \tag{2.22}$$

Note that if the neutrino of mass m_1 is heavy, then the mass of the other neutrino m_2 is very light due to the suppression factor $\frac{1}{m_R}$. This is known as the See-Saw Mechanism [22]. It can answer the question of why the neutrino is much lighter than other charged leptons. Assuming that the Dirac mass is ~ 1 GeV, in the same range with the other charged leptons, and the right-hand Majorana mass term is at the scale of Grand Unification Theory ($\sim 10^{15}$ GeV), then the mass of the light neutrino is in the meV scale, as it is observed. The See-Saw Mechanism

introduces a very heavy neutrino, and CP violations in the decay of this heavy neutrino in the early universe could explain the matter-antimatter asymmetry [23].

2.4 Neutrino Mass Constraints From Experiments

There are mainly four types of experiments that offer information about neutrino mass. Tritium Decay, $0\nu\beta\beta$, and cosmological models can measure the absolute neutrino mass, while neutrino oscillation experiments can only measure the squared mass differences. Through the precise measurement of $|\Delta m_{23}^2|$, which is the largest mass splitting, a lower limit on the heaviest neutrino can be set as $> 0.06 \text{ eV} (\sqrt{|\Delta m_{23}^2|})$, since the lightest neutrino cannot be less than zero [24].

2.4.1 Tritium Decay Experiment

Tritium Decay is one of the standard methods to measure the mass of the electron neutrino by measuring the end point of the beta decay spectrum with high energy resolution. The underlying mechanism for this decay is:



The maximum allowable energy for the electron from the decay kinematics, called the end point, is Q_β , and it equals the difference of masses between ${}^3\text{H}$ and ${}^3\text{He} + e^-$ at rest. However, if the neutrino mass has a non-zero value, the curve of the energy spectrum will be affected slightly. In addition, the Q_β will be reduced by the neutrino mass, as shown in Figure 2.4.

This kind of direct measurement is challenging due to the very small neutrino mass. The number of electrons near the end point of the spectrum is small, so the statistical error will be large. As well as this, the energy resolution of the detector should be excellent. However, the advantage of a direct measurement is obvious

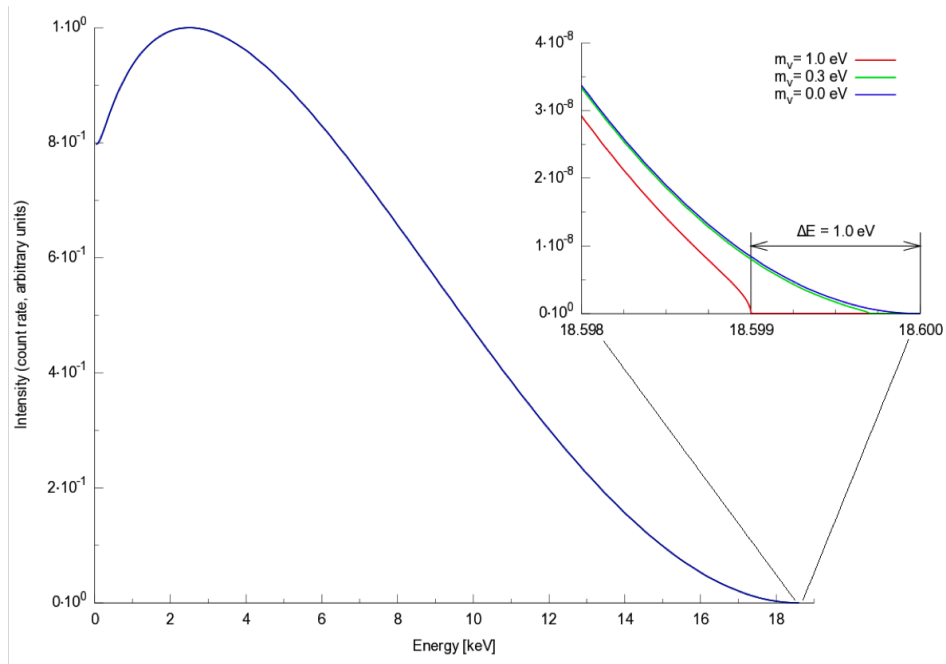


Figure 2.4: Sample spectrum for tritium decay, showing exaggerated distortion in the high energy tail due to a neutrino mass [25]

that it only relies on energy and momentum conservation to extract $\langle m_\beta \rangle$, and thus the result is model independent. The KATRIN experiment, which started data taking in 2018, aims to reach a sensitivity of 200 meV at 90% confidence level (C.L.). It has produced the first result of < 1.1 eV, which improved the previous ^3H constraint by a factor of 2 [26].

2.4.2 Cosmology

The analysis of the cosmic background (CMB) and its anisotropies has also made it possible to constrain the mass of neutrinos. A large number of photons generated in the Big Bang were left behind after the end of the Great Thermal Explosion, which red-shifted and cooled as the universe expanded, forming the Cosmic Microwave Background (CMB) radiation we observe today. Similarly, a large number of neutrinos produced during the Big Bang were also left behind, creating a Cosmic Neutrino Background (CNB). This background has not been detected so far, but it is possible to measure it indirectly using cosmological observa-

tion data. The combined analysis of the anisotropy of the cosmic background (CMB), baryon acoustic oscillations, and large scale structure formation have also made it possible to constrain the mass of neutrinos, although it is heavily dependent on cosmological models. The current best limits are $\sum m_i < 0.11$ eV at 95% C.L. [27].

2.4.3 Double Beta Decay

Double beta decay is a rare process of weak interaction, involving two beta decays in one nucleus at the same time. It occurs only when the single beta decay is forbidden from the energetic point of view. The two-neutrino double beta decay ($2\nu\beta\beta$) is allowed by the SM and has already been observed for several nuclei. However, neutrinoless double beta decay ($0\nu\beta\beta$) is prohibited by the SM because it violates leptonic number conservation. If neutrinos are indeed Majorana particles, $0\nu\beta\beta$ is sensitive to the effective Majorana neutrino mass, $\langle m_{\beta\beta} \rangle$:

$$\langle m_{\beta\beta} \rangle = \left| \sum_i U_{ei}^2 m_i \right|. \quad (2.24)$$

The current best limit of $\langle m_{\beta\beta} \rangle$ is $< 61 - 165$ meV, given by the combined analysis of Kamland-Zen and the EXO experiment in ^{136}Xe [28]. More details about $0\nu\beta\beta$ will be discussed in Chapter 3.

2.5 Outstanding Questions

Since the discovery of neutrino oscillations, significant progress has been made in neutrino physics. However, there are still many outstanding questions left for current and next generation oscillation experiments, double beta decay experiments, cosmology, and beta decay experiments to solve. The unresolved problems of the neutrino and the corresponding experimental techniques for solving these are summarised in Table 2.3.

Property	Oscillation	Cosmology	β -decay	$0\nu\beta\beta$
Number of Neutrinos	✓	✓		
Absolute Mass		✓	✓	✓
Mass Ordering	✓			✓
Dirac or Majorana				✓
Dirac CP-violation	✓			
Majorana CP-violation				✓

Table 2.3: Unknown properties of the neutrino that can be observed using the four main experimental techniques.

2.5.1 Number of Neutrinos

Three generations of light neutrinos (ν_e , ν_μ and ν_τ) have been detected, as discussed in Section 2.1.4. However, there is still the possibility of one or more sterile neutrinos. The results from the short baseline (SBL) experiments such as LSND and MiniBoone show some hints of the existence of an eV-range sterile neutrino and some cosmological results favour the keV-range sterile neutrino. So far, there is no definitive evidence confirming or refuting the existence of sterile neutrino with sufficient confidence, thus it is left to the next generation of short baseline neutrino oscillation experiments to answer [29].

2.5.2 Absolute Neutrino Mass

The current and next generation of direct measurements, such as KATRIN, and cosmology experiments are working on determining the absolute neutrino mass. In the next few years, if the neutrino is Majorana particle, $0\nu\beta\beta$ experiments will also be able to provide information about the neutrino mass down to 30 meV. In the meantime, cosmology, and direct measurement such as KATRIN will continue. An unrealistically large-scale spectrometer would be required to reach a better sensitivity for the KATRIN experiment; thus it will be a real technical challenge to surpass the current limit of 0.2 eV in the near future. There are

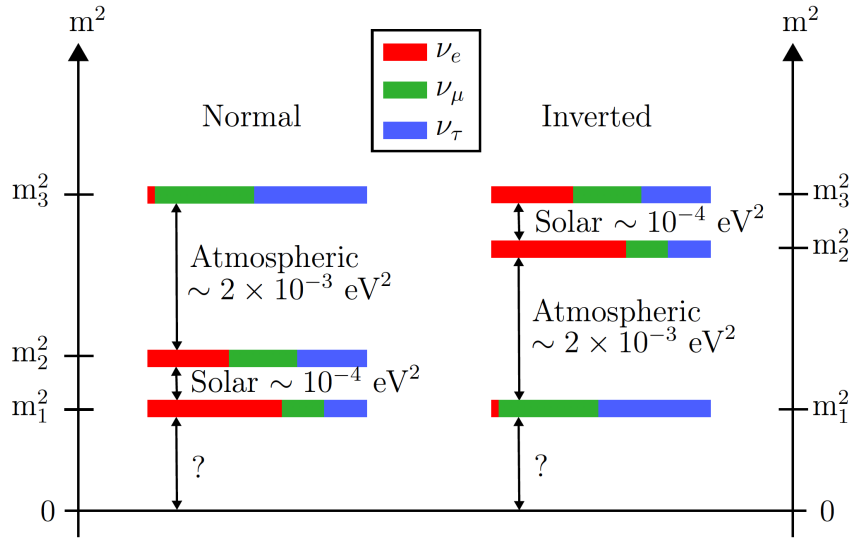


Figure 2.5: A representation showing the "normal" and "inverted" mass ordering of absolute neutrino masses [31].

other ideas on determining the electron energy precisely, such as Project-8 which measures the frequency of cyclotron radiation emission from single electrons [30].

2.5.3 Neutrino Mass Ordering

Oscillation experiments have confirmed that $m_1 < m_2$ through precise measurements of the Δm_{12}^2 . But there are still two possibilities whether $m_1 < m_2 < m_3$ known as normal ordering (NO) or $m_3 < m_1 < m_2$ known as the inverted ordering (IO), shown in Figure 2.5. Thus the neutrino mass ordering remains an open question to be solved. The current and next generation of neutrino oscillation experiments will measure the sign of Δm_{32}^2 to determine the neutrino mass ordering.

A $0\nu\beta\beta$ search is dependent on the neutrino mass ordering, because the decay rate depends on the effective Majorana mass $\langle m_{\beta\beta} \rangle$ which can be expressed as a function of the lightest neutrino mass m_{light} , see Figure 2.6. The two distinct bands are for the normal and inverted mass ordering. The width of each band is determined by the uncertainty over the CP-violating phases.

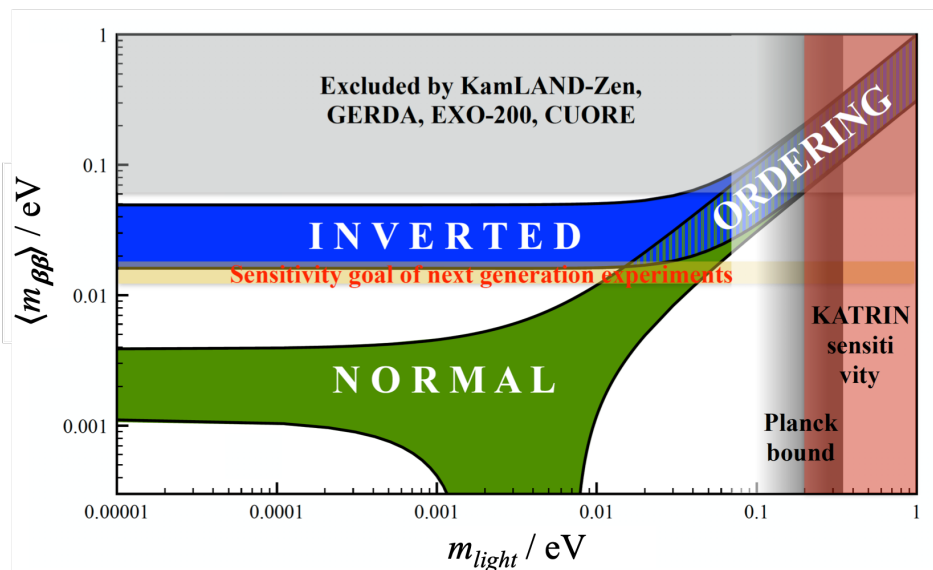


Figure 2.6: The effective Majorana mass $\langle m_{\beta\beta} \rangle$ as a function of the lightest neutrino mass m_{light} , with best fit values with 2σ errors of the oscillation parameters, for normal ordering (green) and inverted ordering (blue) [32].

2.5.4 CP violation

In the SM, CP violation in the quark sector is caused by a complex phase in the CKM matrix describing quark mixing. Similarly, the CP violating phase in the PMNS matrix can cause a difference in the oscillation probability between neutrinos and anti-neutrinos. Future long baseline (LBL) accelerator neutrino oscillation experiments can detect this difference and determine the Dirac CP violating phase. If the neutrinos are Majorana particles, there are two additional CP violating phases in the PMNS matrix which do not affect the neutrino oscillation probability and are therefore unable to be measured with oscillation experiments. A $0\nu\beta\beta$ experiment is the only practical way to measure the Majorana CP violating phase.

2.5.5 Dirac or Majorana

The nature of the neutrino, whether it is a Dirac particle or a Majorana particle, is one of the most fundamental questions in particle physics, and it can only be determined by $0\nu\beta\beta$ experiments. Current and near future experiments will be

able to reach the sensitivity of $\langle m_{\beta\beta} \rangle$ if the neutrino mass ordering is inverted; however, it will be more challenging if the mass ordering is normal, as illustrated in Figure 2.6.

Chapter 3

Double Beta Decay

3.1 Beta Decay

Beta decay (β decay) is mediated by the weak force. It transmutes a nucleus to a different element accompanied by the emission of a neutrino or anti-neutrino. There are three forms of this process: β^- decay, β^+ decay, and electron capture (EC).

In β^- decay, a neutron converts to a proton, emitting one electron and one anti-neutrino:



In β^+ decay, a proton converts to a neutron, emitting one positron and one neutrino:



EC converts a proton and an electron to a neutron, accompanied by the emission of a neutrino. In EC, an atomic electron exchanges a W boson with a quark in the nucleus:



All three types of β decay process are allowed only when the mass of the nucleus

in the initial state is higher than that in the final state:

$$M(A, Z_i) > M(A, Z_f), \quad (3.4)$$

where $M(A, Z)$ is the mass of the atom with A nucleons and Z protons, and the subscripts i and f refer to the initial and final states respectively. The mass of a nucleus, $M(A, Z)$, can be estimated using the semi-empirical mass formula (SEMF) [33], therefore it is possible to predict whether a β decay is allowed or forbidden. The SEMF gives the mass of a nucleus, m , as:

$$m = Zm_p + (A - Z)m_n - a_V A + a_s A^{2/3} + a_c \frac{Z^2}{A^{1/3}} + a_A \frac{(A - 2Z)^2}{A} + \delta(A, Z), \quad (3.5)$$

where

$$\delta(A, Z) = \begin{cases} \frac{a_p}{A^{1/2}} & Z, N \text{ even (} A \text{ even)} \\ 0 & A \text{ odd} \\ \frac{-a_p}{A^{1/2}} & Z, N \text{ odd (} A \text{ even)}. \end{cases} \quad (3.6)$$

The first two terms calculate the masses of individual protons and neutrons respectively. The rest are the volume term, the surface term, the Coulomb term, the asymmetry term, and the pairing term, which provide the correction to the approximation. For fixed A , parabolic curves are generated as a function of Z , which dictate which β decays are energetically allowed. If A is even, two parabolas exist, one for odd-odd and one for even-even nuclei as shown in Figure 3.1.

3.2 Two Neutrino Double Beta Decay

In Figure 3.1, it can be seen that the beta decay process of isotope (c) \rightarrow (d) is energetically forbidden. However, it can undergo the process (c) \rightarrow (e) where two β decays occur simultaneously with two neutrons decaying to two protons, emitting two electrons and two anti-neutrinos. This rare process is called the two

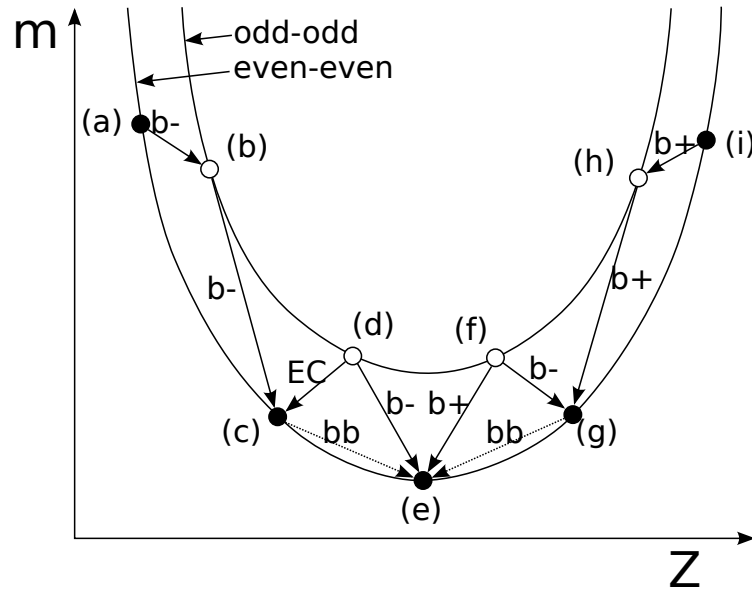
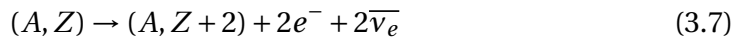


Figure 3.1: Predictions of the SEMF for an even value of A . The arrows between the two parabolae show the energetically allowed β decays [31].

neutrino double beta decay ($2\nu 2\beta$) and it was first postulated by Goeppert-Mayer in 1935 [34].



It is clear that this process only occurs in even-even nuclei where β decay is energetically impossible, or strongly suppressed by conservation principles. The Feynman diagram of the $2\nu 2\beta$ process is shown in Figure 3.2.

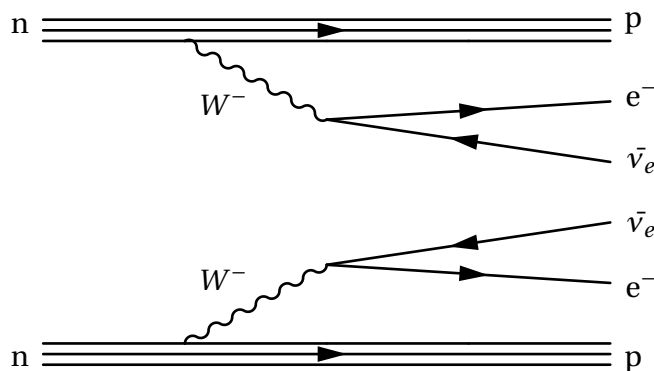


Figure 3.2: Feynman diagram for $2\nu 2\beta$, a second order SM process.

Similar to the spectrum of the β decay, the spectrum of the total energy of the

emitted electrons in the $2\nu 2\beta$ decay is also continuous and the end-point is at the nuclear transition energy $Q_{\beta\beta}$.

$Q_{\beta\beta}$ is the total energy released in the process and it can be calculated using:

$$Q_{\beta\beta} = M(A, Z) - M(A, Z + 2). \quad (3.8)$$

The half-life of the decay is parameterised as

$$(T_{1/2}^{2\nu}(A, Z))^{-1} = G^{2\nu}(Q_{\beta\beta}, Z) |M^{2\nu}(A, Z)|^2, \quad (3.9)$$

where $G^{2\nu}$ is a four-body phase space factor that can be calculated exactly, and $M^{2\nu}$ is the $2\nu 2\beta$ nuclear matrix element (NME) for the decay, which is effectively a nuclear structure calculation of the transition probability from the initial to final states. It should be noted that the NME calculation is heavily model-dependent, as mentioned in Section 3.4, and as such experimental information is vital to tune models appropriately. Although the study of this process does not allow one to discriminate between the Dirac or Majorana nature of the neutrino, it remains nonetheless crucial because it constitutes the ultimate background to searching for the neutrinoless double beta decay.

3.3 Neutrinoless Double Beta Decay

Neutrinoless double beta decay ($0\nu 2\beta$) is a hypothesised decay which was first proposed by W.H. Furry in 1939 [35]. In the $0\nu 2\beta$, two β decays occur simultaneously, resulting in the emission of two electrons without anti-neutrinos. It is clear that this process violates lepton number and is thus forbidden in the SM.

$$(A, Z) \rightarrow (A, Z + 2) + 2e^- \quad (3.10)$$

All isotopes that can result in $2\nu 2\beta$ are also candidates for $0\nu 2\beta$. The half-life of this process is:

$$(T_{1/2}^{0\nu}(A, Z))^{-1} = m_{\beta\beta}^2 \cdot |M^{0\nu}(A, Z)|^2 \cdot G^{0\nu}(Q_{\beta\beta}, Z), \quad (3.11)$$

where $G^{0\nu}$ is now a two-body phase space factor which can be calculated exactly, $M^{0\nu}$ is the $0\nu 2\beta$ NME, and $m_{\beta\beta}$ is the effective Majorana mass of the neutrino defined as:

$$m_{\beta\beta} = \left| \sum_i U_{ei}^2 m_i \right|, \quad (3.12)$$

where U_{ei} is the elements of the neutrino mixing matrix and m_i are the neutrino mass eigenstates. The effective Majorana mass depends on the mechanism of $0\nu 2\beta$. It is still not yet clear whether light Majorana mass term is the leading mechanism of $0\nu 2\beta$. There are many alternative mechanisms of the $0\nu 2\beta$, such as the neutrino mass mechanism [36], right-handed currents [37], Majorana emission [38], R-parity violating SUSY [39], etc. The most common mechanism among them is the neutrino mass mechanism [31], or light neutrino exchange mechanism, which requires the least modification to the SM.

In the neutrino mass mechanism, a light RH (R) Majorana neutrino undergoes a helicity flip, being absorbed as a light LH Majorana neutrino (see Figure 3.3). There is an inherent dependence of the decay rate on the effective mass due to the requirement of a helicity flip.

As there are only two electrons emitted in the $0\nu 2\beta$ process, the experimental signature is given by two electrons whose energy sums to a monochromatic line, see Figure 3.4).

In the SM, the weak interaction is only propagated by a LH W boson, W_L . A Left-Right Symmetric model has been proposed to resolve this apparent asymmetry,

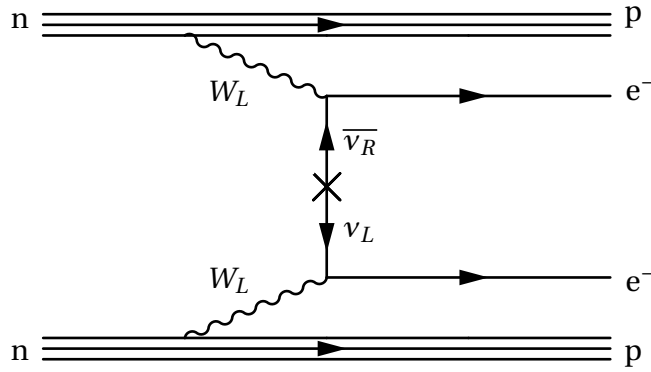


Figure 3.3: Feynman diagram of $0\nu 2\beta$ for the neutrino mass mechanism. The decay is facilitated by the exchange of a Majorana neutrino.

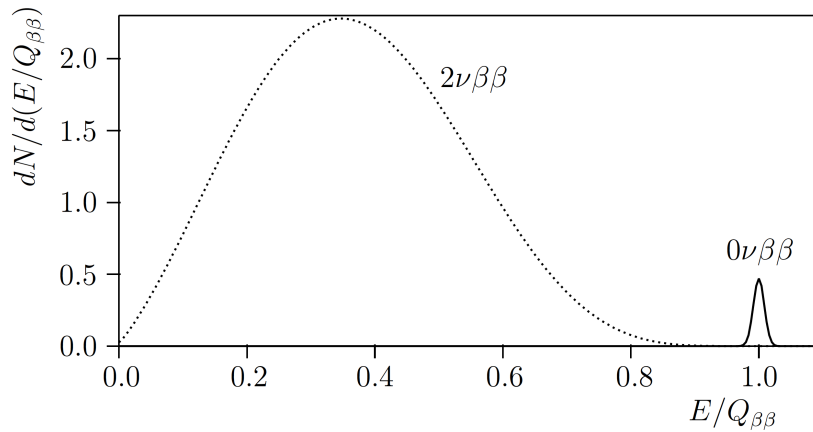


Figure 3.4: Distribution of the sum of electron energies for $2\nu 2\beta$ and $0\nu 2\beta$. The curves assume that $T_{1/2}^{0\nu}$ is 1% of $T_{1/2}^{2\nu}$, with an energy resolution of 2% [40].

where a new RH gauge boson is introduced. The new boson may be completely new, such as a W' boson, or be an addition to the SM W boson such that W is an admixture of W_L and W_R . These new models can lead to $0\nu 2\beta$ without a helicity flip, as can be seen from Figure 3.5 [37].

RH currents will produce a different distribution of individual electron energies and the opening angle between them which can only be distinguished in an experiment which exploits a SuperNEMO-like technology [41], see Figure 3.6.

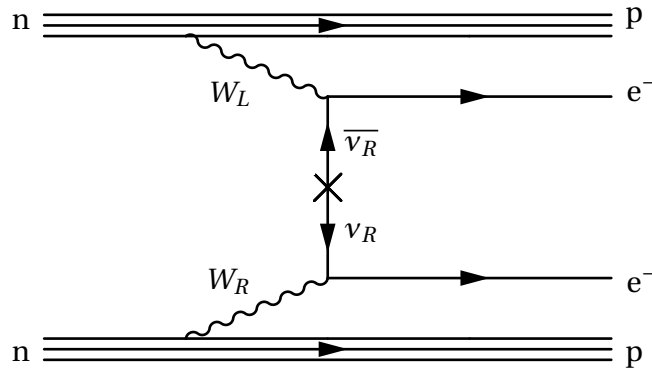


Figure 3.5: Feynman diagram from $0\nu 2\beta$ using a right handed weak current, described by the $\langle \lambda \rangle$ decay mode.

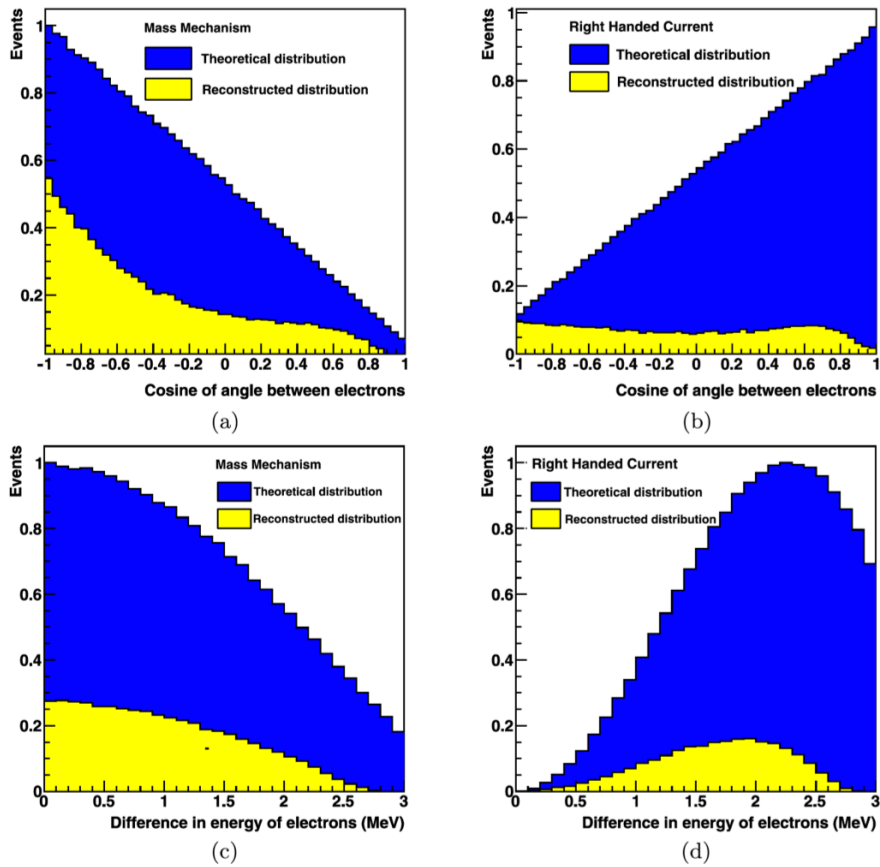


Figure 3.6: Theoretical and experimental electron angular distributions for (a) mass mechanism and (b) right-handed current. Theoretical and experimental electron energy difference distributions for (c) mass mechanism and (d) right-handed currents. All distributions are shown for the isotope ^{82}Se and the reconstructed distributions (yellow) and plotted together with theoretical distributions (blue) to show the signal efficiency [41].

3.4 Nuclear Matrix Elements

Searching for the $0\nu 2\beta$ process can produce a result of the half-life of the decay, $T_{1/2}^{0\nu}$, which can be converted to the physics parameter of interest, usually the effective neutrino mass $\langle m_{\beta\beta} \rangle$ that can not be directly measured. The appropriate NME is required for this conversion (Equation 3.11). To calculate the NME, the many-body Schrödinger equation needs to be solved, accounting for each nucleon-nucleon interaction, given the total initial and final state nuclear wave functions. Due to the complexity of the calculations, various approximations and simplifications have been developed and are applied [36].

To date, five main approaches based on different approximations have been applied with regards to this issue, all of which involve two stages. The first stage is to create a many-body Hamiltonian that describes the nucleon-nucleon interactions at short distances. The second stage is to introduce a mean field which incorporates information about the nuclear structure and residual interactions.

3.4.1 Interacting Shell Model

The interacting shell model (ISM) [42], considers only a limited number of nuclear orbitals close to the Fermi level, but all possible correlations for these orbitals are included. Compared to other correction methods, this approach tends to reduce the value of the NMEs due to the limited number of orbits considered. The ISM is useful for calculating single particle states that are close to Fermi level, and is usually reliable for small nuclei such as ^{48}Ca , ^{76}Ge , and ^{82}Se . In particular, a doubly magic nucleus, such as ^{48}Ca , is considered to be a test bench for ISM calculations. However, it has difficulties in calculating deformed nuclei, such as ^{150}Nd and heavy isotopes [43].

3.4.2 Quasiparticle Random Phase Approximation

The quasiparticle random phase approximation (QRPA) [44] considers more nuclear orbitals but simpler interactions between nucleons compared to the ISM. In the QRPA, the nuclei is described using nucleon-nucleon pairs, and these quasiparticles are then treated as bosons. The coupling constant g_{pp} , which quantifies the proton-proton interaction, is a free parameter of the model but can be constrained by $2\nu 2\beta$ results. Experimental inputs help reduce uncertainties on the model, but might not describe the $0\nu 2\beta$ accurately. The QRPA is more reliable for calculation of the large nuclei in comparison to ISM.

3.4.3 Interacting Boson Model

The interacting boson model (IBM) [45] is similar to the ISM but considers only bosons made of pairs of nucleons with the angular momentum states being restricted to $L = 0$ or $L = 2$. IBM shares similar advantages and disadvantages as the ISM.

3.4.4 Projected Hartree-Fock-Bogoluibov Method

In the projected Hartree-Fock-Bogoluibov (PHFB) [46] model, nuclear wave functions with good particle number and angular momentum are constructed by projection on the HFB wavefunctions. The nuclear Hamiltonian includes only quadrupole interactions. It describes neutron pairs with even angular momenta and positive parity only (non- 0^+ pairs are heavily suppressed in comparison to others).

3.4.5 Energy Density Functional Method

The energy density functional (EDF) method [47] is an improvement based on the PHFB method. It includes modified inter-nucleon interaction to reproduce the Gogny interaction.

3.4.6 Comparison of different NME calculations

All five of these models have been used to calculate several isotopes for similar processes, including $2\nu 2\beta$ decay and β decay. However, the computation result for the $0\nu 2\beta$ decay differs to each other, typically by a factor of 2 - 3, which is problematic as the variation goes directly into an uncertainty in the obtained $0\nu 2\beta$ decay limits from the experiments.

Comparing the NME results evaluated by each method can help to understand the effect of each of these assumptions and the associated systematic error with the resulting NMEs. In the conversion from an experimental half-life to $\langle m_{\beta\beta} \rangle$, the phase space factor, $G^{0\nu}$, enters into the calculation alongside the NME. This factor exhibits a proportionality given by

$$G^{0\nu} \sim \frac{g_A^4}{R_A^2}, \quad (3.13)$$

where g_A is the ratio of the vector and axial-vector couplings and R_A is the atomic radius, commonly parameterised as $r_0 A^{1/3}$ [48]. In the past, different NME calculations are performed using different values of g_A and r_0 so that the phase space factors, and therefore NME results, are not directly comparable. Common values for g_A are either 1.0 or 1.25 and for r_0 either 1.1 to 1.2 fm.

Figure 3.7 shows the difference between the NME of the 11 $0\nu 2\beta$ candidate isotopes in the mass mechanism, calculated using the five methods described previously. Also, for a meaningful comparison, g_A and r_0 are adjusted to be same values, 1.25 and 1.2 respectively.

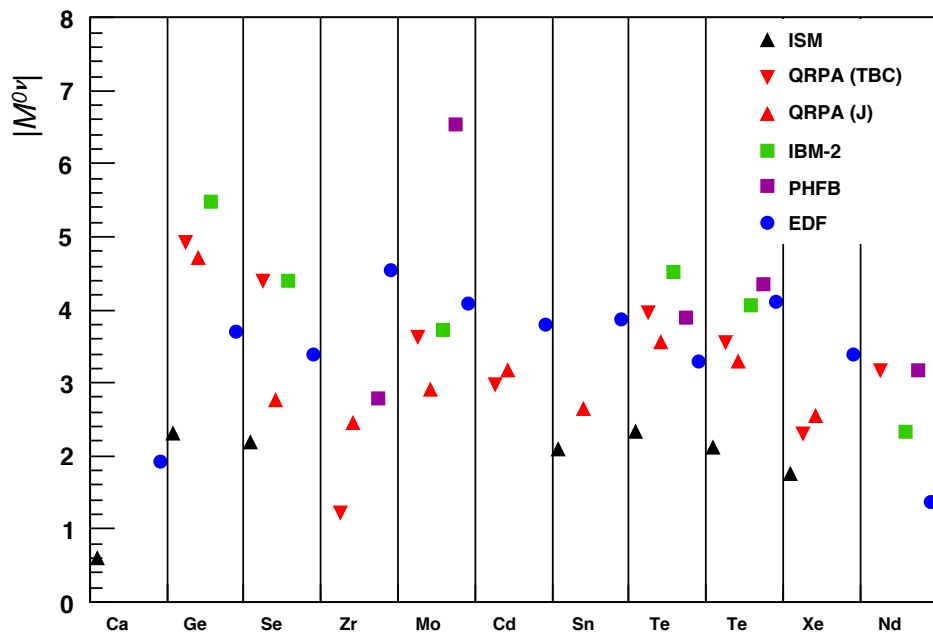


Figure 3.7: $0\nu 2\beta$ NME for the neutrino mass mechanism, calculated with five different approaches. QRPA(TBC) and QRPA(J) show the results of the Tübingen-Bratislava-Caltech and Jyväskylä groups. $|M^{0\nu}|$ values taken from [36]. Conversions for $g_A = 1.25$ and $r_0 = 1.2$ fm have been made where necessary.

Chapter 4

Current Status of Double Decay Experiments

4.1 Detector Design Considerations

Double beta decay experiments search for a small signal from $0\nu2\beta$ hidden amongst backgrounds from natural radioactivity and $2\nu2\beta$. Although the $0\nu2\beta$ process has not yet been observed, many $0\nu2\beta$ decay search experiments using different techniques exist, and these experiments have set ever more stringent limits of $0\nu2\beta$ and improved the half-life measurement of $2\nu2\beta$.

The expected half-life sensitivity of a $0\nu2\beta$ decay experiment can be approximately parameterised using the following equation [40]:

$$T_{1/2}^{0\nu} > \frac{4.16 \times 10^{26} \text{ yr}}{n_\sigma} \left(\frac{\epsilon a M t}{A} \right), \sqrt{\frac{1}{N_B}} \quad (4.1)$$

where

- $T_{1/2}^{0\nu}$ is the half-life sensitivity to $0\nu2\beta$ in years
- n_σ is the number of standard deviations for a given confidence level (90% C.L. corresponds to $n_\sigma = 1.64$ for Gaussian distribution.)

- ϵ is the event detection and identification efficiency
- a is the isotopic abundance of the $0\nu 2\beta$ source isotope in the source mass
- A is the mass number of the source isotope
- Mt is the total exposure of the experiment in kg·yr
- N_B is the number of expected background events for the exposure

This equation is valid for a relatively large number of expected background events, where a Gaussian approximation of Poissonian statistics is valid, so the error is $\sqrt{N_B}$. In cases where the number of expected background events is not sufficiently high, it may still provide indications as to how experimental parameters may affect the half-life sensitivity. The equation shows that in order to maximise the half-life sensitivity in an experiment, it requires:

- a high detection efficiency
- the highest possible mass M of the source
- the lowest possible background

Besides, to achieve better sensitivity, it also requires the detector to have:

- good energy resolution of the detector, which helps reduce the impact of both the natural radioactivity and the $2\nu 2\beta$ process high-energy tail in the Region of Interest (ROI).
- good spatial resolution to reduce the background from random coincidences.

For a zero-background experiment, the sensitivity follows

$$T_{1/2}^{0\nu} = \frac{\ln 2 N_A}{n_\sigma} \left(\frac{\epsilon a}{A} \right) Mt, \quad (4.2)$$

where n_σ at 90% CL is 2.3 for the zero background case, and N_A is Avogadro's constant. One major advantage of the zero-background experiment is that the sensitivity is proportional to the exposure Mt .

4.1.1 Isotopes

12 isotopes have been observed to undergo $2\nu 2\beta$ decay, all of which are $0\nu 2\beta$ decay candidates. The experimental considerations of choosing the isotope includes:

- high isotope $Q_{\beta\beta}$ value to reduce possible background from natural radioactivity
- possibility of increasing the mass of isotope, which is limited by the natural abundancy and ease of enrichment.
- high phase-space, as discussed in Section 3.4
- high NME, as discussed in Section 3.4

The list of most promising $2\nu 2\beta$ decay isotopes are summarised in Table 4.1. While the majority of isotopes can be enriched via centrifugation, which is relatively low in cost for producing a large mass of the isotope, electromagnetic separation is currently the only possible method for producing ^{48}Ca , ^{96}Zr , and ^{150}Nd .

4.1.2 Radio-purity

As shown in Equation 4.1, in order to maximise the sensitivity of the experiment, the largest possible exposure is required, meaning as many atoms as possible of double beta decay isotope should be studied for the longest possible time. In addition, the best possible detector efficiency to detect the event it also required, in the case that a $0\nu 2\beta$ process does occur. One dominant background contribution is from the natural radioactive isotopes ^{214}Bi and ^{208}Tl , which come from

Isotope	$Q_{\beta\beta}$	$G^{0\nu}$	NA	Enrichment Possibilities	
	keV	10^{-14} yr^{-1}	%	Current Method	R&D Method(s)
^{48}Ca	4276	7.15	0.187	EMS	Laser Separation, Gaseous Diffusion
^{76}Ge	2039	0.71	7.8	Centrifugation	-
^{82}Se	2992	3.11	9.2	Centrifugation	-
^{96}Zr	3348	5.63	2.8	EMS	Laser Separation
^{100}Mo	3034	5.03	9.6	Centrifugation	-
^{116}Cd	2804	5.44	7.6	Centrifugation	-
^{130}Te	2529	4.89	34.5	Centrifugation	-
^{136}Xe	2467	5.13	8.9	Centrifugation	-
^{150}Nd	3368	23.2	5.6	EMS	Laser Separation, Centrifugation

Table 4.1: Details of isotopes commonly used in $0\nu 2\beta$ experiments, showing Q-value, phase-space factor, natural abundance (NA), and possibilities for enrichment. EMS is the electromagnetic separation. $G^{0\nu}$ is calculated with $g_A = 1.25$ and $R = 1.2 A^{1/3} \text{ fm}$ [36, 49].

^{238}U and ^{232}Th contamination in the detector materials, hence where N_B usually increases linearly with exposure in real-life operation, with such a dependency on exposure reduces to \sqrt{Mt} .

The half-life sensitivity of an experiment scales as $1/\sqrt{N_B}$, as shown in 4.1. As such, the best sensitivity will be achieved by minimising the number of background events while keeping a high signal efficiency.

To suppress the backgrounds from radioactive contamination, the detector materials must be carefully chosen to be extremely radiopure. For example, to reach a sensitivity to the Majorana neutrino mass of 10 meV level, it is expected that materials will require radiopurity below the $\mu\text{Bq/kg}$ level. To further reduce this contribution, it is also preferable to select an isotope with $Q_{\beta\beta} > 2.6 \text{ MeV}$ (as listed in Table 4.1). This greatly reduces the background from ^{208}Tl , which has the

highest energy γ -line (at 2.6 MeV) in the ^{232}Th decay chains.

4.1.3 Location

Except for contamination of the detector materials, there are external sources of background for rare event search experiments, one of which are cosmic muons. A typical $0\nu 2\beta$ experiment has at least 2500 metres water-equivalent of rock to ensure the suppression of cosmic background, and as such it is essential to locate the experiment in an underground laboratory. Figure 4.1 shows a list of the major underground laboratories around the world.

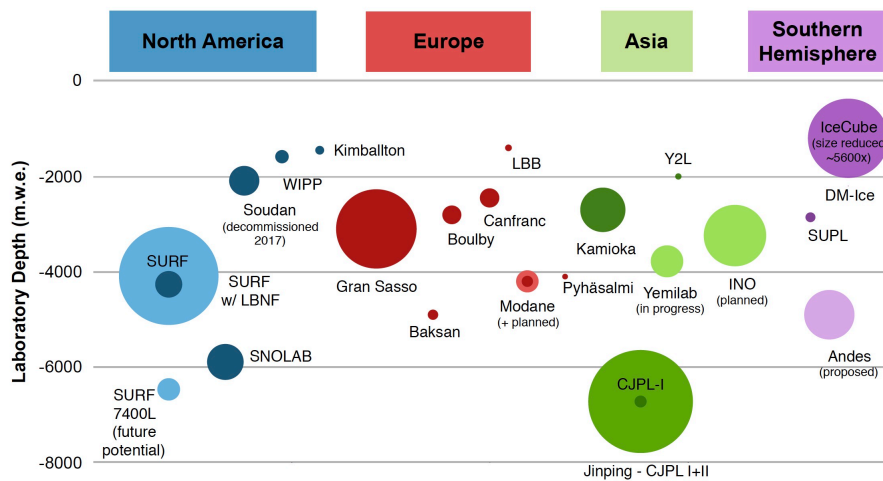


Figure 4.1: A list of the world major underground laboratories, their respective depth in meters water equivalent (m.w.e.), and their volume (represented by the size of the circles) [50].

4.1.4 Shielding

Additional shielding can provide a further reduction of the background from external sources. As background from the surrounding environment, i.e. rocks and materials in the lab, usually consist of gamma radiation or neutrons, radio-pure lead, ultra-pure copper, and water shielding are generally chosen to protect the detector. In addition, there is usually a detector shell made of radio-pure materials to act as a radon barrier.

One external background that can not be shielded against is the ^8B solar neutrino, which increases proportionally to the detector mass. For the current experiments, like SNO+, this is already expected to be a major background [51].

4.1.5 Energy Resolution

In principle, the signal window of the $0\nu 2\beta$ decay should be very narrow, but experimentally it is limited by the energy resolution of the detector. Maximising detector energy resolution can help to narrow down the range of signal on the total electron energy spectrum, and therefore, reduce the background. As discussed in Section 3.2, the tail of $2\nu 2\beta$ decay is an irreducible background to the search for $0\nu 2\beta$ decay. A good energy resolution is the most practical way to suppress $2\nu 2\beta$ background.

4.2 Detector Technologies of Various $0\nu 2\beta$ Experiments

4.2.1 Semiconductor Experiments

In the semiconductor experiments, the $0\nu 2\beta$ decay source material is usually some form of the semiconductor, such as ^{76}Ge . When a double beta decay event occurs, the emitted electrons ionise the semiconductor, leading to a cascade of electron/hole pairs that drift to electrodes on the surface of the detector, generating a voltage pulse that can be measured. As ^{76}Ge can be readily enriched to above 80% to produce large crystals which have a depletion layer of a few centimetres, allowing total absorption of gamma rays up to ~ 5 MeV, it is the most popular isotope. Germanium detectors of this size are often referred to as high-purity germanium (HPGe) detectors. Enriched HPGe detectors are the source and detector at the same time. To minimise the background, such as beta decay of ^{208}Tl , the HPGe detectors are required to be extraordinarily radio-pure.

HPGe detectors operate at cryogenic temperatures to reduce thermal noise. Also, in this configuration, they can achieve excellent energy resolution of $\sim 0.15\%$ at ^{76}Ge $Q_{\beta\beta}$, which is the primary advantage of this type of experiment. However, these experiments suffer from lots of background events from the radioactive process occurring in the detector material since they can only measure the energy spectrum of the electrons.

The modern development of Broad Energy Germanium (BEGe) detectors further improve performances such as energy resolution and background reduction, and they are now used in modern $0\nu 2\beta$ decay experiments. BEGe detectors also have signal electrodes of small size, resulting in a low capacitance, which can improve the determination of energy. The increased field near the electrode can improve the identification of the event topology to reduce backgrounds.

The modern generation of semiconductor experiments, GERDA and MAJORANA, are built on the successes of the previous Heidelberg-Moscow (H-M) [52] and IGEX experiments [53]. Moreover, the GERDA and MAJORANA collaborations recently joined together to develop the next generation experiment, LEGEND, which is aiming to achieve a sensitivity of $\langle m_{\beta\beta} \rangle \sim 15$ meV [54, 55].

- **GERDA** located at the Laboratori Nazionali del Gran Sasso (LNGS).

It consists of a large mass of germanium crystals isotopically enriched to $\sim 86\%$ in ^{76}Ge that acts simultaneously as both source and detectors. The detectors are mounted in low-mass copper holders with ultra-low radioactivity and immersed directly in a 64 m^3 cryostat filled with 70 tonnes of liquid argon (LAr), which works both as a coolant and as active shielding from external backgrounds [56]. The cryostat is located inside a 590 m^3 ultra-pure water tank instrumented with 66 PMTs for the detection of Cherenkov light from cosmic muons. GERDA-II set a competitive half-life limit of $T_{1/2}^{0\nu} > 8.0 \times 10^{25}$ yr [57].

- **MAJORANA** experiment uses similar technology to the previous semicon-

ductor experiments, with the main difference being the shielding. MAJORANA deploys its HPGe detectors in a custom vacuum cryostat and uses a compact shield made with lead, oxygen-free copper, electro-formed copper, and scintillator paddles. To achieve the challenge goal of extremely low backgrounds level at 0.001 cts/(keV·kg·yr), many of the detector components were made in underground facilities to ensure they met strict radiopurity requirements. In addition, more effective shielding and pulse shape discrimination are used to reduce backgrounds.

The Majorana Demonstrator [58] used 29.7 kg of 88%-enriched ^{76}Ge and 14.4 kg of natural p-type point-contact detectors at the Sanford Underground Research Facility (SURF). The experiment has placed a half-life limit at $T_{1/2}^{0\nu} > 8.0 \times 10^{25}$ yr, translating to $m_{\beta\beta} < 200 - 433$ meV [59].

- **COBRA** holds five different isotopes: ^{114}Cd , ^{128}Te , ^{70}Zn , ^{130}Te , and ^{116}Cd in an array of CdZnTe (CZT), which is an intrinsic semiconductor at room temperature.

The COBRA Demonstrator consists of a $4 \times 4 \times 4$ array of 1 cm^3 (5.9 g) detectors. With the 234.7 kg · d exposure, it has set limits at $T_{1/2}^{0\nu} > 1.6 \times 10^{21}$ yr, $T_{1/2}^{0\nu} > 1.9 \times 10^{21}$ yr, $T_{1/2}^{0\nu} > 6.8 \times 10^{18}$ yr, $T_{1/2}^{0\nu} > 6.1 \times 10^{21}$ yr, $T_{1/2}^{0\nu} > 1.1 \times 10^{21}$ yr respectively [60].

While the energy resolution of COBRA experiments are not competitive with the HPGe experiments, it has the main advantage of operating at relatively high temperature (~ 20 °C). The experiment will use a pixelated array and improved readout, enabling the possibility of particle tracking and identification, which can significantly reduce the background level. If the background reduction can be significantly improved, the technology will be used on a 415 kg detector, aiming at a sensitivity of 50 – 70 meV [61].

4.2.2 Scintillator Experiments

In scintillator experiments, the $0\nu 2\beta$ candidate isotope is placed inside the radiopure scintillating medium and surrounded with PMTs. This design allows for the observation of light emitted by the scintillator when the decay product of the $0\nu 2\beta$ isotope excites the scintillation material. Generally, scintillator experiments are relatively inexpensive, and they can reach a high degree of radiopurity.

Scintillator experiments can be divided into two major types based on their technology. The first type is where the $0\nu 2\beta$ isotope is dissolved in a large volume of liquid scintillator. This design allows for the study of large masses of isotopes such as ^{136}Xe , ^{130}Te , or ^{150}Nd . In addition, the scintillator detectors can provide relatively good detection efficiency, good self-shielding, and low background. However, these experiments suffer from poor energy resolution. The two main experiments using this technology are the KamLAND-Zen experiment studying ^{136}Xe , and the SNO+ experiment studying ^{130}Te .

- **KamLAND-Zen** use the existing KamLAND detector which was originally built to study neutrino oscillations [62]. In the centre of the KamLAND-Zen detector, there is a transparent nylon inner balloon which is 3.08 m in diameter containing 13 tonnes of Xenon-loaded liquid scintillator. It is surrounded by 1000 tonnes of liquid scintillator contained in a 13 m diameter spherical outer balloon, which provides an active shield. Outside the outer balloon, there is a layer of 1.8 m thickness transparent buffer oil. The scintillation lights are viewed by 1,879 17-inch and 20-inch PMTs mounted on the inner surface of the 18-meter-diameter stainless steel spherical tank, which is surrounded by a 3200-ton water-Cherenkov detector serving as a radiation shield from the surrounding rock.

The first phase of the KamLAND-Zen experiment (Phase I) contained ~ 300 kg of ^{136}Xe and achieved an exposure of 89.5 kg·yr, reaching a half-life limit of $T_{1/2}^{0\nu} > 1.9 \times 10^{25}$ yr (90% C.L.), corresponding to $\langle m_{\beta\beta} \rangle < 160 - 330$ meV

[63].

After the first phase, the liquid scintillator was purified to remove impurities. In the second phase (Phase II), ~ 340 kg of ^{136}Xe was used and a reduction of ^{110m}Ag by more than a factor of 10 was found. Phase II reached an exposure of 504 kg·yr, which is equivalent to $T_{1/2}^{0\nu} > 1.9 \times 10^{25}$ yr, corresponding to $\langle m_{\beta\beta} \rangle < 61 - 165$ meV [28].

Furthermore, due to its low background level, KamLAND-Zen can observe $2\nu 2\beta$ across a wide energy range and provide strong constraints on Majoron emission decay modes [64].

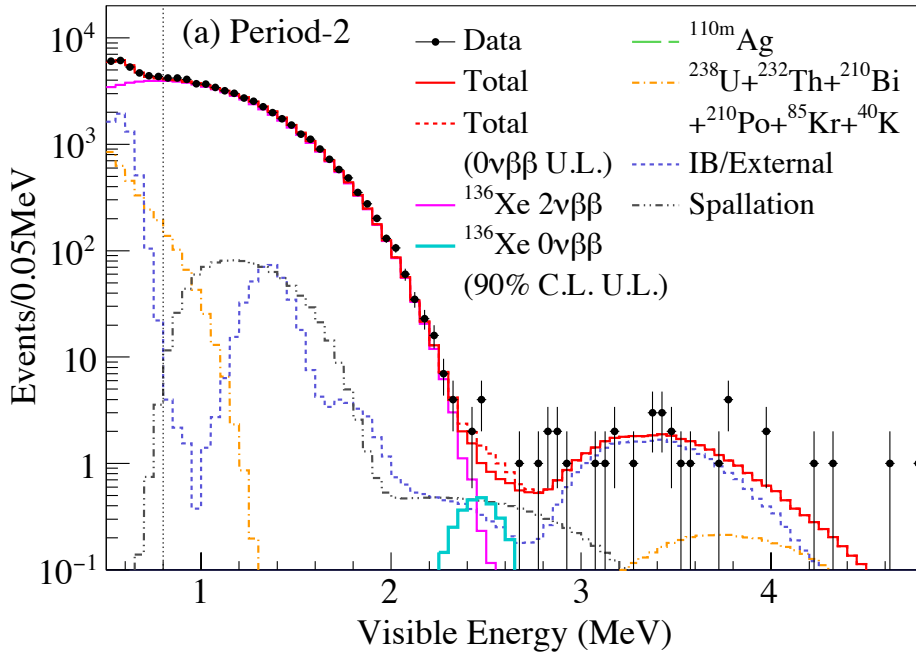


Figure 4.2: Energy spectrum showing the results from KamLAND-Zen [28].

Additionally, in a future upgrade, the KamLAND2-Zen experiment will improve the detector energy resolution as well as increase the capacity to load more isotope. Using 1 ton of ^{136}Xe , it is expected to reach $\langle m_{\beta\beta} \rangle \sim 20$ meV, fully covering the IH region [65].

- **SNO+** follows a similar principle to KamLAND-Zen but studies a different isotope: ^{130}Te . The SNO+ detector is inherited from SNO located in the

Sudbury Neutrino Observatory, which is one of the world's deepest underground laboratory (~ 6000 m.w.e.).

The detector consists of a 12 m diameter spherical acrylic vessel (AV) which is shielded by a water bath and surrounded by 9,394 8-inch PMTs mounted on a stainless steel support structure [66].

^{130}Te will be dissolved in liquid scintillator contained in a 12 m diameter acrylic sphere. This acrylic sphere is shielded by a water bath and instrumented with 9500 PMTs.

For the initial phase, ^{130}Te will be loaded at 0.3% within a scintillation solution, providing 800 kg of isotope reaching a sensitivity of $\langle m_{\beta\beta} \rangle < 50 - 100$ meV. In the second phase, it will increase the concentration to 3%, loading 8000 kg of ^{130}Te in total, with the expected sensitivity reaching the level of $\langle m_{\beta\beta} \rangle < 20 - 40$ meV [67].

The second type of scintillator experiments is where the isotope is inherently part of the scintillator. The two most successful experiments of this type are ELEGANT VI and CANDLES III. Both of them use crystal scintillators containing ^{48}Ca .

- **ELEGANT VI** studied 23 $\text{CaF}_2(\text{Eu})$ crystal scintillators, which contained 7.6 g of ^{48}Ca in total. These crystals were shielded by an active veto to reduce the background. With a total exposure of 0.015 kg-yr, the ELEGANT VI experiment produced a half-life limit of $T_{1/2}^{0\nu} > 5.8 \times 10^{22}$ yr, equivalent to the $\langle m_{\beta\beta} \rangle < 3.5 - 22$ meV [68].
- **CANDLES III** evolved from ELEGANT VI. It studies 305 CaF_2 crystals, which contain 300 g of ^{48}Ca in total. The crystals are surrounded by liquid scintillator which acts as the active shielding and removes the need for doping of the crystals. The experiment is currently taking data and is expected to achieve a sensitivity of $\langle m_{\beta\beta} \rangle < 50 - 100$ meV or 0.5 eV. If ^{48}Ca enrichment technology can be improved in the future, the experiment can be scaled up

by an order of magnitude to study ~ 3 kg of ^{48}Ca , reaching a sensitivity of 50 meV [69].

4.2.3 Bolometer Experiments

Bolometer experiments measure the $0\nu 2\beta$ through the temperature rises caused by energy absorption. When the $0\nu 2\beta$ decay occurs, the emitted electrons generate heat while passing through the material, thus raising the temperature of the material by a small amount. The temperature increase is the ratio of the energy deposited over the heat capacity, and when the detector operates at a very low temperature (order of mK), the heat capacity of the material at very low temperatures T is proportional to T^3 . In the bolometer experiments, the typical temperature variation is of the order of 0.1 mK per MeV of deposited energy. This temperature variation can be measured by semiconductor thermistors to determine the summed electron energy. Bolometer experiments generally have excellent energy resolution (0.3 - 0.5%), and high efficiency on the containment of the $0\nu 2\beta$ isotopes, and can use different materials as a number of $0\nu 2\beta$ candidates can be used to grow a crystal [70]. However, this type of experiment may suffer from background because the particle identification can be challenging, and the detector response time can be long (order of seconds). Also, for the future experiments, the technical difficulty of maintaining the extremely low temperature can pose a big challenge on building larger detectors.

- **CUORE** is built on the success of the CUORICINO experiment [71] using the same technology. CUORE is composed of a tower array of 988 $5 \times 5 \times 5$ cm³ enriched and natural TeO₂ crystals working at ~ 7 mK, containing total mass of ^{130}Te to 204 kg [72]. After a short time running, the first results show CUORE has already reached a sensitivity of 1.5×10^{25} yr (90% C.L.) [72] corresponding to $\langle m_{\beta\beta} \rangle < 110 - 520$ meV.

To reduce the background, the bolometric crystal can also be used as a scintillator. By combining the temperature and scintillation light measurements,

particle identification can be improved, thus allowing for better background rejection.

- **CUPID** project will be built on the experience and skills gained from the CUORE, with upgraded Particle ID, increased mass of source and reduced background. It is aiming to achieve zero-background in the region of interest to further improve the sensitivity of $0\nu 2\beta$ half-life. The two CUPID demonstrators: CUPID-0 using Zn^{82}Se and CUPID-Mo using $\text{Li}_2^{100}\text{MoO}_4$ have started data taking since 2017 and 2019, respectively [73, 74].

4.2.4 Time Projection Chamber Experiments

The Time Projection Chamber (TPC), which can provide a 3-dimensional reconstruction of a particle trajectory, is a popular detector technique in experimental high energy physics. There are several different designs of TPCs, but their principle remains the same. A TPC contains a sensitive gaseous or liquid medium which is embedded in an electric field. When a particle passes through, it ionises the medium and produces free electrons which drift towards a position-sensitive electron collection device. The induced current is proportional to the ionisation.

In most TPC experiments, the detector medium is also particularly selected as a scintillator, which can measure energy and provide a prompt signal for time measurement. The location of the energy deposited gives the 2-dimensional position. In addition, given the known drift speed of the free electron in a specific medium, and the measured time of arrival, it is possible to reconstruct the event in 3 dimensions. Considering the cost of enrichment, xenon is currently the most suitable medium among all double β candidate isotopes. The most promising scintillating-TPC experiments are EXO and NEXT, both of which search for $0\nu 2\beta$ in ^{136}Xe , utilising the scintillating properties of xenon.

- **EXO-200** is located in an underground cleanroom in the WIPP. The experiment consists of a liquid Time Projection Chamber (TPC) based on Xe.

EXO-200 has completed its science run, studied 200 kg of ^{136}Xe (enriched to 80.6%). The TPC uses cylindrical geometry in order to minimise the surface and thus reduce the background contribution from the copper vessel, and it is symmetric around a central cathode plane held at a negative high voltage. At each end of the TPC, there are planes of anode wires with an array of avalanche photodiodes for ionisation and scintillation readout [75]. EXO-200 phase I started in 2011 and was interrupted in 2014, with a total exposure of 100 kg·yr. Phase II started running in 2016 with an upgraded radon suppression system and low-noise electronics, and it completed data taking in 2018. No $0\nu 2\beta$ signal has been observed, thus a half-life limit has been set at $T_{1/2}^{0\nu} > 1.8 \times 10^{25}$ yr [76]. The EXO-200 experiment has achieved an energy resolution of 2.90% (FWHM) at $Q_{\beta\beta}$ (2.458 MeV for ^{136}Xe) and a background level of $1.9 \pm 0.2 \times 10^{-3}$ counts/keV/kg/yr. The next generation, nEXO, will contain 5 tons of xenon enriched to 90% in ^{136}Xe , aiming for sensitivity on the order of 10^{28} yr. The expected energy resolution reached will be 2.90% (FWHM) with lower noise silicon photomultipliers (SiPMs) for scintillation collection [77].

- **NEXT** is a planned high-pressure gas-phase xenon TPC which is located at the Laboratorio Subterráneo de Canfranc (LSC) in Spain. Operating at high pressure (10 - 15 bar), the TPC can track individual particles, thus providing an effective way of rejecting background through the topological signature of events. The TPC has an asymmetric geometry, with the array of PMTs which detect both the primary scintillation light and the secondary scintillation light to reconstruct energy located at one end referred to as the energy plane, and the SiPMs used for track reconstruction located at the other end near the amplification region. The demonstrator NEXT-100 detector will contain 100 kg of xenon enriched to 91% in ^{136}Xe , aiming to achieve a background level of 0.4×10^{-3} counts/keV/kg/yr and an energy resolution of $< 1\%$ (FWHM) at $Q_{\beta\beta}$ [78]. The final goal of NEXT-100 is to reach a half life sensitivity of $T_{1/2}^{0\nu} > 2.8 \times 10^{25}$ yr after 3 years of running

[78]. If the experiment is successful, the experiment will scale to contain one tonne of xenon.

4.2.5 Tracker-Calorimeter Experiments

In the tracker-calorimeter experiment, the $0\nu 2\beta$ decay source is located at the centre of the detector surrounded by the tracker, followed by the calorimeter. The scattering of the emitted electrons can be minimised in the tracker, benefiting from the low-density gases. The design of tracker-calorimeter experiment allows for full reconstruction and measurement of single-particle energy. As such, the tracker-calorimeter experiments have excellent background rejection ability, and can shed light on the underlying $0\nu 2\beta$ decay mechanism [41]. Tracker-calorimeter experiments perform excellently in both $2\nu 2\beta$ and $0\nu 2\beta$ measurements because they can achieve some of the lowest background rates among $0\nu 2\beta$ experiments across the entire energy spectrum. It has been shown that the angular and electron energy difference distributions can be used to discriminate between the two prominent models, the mass mechanism (MM) and the right-handed current (RHC), as shown in Figure 3.5. The separated source and detector allow for the study of different $0\nu 2\beta$ isotopes. However this design suffers from relatively poor energy resolution. The most notable tracker-calorimeter experiments are the NEMO-3 and SuperNEMO experiments.

- **NEMO-3** operated from 2003 to 2011 at the Laboratoire Souterrain de Modane (LSM). It studied seven different $0\nu 2\beta$ candidates, set the leading $0\nu 2\beta$ decay half-life limits on four of them, and measured the most accurate $2\nu 2\beta$ half-lives on all of them. The isotopes were housed in thin foils which were surrounded by the tracker containing the gas mixture of helium, argon, and alcohol, and then enclosed by a plastic scintillator calorimeter. 25 G magnetic field was applied to enable charge identification. The calorimeter provided position, energy, and timing measurements of individual particles such as electrons, positrons, γ , and α particles. The strongest limit

of NEMO-3, $\langle m_{\beta\beta} \rangle < 0.3 - 0.8$ eV, is provided by 6.9 kg of ^{100}Mo with an exposure of 34.5 kg-yr [79].

- **SuperNEMO** is building upon the successful NEMO-3 design, with improvements on radiopurity, calorimeter design, and detection efficiency. It will contain 20 identical modules housing 100 kg of ^{82}Se in total. The target sensitivity for SuperNEMO is $T_{1/2}^{0\nu} > 1.0 \times 10^{26}$ yr, corresponding to $\langle m_{\beta\beta} \rangle < 40 - 100$ meV [80]. The first Demonstrator Module is about to start its physics run at LSM, aiming to reach zero backgrounds in the region of interest of the $0\nu 2\beta$ decay of ^{82}Se . Thanks to the tracker capabilities and segmented calorimeter, SuperNEMO is currently the only experiment which can study the underlying mechanism of $0\nu 2\beta$ decay. More details of the SuperNEMO experiment can be found in Chapter 5.

4.3 Summary of the Current and Next Generation Experiments

A wide range of experimental techniques has been applied to search for the $0\nu 2\beta$ decay process. A summary of key experiments can be found in Table 4.2 and Table 4.2.

Experiment	Isotope	Mass (kg)	Type	Sensitivity $m_{\beta\beta}$ / meV
MAJORANA	^{76}Ge	40	Semiconductor	100 - 300
GERDA	^{76}Ge	40	Semiconductor	100 - 300
CUORE	^{130}Te	204	Bolometer	100 - 400
KamLAND-Zen	^{136}Xe	380	Liquid Scint.	61 - 165
EXO-200	^{136}Xe	80	Scint. TPC	190 - 450
NEXT-100	^{136}Xe	90	Scint. TPC	70 - 150
NEMO-3	^{100}Mo	7	Tracker-Calo	300 - 800

Table 4.2: Summary of current $0\nu 2\beta$ experiments.

Experiment	Isotope	Mass (kg)	Type	Sensitivity $m_{\beta\beta}$ / meV
LEGEND	^{76}Ge	1000	Semiconductor	10 - 20
CUPID	^{100}Mo	280	Bolometer	12 - 20
KamLAND2-Zen	^{136}Xe	800	Liquid Scint.	20 - 60
SNO+	^{130}Te	800	Liquid Scint.	50 - 100
nEXO	^{136}Xe	3700	Scint. TPC	7 - 18
NEXT-HD	^{136}Xe	1000	Scint. TPC	13 - 60
SuperNEMO	^{82}Se	100	Tracker-Calo	40 - 100

Table 4.3: Summary of future $0\nu 2\beta$ experiments and their designed sensitivity.

The experiments which are currently under construction or have started data-taking are sensitive to $\langle m_{\beta\beta} \rangle \sim 60$ meV, approaching the top of the region corresponding to inverted ordering of neutrino masses, and many of the next generation experiments are planning to study larger masses of $0\nu 2\beta$ isotopes to achieve better sensitivity to $\langle m_{\beta\beta} \rangle \sim 10$ meV. There is a rich interplay with neutrino oscillation experiments. For example, if the inverted ordering is discovered by oscillation experiments the currently proposed $0\nu 2\beta$ experiments should be able to observe or refute $0\nu 2\beta$ driven by the light Majorana neutrino mass.

Chapter 5

The SuperNEMO Experiment

SuperNEMO is a neutrinoless double beta decay experiment using tracker-calorimeter technology 4.2.5, built on the successes of the NEMO-3 experiment. It is designed to search for $0\nu 2\beta$ decay and is capable of reaching a half-life sensitivity of $T_{1/2} > 10^{26}$ years, equivalent to an effective Majorana neutrino mass of $\langle m_\beta \rangle < 40 - 100$ meV. Its unique tracker-calorimeter technology allows for the reconstruction of the 3D topology of the detected event, providing both a powerful background rejection method and evidence for the underlying decay process. The baseline design of SuperNEMO contains 20 identical planar modules, housing 100 kg of source isotope in total. The first module, the SuperNEMO Demonstrator, has been installed at LSM with the aim of reaching zero background in the region of interest for the $0\nu 2\beta$ decay of ^{82}Se . This target placed challenging demands on the radiopurity of detector components, in particular, the radon (^{222}Rn) activity within the tracker. All internal detector components and construction materials are screened for radon emanation to minimise radon levels.

5.1 SuperNEMO Baseline Design

In the baseline design of the SuperNEMO experiment, all 20 modules are fully operational independent detectors. Each module is 6 m long, 4 m high, and 2 m wide. In the centre of the module, there are thin source foils containing 5 - 7 kg

of source isotope with an areal density of $\sim 40 \text{ mg/cm}^2$. And they are made into very thin foils to avoid secondary scattering. The source foil is sandwiched by the tracker, which is a drift chamber operating in Geiger mode, capable of detecting charged particles and recording their 3D tracks. A magnetic field is applied to the tracker to curve the charged particles, except alpha which is too heavy. The tracker chamber is then enclosed by the calorimeter walls, containing 500 Optical Modules (OM) consisting of PMTs and scintillator blocks. The principle of the Demonstrator is illustrated in Figure 5.1.

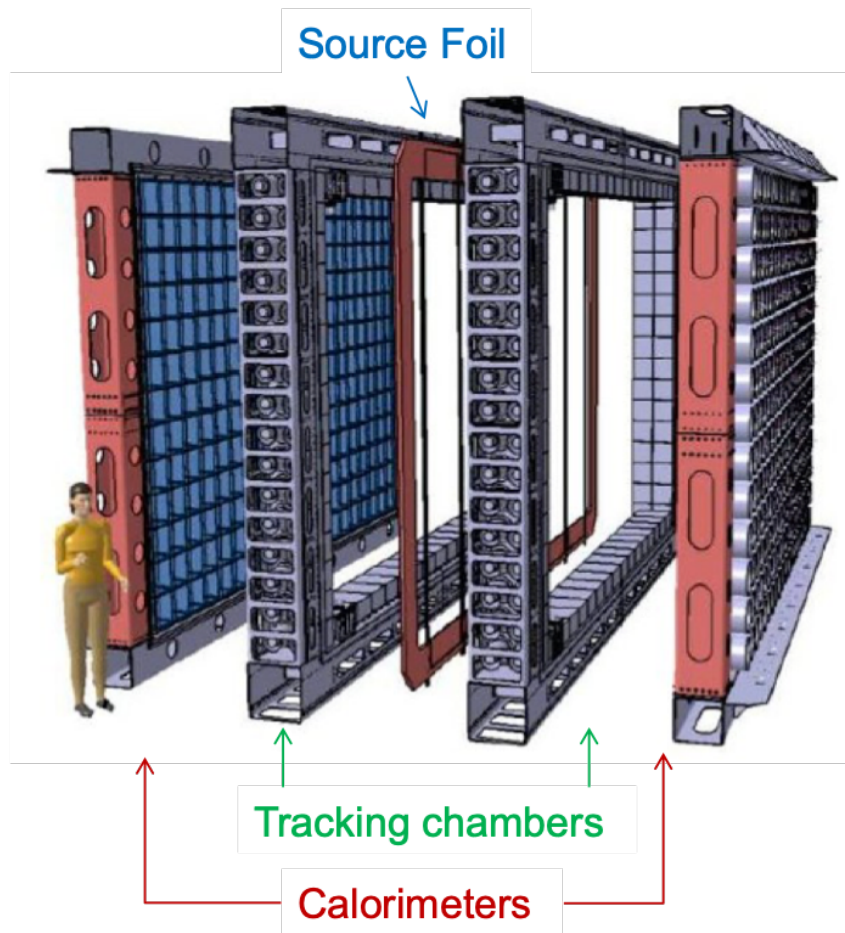


Figure 5.1: Exploded view of the SuperNEMO demonstrator module with source foil in the centre surrounded by the tracking chambers on both sides, followed by the calorimeters.

5.2 Source Foil

As the design of SuperNEMO is such that the source is separated from the detector, it allows for the measurement of different isotopes as it is possible to extract and exchange the source foil for one of a different isotope. The transition energy $Q_{\beta\beta}$, NME, phase space, natural abundance, and the feasibility of purification and enrichment are the major considerations when choosing the isotope for an experiment. For SuperNEMO, ^{82}Se was primarily selected. The source isotope, ^{82}Se , was enriched using the centrifugation method in Russia and then used to produce source foils at LAPP (Annecy) and ITEP (Moscow). The radiopurity requirement of the source foil is the most strict of all components on account of its central location: $A(^{214}\text{Bi}) < 10 \mu\text{Bq/kg}$, $A(^{208}\text{Tl}) < 2 \mu\text{Bq/kg}$. To confirm this level of radio-purity has been achieved, a dedicated detector known as the BiPo detector was built [81] which can measure the background via BiPo coincidence between an electron and a delayed alpha particle (see Section 9.2).

5.3 Tracker

The Demonstrator tracker is a drift chamber containing over 2000 wire drift cells operating in Geiger mode. The composition of the tracker gas mixture is 95% helium, 1% argon, and 4% ethanol. The drift cells are arranged in nine layers parallel to the foil. Each cell has a $40 \mu\text{m}$ stainless steel central anode wire surrounded by twelve $50 \mu\text{m}$ field wires, with a cathode pickup ring at each end. A 25 G magnetic field is used to reject positron events from the external background. Since a large number of wires are used in the chamber, the radio-purity requirement of the wires should be stringent. The wires were produced using the automatic wiring robot in Manchester, then the cassette of the wires are inserted into the tracker at UCL-MSSL (see Figure 5.2 and Figure 5.3).

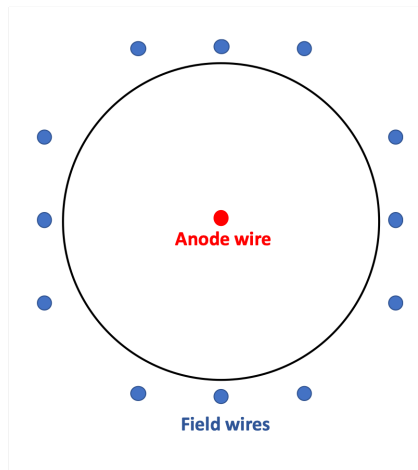


Figure 5.2: Sketch of a tracker Geiger cell from transverse view. The anode wire is drawn in the centre, and the 12 field shaping wires are all around.

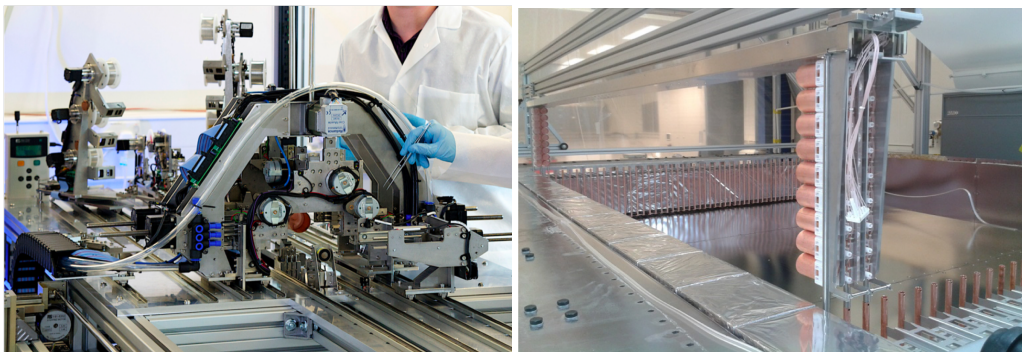


Figure 5.3: (left) Tracker cell production using the wiring robot. (right) The tracker wire cassette insertion at MSSL.

5.4 Calorimeter

The critical functions of the Demonstrator calorimeter are to measure the energy and the time-of-flight (TOF) of particles, and to provide a fast trigger signal. The Demonstrator calorimeter contains 550 OMs on the main calorimeter wall, 64 OMs on the veto at the top and bottom of the tracker chamber, and 128 OMs on the cross-wall (X-wall) at two sides of the tracker chamber. Each main wall OM has a scintillator block with a cross-section of $26\text{ cm} \times 26\text{ cm}$ coupled to a low radioactive 8-inch Hamamatsu R5912 PMT, as shown in Figure 5.4. The veto and X-wall OMs use 5-inch Hamamatsu R6594 PMTs recovered from NEMO-3, coupled to scintillator blocks. Dedicated studies have shown that this design can reach an energy resolutions of 4% FWHM at 3 MeV [82], which is a factor of 2 im-

provement compared to NEMO-3. The improved energy resolution can reduce the background by decreasing the overlap of the spectra of $2\nu 2\beta$ and $0\nu 2\beta$ events, which can not be distinguished from each other by reconstructed event topology.

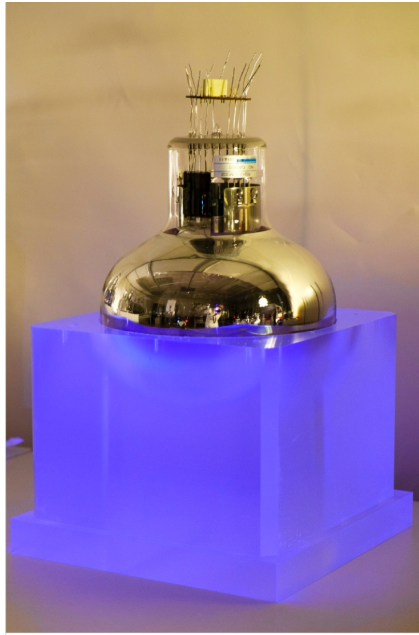


Figure 5.4: An optical module of the calorimeter consists a photomultiplier tube which is directly coupled to a scintillator block.

5.5 Readout Electronics and Data Acquisition System

The data acquisition rate for SuperNEMO is very low comparing to collider experiments. The trigger and data acquisition system for the tracker and calorimeter are inter-dependent. The calorimeter front-end boards determine timing as the calorimeter is much faster than the tracker. The tracker is then synced to the calorimeter clock. This is not only for the triggering and data collection for double-runs, but also for calibration runs and background studies. A block diagram of the SuperNEMO readout electronics can be seen in Figure 5.5.

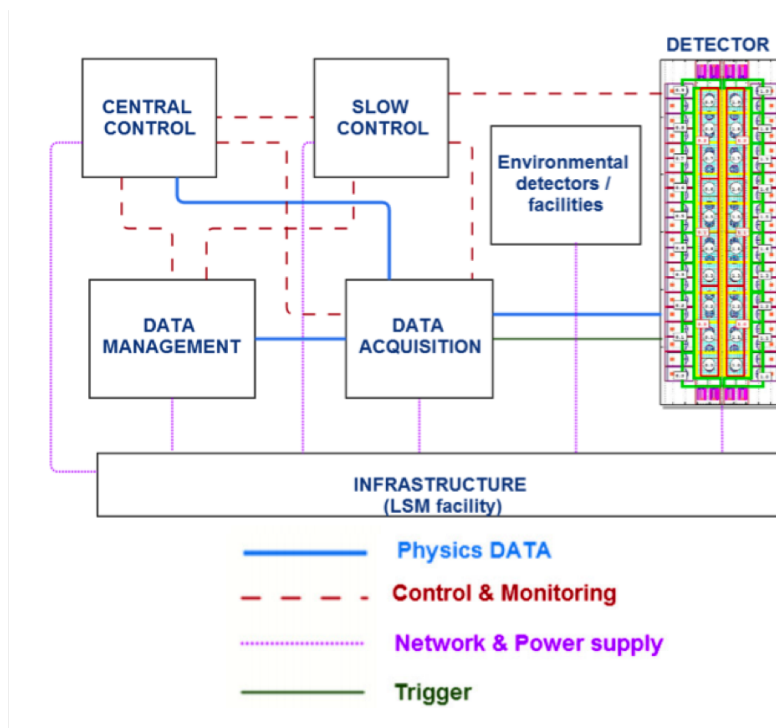


Figure 5.5: Schematic of the SuperNEMO readout electronics [43].

5.6 Shielding

5.6.1 Radon Shielding

The detector is isolated from the external environment for low background consideration. The tracker is tightly sealed together with the calorimeter and the detector mainframe using selected materials which are good radon barriers, such as nylon film and SBR. Thorough leak tests are then carried out, and all leaks are sealed using styrene-butadiene rubber (SBR) [43]. In front of the calorimeter wall, there is a layer of nylon film to reduce radon diffusion from the calorimeter into the tracker. The thickness of the nylon films, $25 \mu\text{m}$, was selected in particular to prevent loss of energy resolution due to multiple scattering of electrons in the film.

5.6.2 Anti-radon Factory

The average radon level at LSM is 15 Bq/m^3 [83], which mainly comes from the radon emanation of the surrounding rocks. To prevent radon diffusion, the Demonstrator is housed in an anti-radon tent, which is continuously flushed with filtered air. The air is filtered through two radon trapping columns, 0.6 m and 3 m high, filled with 500 kg of activated charcoal cooled to -50°C . The anti-radon facility filters air at a rate of $150 \text{ m}^3/\text{hr}$, and the absorbed radon will naturally decay away inside the columns. The radon levels in the anti-radon tent are reduced by $\sim 10^3$ compared to the environmental radon level, dropping down from 15 Bq/m^3 to 0.0018 Bq/m^3 [43].

5.6.3 Passive Shielding

The Demonstrator is housed inside the Modane Underground Laboratory (LSM) beneath the Frejus mountain, where under 1700 meters of rock (4800 m.w.e.) the cosmic muon flux is reduced by $\sim 10^6$, down to $4 \text{ events/m}^2/\text{day}$. While cosmic muons themselves do not directly contribute to the background due to their distinct event signature, they can produce neutrons from spallation.

In addition, gamma rays and neutrons are present from nuclear decay in the surrounding rocks under the mountain. The neutrons can undergo neutron capture on various parts of the detector frame, producing up to 10 MeV gammas. The gamma rays can interact with the source foil and cause the emission of two electrons (or positrons) via three processes: pair creation, Møller scattering and Compton scattering (see Figure 6.2).

The external shielding was constructed to prevent the background from the surrounding environment. Iron, 20 cm in thickness, will be used to stop external γ s, with water shielding for neutrons outside of the iron. Some studies indicate that borated water or sheets of borated polyethylene constitute better shielding against neutrons [82], but is also more expensive. A completed SuperNEMO module with

the external shielding is shown in Figure 5.6.

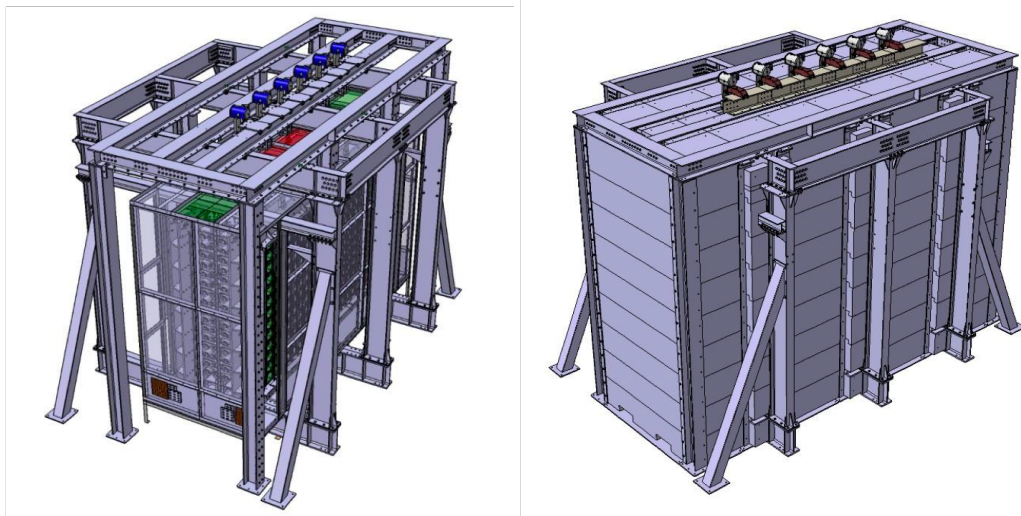


Figure 5.6: (left) Schematic of the SuperNEMO demonstrator module in the Anti - Radon tent. (right) Schematic of the SuperNEMO demonstrator module with all external shielding [84].

5.7 General Analysis Techniques

5.7.1 The SuperNEMO software

The SuperNEMO collaboration has developed a series of software packages for simulation, reconstruction, and analysis, including three major components: Cadfael [85], Bayeux [86], and Falaise [87].

- Cadfael is a software development kit which gathers the software packages needed for the development of SuperNEMO, including Boost [88], ROOT [89], Camp [90], CLHEP [91], Xerces [92], Geant4 [93], Doxygen [94] and Qt5 [95], which are all popular packages in nuclear and particle physics.
- Bayeux holds a C++ library for experimental nuclear and particle physics, which contains many C++ classes and functions designed for event simulation, data taking, and data analysis [82]. This functionality is split into several specialised submodules including:

- data handling: serializable data structures based on Boost (data tools), a basic data processing pipeline API (dpp), and data selection (cuts).
- numerical tools: C++ wrapper and extensions to the GNU Scientific Library (mygsl).
- utilities for GEANT4 simulation: definition of the primitive geometrical volumes (geomtools), database of the elements and isotopes composing the detector (materials), modelling of the electromagnetic field applied in the tracker (emfield), definition of the primitive geometrical volumes (geomtools), database of the elements and isotopes composing the detector (materials), nuclear database describing the kinematics of the radioisotopes (genbb_help, a C++ port of Genbb/DECAY0 from Vladimir Tretyak [96]), and a random generator of the vertex (genvtx).

Cadfael and Bayeux were particularly designed for the SuperNEMO experiment by the collaboration, but now they are also used by other nuclear and particle physics experiments [82].

- Falaise depends on Cadfael and Bayeux. It provides the main computational environment for the simulation, algorithms of reconstruction, processing and analysis of data for the SuperNEMO experiment. It consists of three major parts: a core library called libFalaise, a main detector simulation tool called flsimulate, and the main reconstruction tool called flreconstruct.

The complete analysis procedure can be compared to a pipeline where events flow through, starting with the simulated or the real recorded data, followed by the reconstructed data, and ends with the analysed data [82].

5.7.2 Sample Simulation and Reconstruction

Falaise is capable of virtually reproducing the geometry, materials, and physical conditions of the detector, and simulating the steps and processes of an event — this process is called simulation. Event simulations are generated by GENBB, with the propagation of the particle inside the reconstructed SuperNEMO detector being carried out by GEANT4 [93].

GENBB is a Monte-Carlo event generator for 2β processes and the decay of radioactive nuclei and contains information relating to decays — including the half-life, energy, decay mode, and probability — of all known isotopes. It is capable of generating nuclear decay events and providing information with regard to the decay energy, time, and direction of the emitted particles [93, 96].

The detector geometry, materials and physical conditions are reproduced virtually thanks to Geant4. Under this environment, it is possible to simulate the physics process in the detector. For a typical double beta decay event from the source foil, its vertex is generated randomly within the source volume, and the kinematics is also generated randomly according to the specific probability distribution function for the process given by the existing database. The two electrons propagate in the detector volume following the Monte-Carlo procedure. Each particle is propagated step by step, and the length of each step is subject to the materials and physics conditions. The interactions which can affect the length of a step, like decays and scattering, are implemented in the software, and the step length is randomly simulated according to these interactions. Possible secondary particles generated in the interactions, for example, a Møller electron or γ from Bremsstrahlung are also simulated. The simulation will stop if a previously defined criterion is met, such as the low energy cutoff, particle entered no-defined volume, etc.

Figure 5.7 shows a simulated $2\nu 2\beta$ event. Each circle represents a hit on the tracker cell. The centre of the circle locates on the anode wire of the cell, and

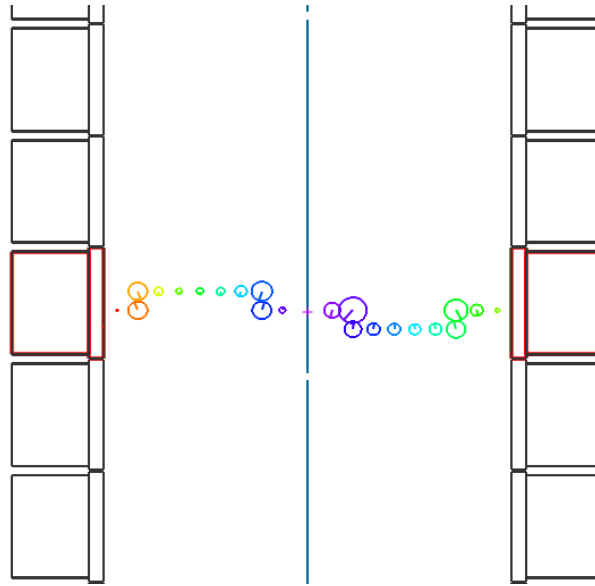


Figure 5.7: Visualisation of a simulated $2\nu 2\beta$ event in the SuperNEMO demonstrator from the top view. The calorimeter PMTs, the side and top scintillator blocks and the tracker cells are not represented for the sake of readability. The source is displayed in blue, and the different source pads are distinguishable. The scintillators are displayed in grey. The coloured circles represent the tracker cells where the two simulated electrons have crossed. The centre of the circle locates on the anode wire of the cell, and its radius represents the minimum distance between the particle track and the anode wire. The colour of the circle is related to the time when the particle hits the cell.

its radius represents the minimum distance between the particle track and the anode wire. The colour of the circle is related to the time when the particle hits the cell. It should be noted that the simulation is based on the assumption of ideal detection efficiency and time resolution of the tracker. In reality, not all the hit cells considered by the simulation will be triggered by the particle because the detection efficiency decrease from the central anode wire to the edge of each cell (but still remains above 99%). Also, due to the stochastic nature of the Geiger cell, the radii are only known associated with uncertainty so that it is almost possible to arrange hit cells by time. The electron goes through the tracker in several nanoseconds, but it takes microseconds for the avalanche created and the plasma propagation towards the cell. The red box on the calorimeter blocks represents that the energy deposited in the scintillator. All the simulated event

information are stored in the Simulated Data bank (SD bank). The simulated or real data will then go through a succession of algorithms, each striving to improve comprehension of the events and to reconstruct them accurately.

To match the real data, the running conditions should be considered in the simulation: the PMT gains, dead Geiger cells, dead PMTs, and ageing of the detector. Therefore pseudo-calibration are carried out at this stage, and the event information is saved in the Calibrated Data bank (CD bank).

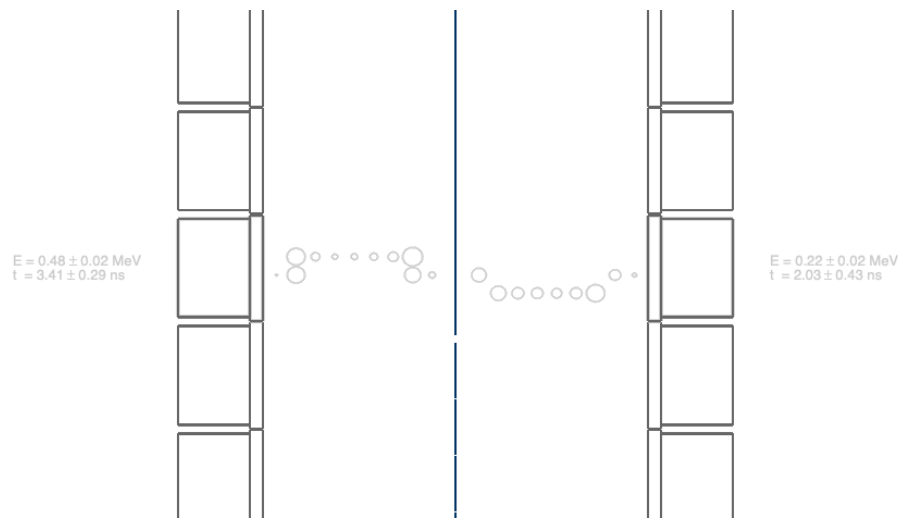


Figure 5.8: Visualisation of $2\nu 2\beta$ event from the top view, with information from the Calibrated Data bank. The chronological information of the tracker hits is not available.

Cellular Automaton Tracker Module

The first step in the reconstruction is to find out the number of charged particles in the event based on the tracker hits. This work is done by the Cellular Automaton Tracker (CAT) Module which can cluster all the neighbouring calibrated Geiger hits. It starts working from the inner layers of the tracker (close to the source), and then adds neighbouring hits layer by layer towards the calorimeter wall. If there are still unclustered hits, it starts another clustering job until all the hits are clustered. Particles crossing the foil will generate two separate clusters as a CAT cannot gather a cluster across the foil by definition. If a tracker hit is $10 \mu\text{s}$ later than the prompt signal given by the calorimeter hit, it will be iden-

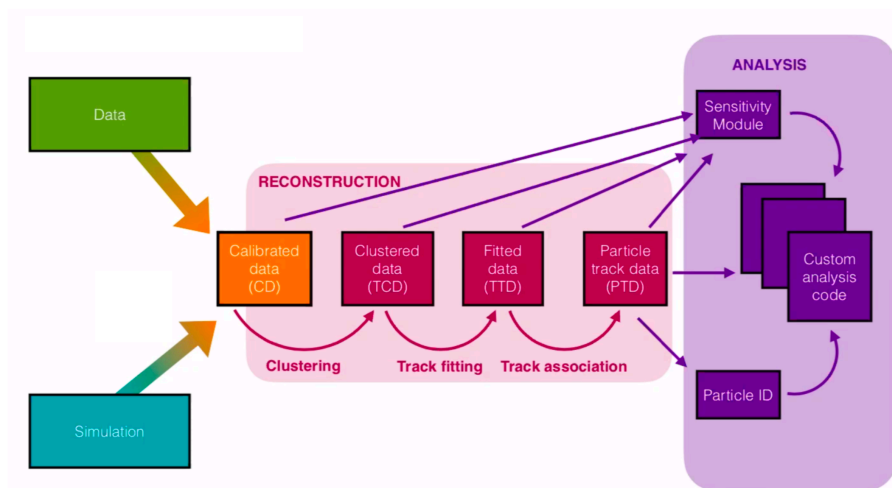


Figure 5.9: SuperNEMO software pipeline. Real data or simulated data flowthrough the reconstruction modules and then go into customised analysis module.

tified as a delayed hit. These delayed hits are usually from the alphas in the BiPo events ($^{214}\text{Bi} \rightarrow ^{214}\text{Po} \rightarrow ^{210}\text{Pb}$, see Figure 9.1). Tracker hits occurring after this time window will be recorded by a second trigger and acquisition system. Figure 5.10 shows the clustered hits of electrons from a $2\nu 2\beta$ event. Different clusters are represented by a different colour in event visualisation. This information fills up the Tracker Clustering Data bank (TCD bank).

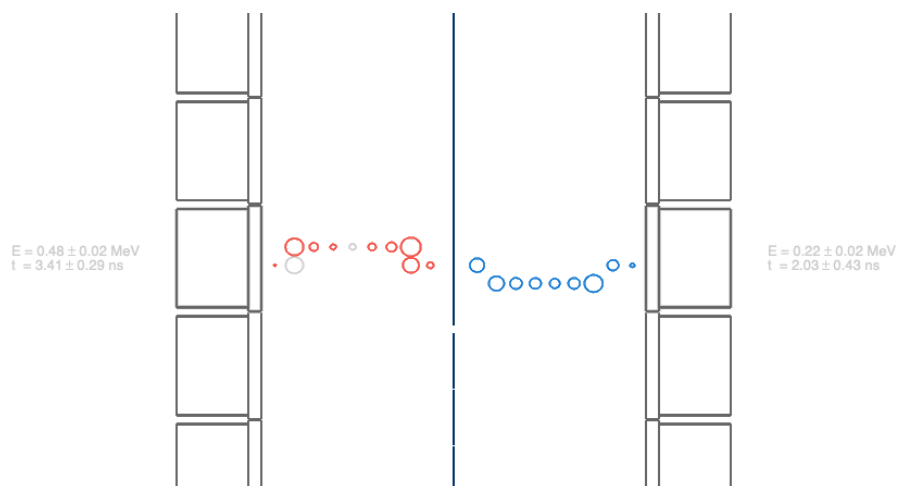


Figure 5.10: Visualisation of a $2\nu 2\beta$ event from the top view, with information from the Tracker Clustering Data bank. Tracker hits clustered and represented by a specific colour if they are from the same cluster.

Track Trajectory Module

The clusters found by CAT are fitted to a trajectory by the Tracker Trajectory Module. This module only processes the clusters with 3 or more Geiger hits. During this trajectory fitting step, different patterns, both helices and straight lines, are tested because the 25 Gauss magnetic field is not strong enough to bend high energy electron tracks or alpha particles. The best fit is chosen according to the lowest χ^2/ndof , shown in Figure 5.11. For delayed clusters, straight-line fitting is applied, and the radius is one-fourth of the total radius of the cell by construction. All information processed by the fitting trajectory step is stored in Tracker Trajectory Data (TTD) bank.

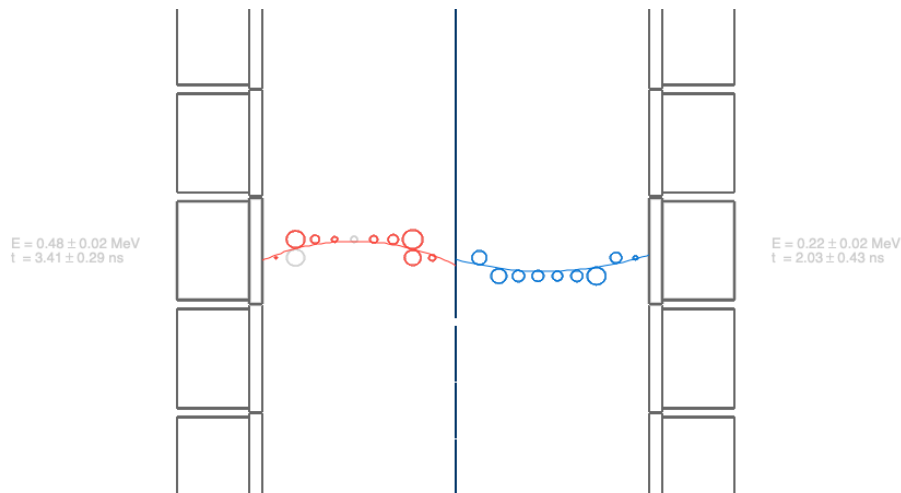


Figure 5.11: Visualisation of a $2\nu 2\beta$ event from the top view, with information from the Track Trajectory Data bank. Clusters found by CAT are fitted to a trajectory.

Charged Particle Tracking Module

Charged particle tracks fitted by the tracker trajectory module are processed to the next step where the tracks will be resituated in the SuperNEMO detector. The tracks are extrapolated both to the calorimeter walls and the source in an attempt to find a possible associated calorimeter hit and to locate the vertex of the event respectively. Based on the assumption that particles travel from the source towards the calorimeter, it is possible to extract the charge of the particle from the curvature of the track. Figure 5.12 shows the two negatively charged electrons in a $2\nu 2\beta$ are associated with their corresponding calorimeter hits, and the vertex is found in the source.

Alpha particles coming from the BiPo events are mostly delayed with respect to a prompt electron. The clustering algorithm can not process these delayed tracks. As there is no calorimeter hit which can provide a reference time, it is impossible to calculate the drift radii. The longitudinal coordinate is reconstructed according to the anode time when the initial avalanche reached the anode. Straight-line tracks are fitted to the delayed tracker cells, and the drift radius is set as one-fourth of the total radius of the cell. The information processed by the charged particle tracking module is stored in the Particle Track Data (PTD) bank.

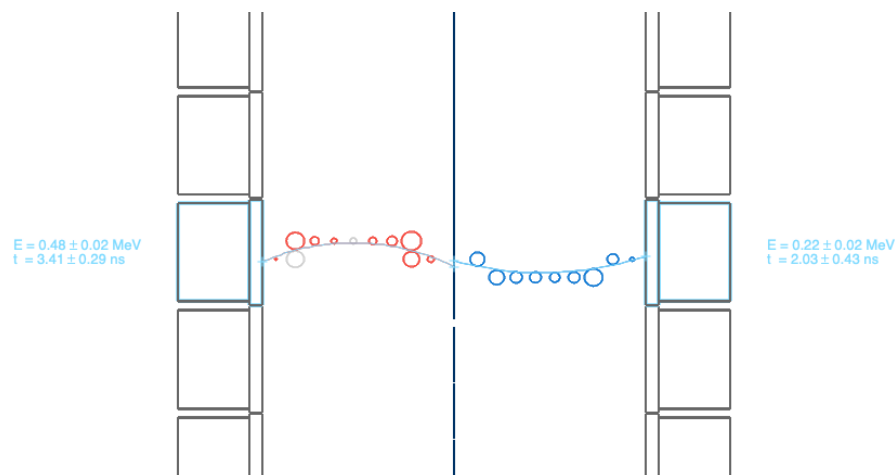


Figure 5.12: Visualisation of a $2\nu 2\beta$ event from the top view, with information from the Particle Track Data bank. Tracks are extrapolated both to the calorimeter walls and the source to find a possible associated calorimeter hit and to locate the vertex.

Sensitivity Module

Sensitivity Module [97], is a customised output module for the storing of simulated and reconstructed data from the SD, CD, TCD, TTD, and PTD banks in a ROOT ntuple file.

The reconstructed particles are identified according to definitions given by the user, see Figure 5.13 [82]:

- **Electron** has a negatively curved track with an associated calorimeter hit.
- **Position** has a positively curved track with an associated calorimeter hit
- **Alpha** has a short straight track (normally being delayed).
- **Gamma** has one or more unassociated calorimeter hits.

After all the particles in an event are identified, they can be associated to form a topology. Then a number of observables can be computed based on different topologies, such as:

- the angle between the particles.
- the distance between the source vertices of charged particles.
- the delayed time between the prompt electron and delayed alpha.

5.7.3 Alpha Finder

Alpha particles come to a stop at a very short distance into the tracker due to their high ionisation power, and due to their high mass, and are not significantly affected by the magnetic field. As such, the typical signal of an alpha particle is a short straight track (typically less than 40 mm) and, if it comes from the foil, has no associated calorimeter hit.

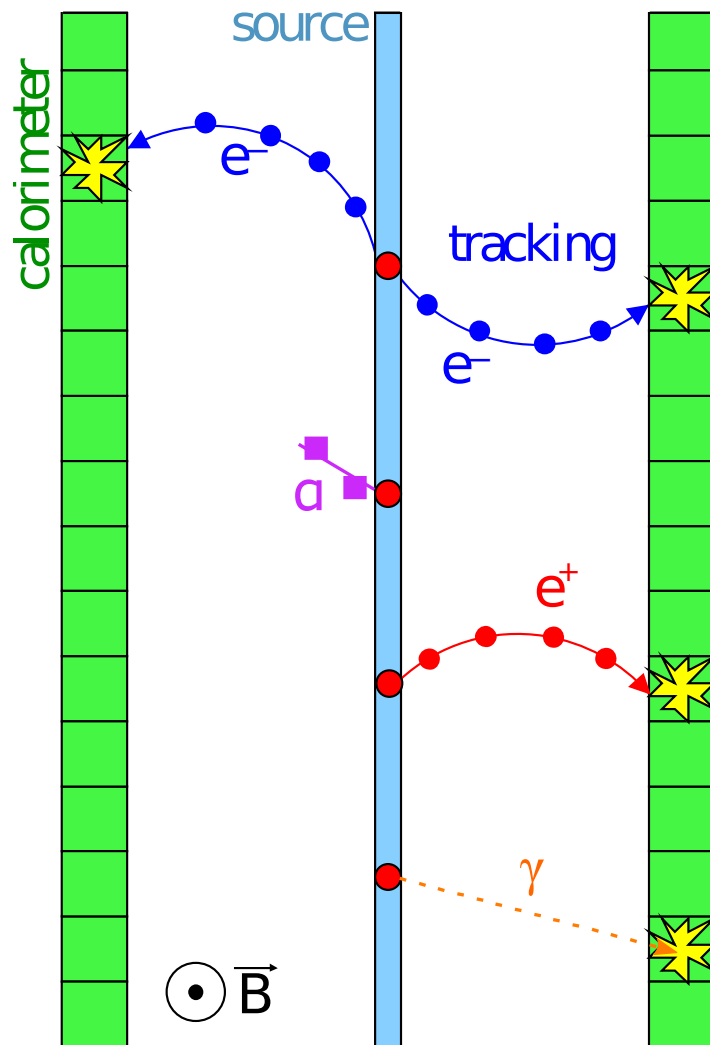


Figure 5.13: A sketch of particle topologies in the SuperNEMO detector [82].

For alpha particles which hit 3 or more Geiger cells (see Figure 5.14) the tracks are treated as normal by CAT: Centres of the cells in the delayed cluster are connected with a straight line of best-fit, and in cases where the projection of the line intercepts the foil, the track is extended to the foil. The track will not be connected to other particles, such as the prompt electron.

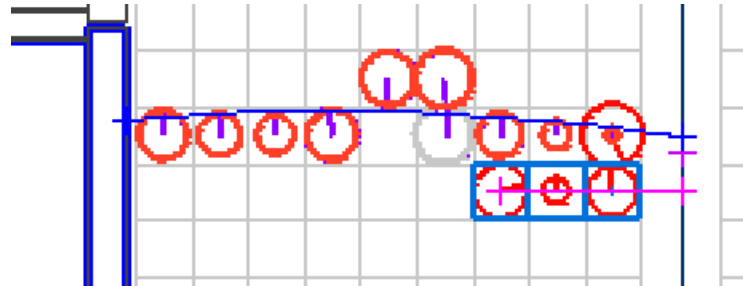


Figure 5.14: Visualisation of a $1e1\alpha$ event where the α hits 3 tracker cells. The centre of the 3 hit cells are connected and extrapolated to the foil in attempt to locate the α vertex.

Some alpha particles will hit only 1 or 2 Geiger cells in the tracker, and cannot be processed by the TrackFit module. Because such an alpha particle will not trigger the SuperNEMO detector itself, to identify the alpha event, a prompt electron is required for verification, as during data taking, a 1 ms window will open after a calorimeter hit is triggered by a prompt track. In the event a prompt track is present, the existence of delayed unfitted tracks (a 2-hit cluster) or a delayed unclustered Geiger hit (a single hit) can be verified. These alphas are found by the Alpha Finder algorithm.

In the event an alpha particle hits 2 Geiger cells, the centre of the furthest cell hit is connected to the vertex of the prompt electron track to construct a track (see Figure 5.15).

In the event the alpha particle hits only 1 Geiger cell, the centre of the cell is connected with the delayed hit to the closest end of a prompt electron track (see Figure 5.16).

All alphas are treated equally during the analysis, regardless of the way they were found.

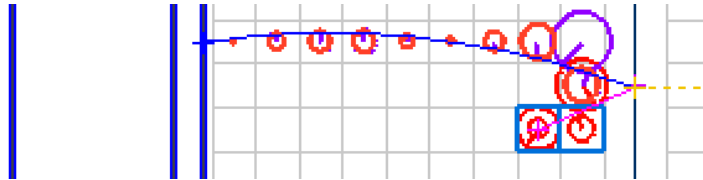


Figure 5.15: Visualisation of a $1e1\alpha$ event where the α hits 2 tracker cells. The centre of the furthest α hit is connected to the vertex of the prompt electron track to construct an alpha track.

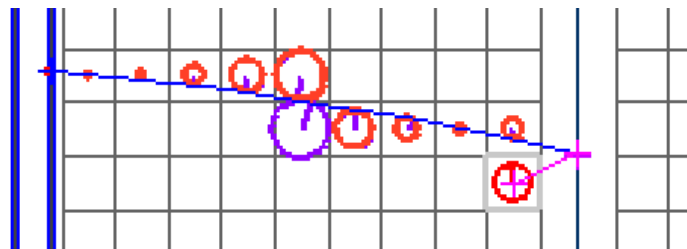


Figure 5.16: Visualisation of a $1e1\alpha$ event where the α hits only one tracker cells. The centre of the cell is connected with the delayed hit to the closest end of a prompt electron track.

Chapter 6

Radon and SuperNEMO Sensitivity

In the SuperNEMO experiment, a double beta decay signal is characterised by the observation of two electrons from the same location in the source foil. In addition, the $0\nu\beta\beta$ requires the total energy of the two electrons meet $Q_{\beta\beta}$ of the isotopes (2.99 MeV for ^{82}Se). Therefore, any process that can mimic this signal will contribute to the background of the experiment. The sensitivity of SuperNEMO is directly related to the background level (as discussed in Chapter 4), thus it is essential to reduce the background and to measure the residual background accurately. One unavoidable background is from the $2\nu\beta\beta$ process when considering $0\nu\beta\beta$ as the signal only. The $2\nu\beta\beta$ process is observed across the entire energy spectrum, and its high energy tail becomes a background to the $0\nu\beta\beta$ observation. The only practical way to suppress this background is to improve the energy resolution.

6.1 The SuperNEMO Backgrounds

The main sources of background for SuperNEMO are trace amounts of radioactive isotopes in all materials. β -decay isotopes inside the source foils are generally the most problematic, whereas γ -emitting isotopes mostly contribute to the external background. Almost all radioactive isotopes are background to $2\nu\beta\beta$ searching, but only isotopes with high Q_{β} values contribute to the background of

$0\nu\beta\beta$ searching. The two most problematic isotopes are the β -decaying isotopes ^{214}Bi ($Q_\beta = 3.27$ MeV) and ^{208}Tl ($Q_\beta = 4.99$ MeV) from the ^{238}U and ^{232}Th decay chains respectively which are shown in Figure 6.3).

The SuperNEMO backgrounds can be classified into three types: internal backgrounds, external backgrounds, and radon background.

6.1.1 Internal Background

Internal backgrounds originate from inside the source foils, and thus they are dominated by the radioactive contaminants in the foils. The β -decay isotopes are most harmful because they can mimic two electron events via the processes of β -decay with Møller scattering, β decay followed by internal conversion or β -decay to an excited state with Compton scattering of the de-excitation photon, as shown in Figure 6.1.

To monitor the internal backgrounds, all the source foils are measured by the HPGe detectors prior to installation into the SuperNEMO detector. The in-situ activity measurements made by the SuperNEMO will be directly compared with these HPGe measurement results. From these HPGe measurements and by considering commonly-found naturally occurring isotopes, the list of expected contaminants is comprised of ^{214}Bi , ^{214}Pb , ^{208}Tl , ^{212}Bi , ^{228}Ac , ^{234m}Pa and ^{40}K [31]. Most of these isotopes are from the ^{238}U and ^{232}Th decay chains except ^{40}K .

6.1.2 External Background

External backgrounds refer to those from anywhere in the detector other than the source foils and that are not radon-induced. In order to mimic two electron events, external backgrounds usually involve a photon that interacts with the source foil, as shown in Figure 6.2. In the case of pair production, the outgoing positron must also be misidentified as an electron, which is unlikely given the magnetic field. Electrons that do not interact in the foil, but cross the detector, can also be mistaken for two electron events. However, these crossing

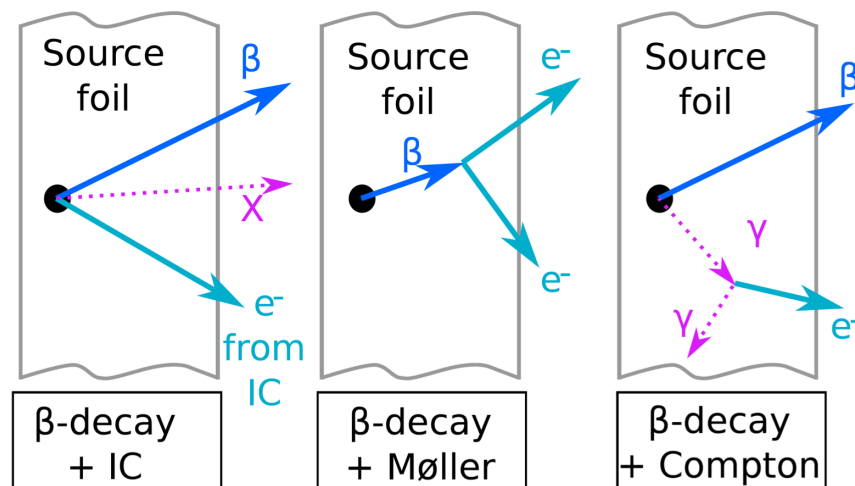


Figure 6.1: Three dominant processes via the β -decay isotope contamination in the source foil, leading to the emission of two electrons, which contributing to internal background [82].

electrons are heavily suppressed by removing events based on their timing information. External background is predominantly from the radioactive decay within the rock surrounding the laboratory, neutron capture and decays within the detector components themselves.

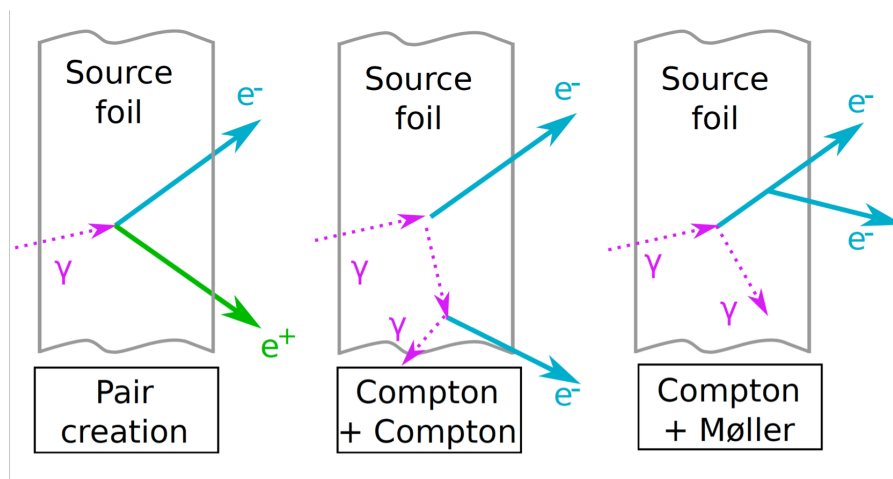


Figure 6.2: Three dominant processes of production of two electrons from an external particle interacting with the source foil [82].

6.1.3 Radon Background

The third type of background is radon-induced background. The radon background is originally from radon in the tracker gas. Radon progenies can be deposited on the source foil surface, thus effectively becoming internal backgrounds. The radon level inside the detector can be measured in situ by studying BiPo events as described in Chapter 9.

6.2 The Property of Radon

Radon is a colourless and odourless noble gas with the symbol Rn and atomic number 86. It is the only gas that consists entirely of radioisotopes.

Friedrich Ernst Dawn first reported the discovery in 1900 in a series of experiments where radium compounds emitted a radioactive gas [98]. Later in 1904 and 1910, William Ramsay isolated the gas and studied its properties at University College London [99, 100], discovering that the spectrum of this gas and its low-level chemical interaction were similar to those of argon, krypton, and xenon. Eventually, after a series of suggestions, this new element was named as radon in 1923.

All 36 radon isotopes that have been characterised are radioactive, with only four of them being found in nature. The most stable radon isotope, ^{222}Rn (half-life 3.8235 days), is from the ^{238}U decay series (see Figure 6.3).

In addition, there is another important radon isotope — ^{220}Rn (half-life 51.5 seconds) from the ^{232}Th decay series. For $0\nu\beta\beta$ decay experiments, ^{222}Rn and ^{220}Rn are of interest as they provide ^{214}Bi and ^{208}Tl due to their high Q_β values. The simplified decay schemes are shown in Figure 6.4 and Figure 6.5.

Radon, as a noble gas, has a full valence shell and is thus inert to most chemical reactions, making it difficult to remove chemically. Its long diffusion length in solids has posed a significant challenge to seal on a large scale. The diffusion

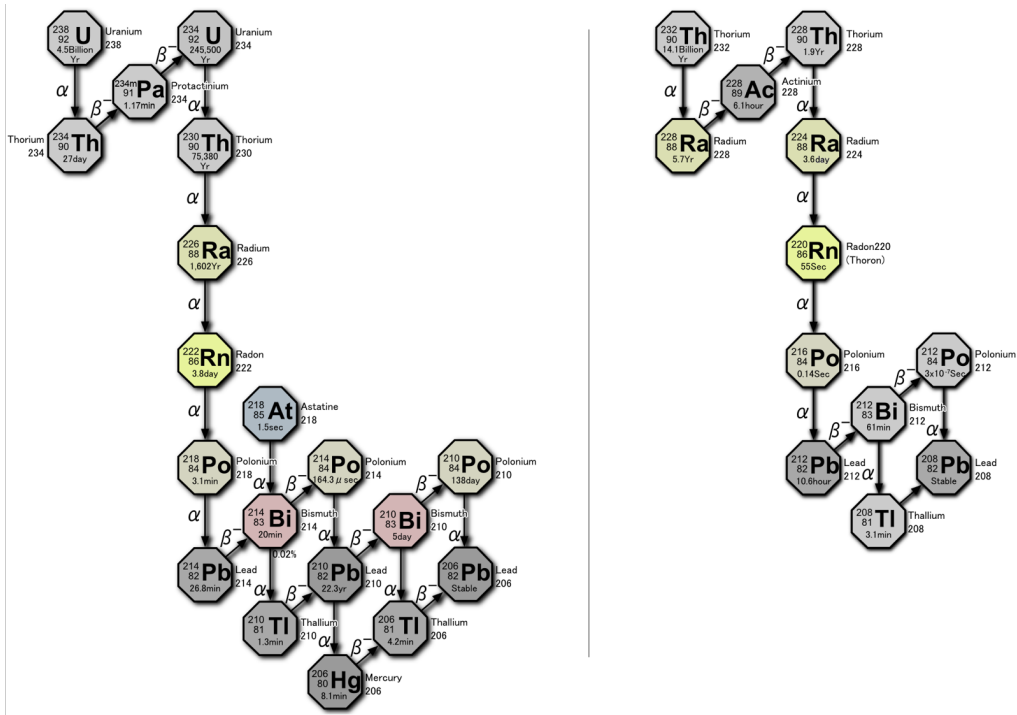


Figure 6.3: (left) Decay chain of ^{238}U [101]. (right) Decay chain of ^{232}Th [102].

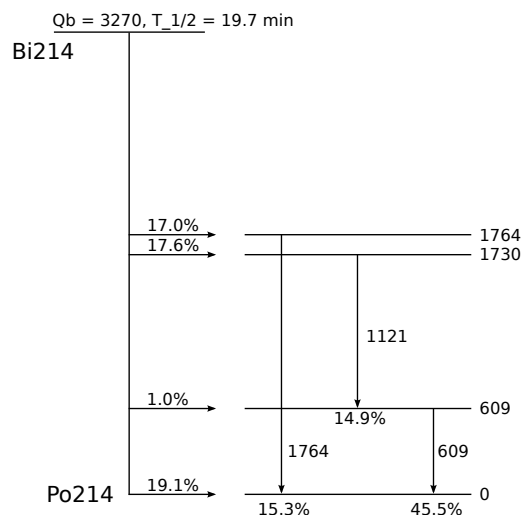


Figure 6.4: The simplified decay scheme for the decay of ^{214}Bi [31].

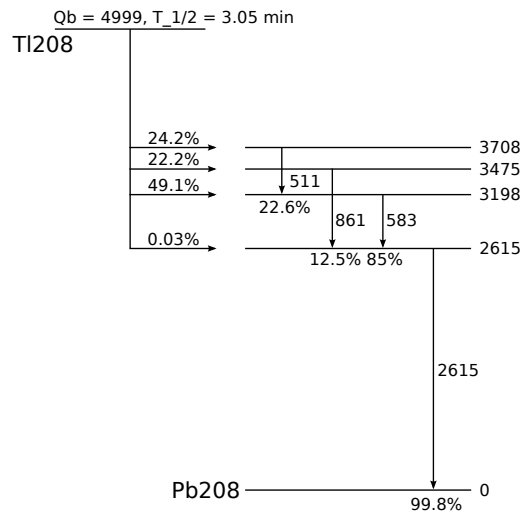


Figure 6.5: The simplified decay scheme for the decay of ²⁰⁸Tl [31].

length L is defined as:

$$L = \sqrt{\frac{D}{\lambda}}, \quad (6.1)$$

where λ is the decay constant and D is the diffusion coefficient of the material. Metals usually have minimal diffusion coefficients.

Some typical values of radon level are 1 - 100 Bq/m³ in the open air, and 30 - 50 Bq/m³ indoor. In the UK, the average radon level is 4 Bq/m³ in open air, and 20 Bq/m³ indoor [103]. These values are heavily dependent on the location, ventilation, and the surrounding materials and thus can vary dramatically. In a cleanroom, with the barrier from brickwork and active ventilation, the level can be reduced to < 5 Bq/m³. Radon levels in underground laboratories also vary depending on the surrounding rock, which can range from ~ 2 Bq/m³ in a salt mine to several kBq/m³ in a uranium mine [43].

Beyond experimental high energy physics, the study on radon has also become a general interest in public health. It is regarded as the second highest cause of lung cancer after smoking. Aside from radon itself, which is easily inhaled as a gas, the radioactive decay products are solid and can stick to the surface of dust in the air, which can in turn be breathed in. While there are extensive commercial

radon detection devices sensitive to an activity range of 0.1 Bq/m^3 - 1 Bq/m^3 , such sensitivity is far below the requirement for low background experiments. As such, a custom-made detector is required for the SuperNEMO experiment.

6.3 Radon in SuperNEMO

From the NEMO-3 experience, as the decay daughters of ^{222}Rn , ^{214}Bi contributes a large part to the background due to the high β decay Q_β value of 3.27 MeV. All materials are naturally contaminated with traces from the ^{232}Th and ^{238}U . Radon can enter the SuperNEMO detector generally via the following ways: emanation from the detector construction material and diffusion from the environment. The study on the effect of different radon concentrations on the sensitivity of SuperNEMO is shown in Figure 6.6. In the study, radon from the source foil and from the tracker are treated separately, and as such the radon budget of $280 \mu\text{Bq/m}^3$ for the sensitivity of 10^{26} yr is calculated with the assumption that the contribution from the source foil is 0. This being the case, the target of radon level should be divided between internal contamination and the tracker, resulting in a target for the tracker activity of $< 150 \mu\text{Bq/m}^3$. To achieve this target, various methods have been used to monitor and mitigate radon which effects as a major background: screening of the construction materials and components, purification of the tracker gas and in-situ monitoring of radon background levels.

6.4 Gas Flow Suppression of Radon in Tracker

Besides monitoring the radon contamination of material used in SuperNEMO, a sufficient improvement on the radon level in the tracker can be gained by replacing the contaminated tracker gas with clean gas. The diffused and emanated radon can be flushed away, creating a suppression that is, unsurprisingly, a function of flow rate and the activity of the supply gas. Naively, one may expect the flow rate to be as high as possible to reduce the radon activity, however, in reality this flow rate is limited. The tracker performance will decrease if the volume ex-

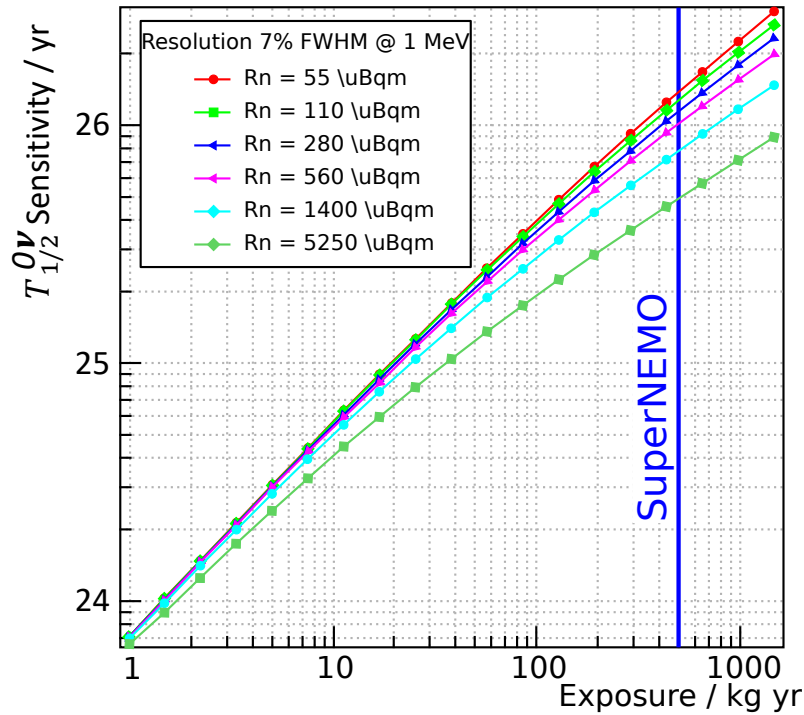


Figure 6.6: SuperNEMO sensitivity as a function of exposure for different radon activities inside the tracker. Internal contamination of ^{214}Bi is neglected [104].

change too fast. The accuracy of the gas mixing system which is introducing the required 4% ethanol into the tracker gas can also be affected by high flow rate. Studies showed a satisfactory performance of the tracker up to a maximum flow rate of $2 \text{ m}^3/\text{h}$ [105]. The flow rate is also limited by the ability of the gas purification system used to trap radon in the supply gas before being flushed into the tracker. To achieve effective suppression, an active gas purification system was developed, similar to the anti-radon factory, to purify the gas mixture of helium and argon prior to the gas mixing system delivering the correct concentration of tracker gas. The gas purification system is described in Section 7.5. The major part of the gas purification system is a trap which use activated charcoal to trap radon at -80°C , and, as it is known that ethanol can quickly saturate the trap and stop radon trapping, this gas purification system must not be installed post gas mixing system. As radon emanated from the gas mixing system will be delivered

to the tracker, the radiopurity of the gas mixing system should be minimised.

When radon level inside the sealed tracker reaches equilibrium, A_T , the number of radon atoms, N , is:

$$N_T^0 = A_T / \lambda \quad (6.2)$$

where λ is the decay constant. The suppression factor can be extracted by taking a ratio of the number of radon atoms inside the tracker with a certain gas flowrate and without flushing:

$$F_S = \frac{N_T}{N_T^0} = \frac{\lambda'_T}{A_T + A_G} \frac{A_T}{\lambda} = \frac{1 + f/V_T \lambda}{1 + A_G/A_T} \quad (6.3)$$

where N_T is the number of radon atoms inside the tracker while flushing, A_T is the activity of the tracker, A_G is the activity of the flushing gas, f is the flowrate, and V_T is the volume of the tracker. Here λ'_T is the effective decay constant: λ'_T :

$$\lambda'_T = \lambda + \frac{f}{V_T} \quad (6.4)$$

The radon suppression factor as a function of gas flow rate is shown in Figure 6.7 [31], in which three different radiopurities of gas are considered. When the radon level of the replacing gas is negligible, a suppression factor of 18.4 can be achieved by flushing at 2 m³/hr.

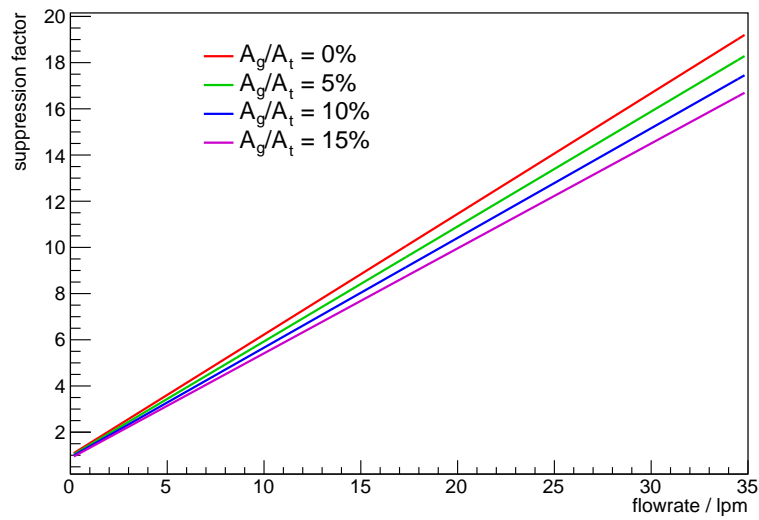


Figure 6.7: The radon suppression factor as a function of gas flow rate. Four different levels of radiopurity of the replacing gas are shown at 0%, 5%, 10%, and 15% [31].

Chapter 7

Radon Detection

The SuperNEMO experiment requires radon contamination of the tracker gas to be less than 0.15 mBq/m^3 , and achieving this target has posed a significant challenge in the detector design and construction. Furthermore, the measuring and monitoring of such ultra-low radon activity is also a challenging prospect. The world's best radon detectors can achieve a sensitivity of 0.1 Bq/m^3 [43], which is 3 orders of magnitude away from meeting the SuperNEMO tracker gas radiopurity requirement. As such, a state-of-art custom-made electrostatic detector has been acquired for SuperNEMO. Initially designed for the ELEGANT V and Super-Kamiokande experiments [106, 107], the detector is capable of measuring radon down to a level of $1 - 2 \text{ mBq/m}^3$ — 2 orders of magnitude better than commercial detectors. However, this is still ten times higher than the target sensitivity. A new system called the Radon Concentration Line (RnCL) has been developed and built at UCL, which can concentrate the gas sample so that the sample can reach the sensitivity required for the SuperNEMO detector. This is described in Section 7.4.

7.1 Electrostatic Detector

The electrostatic detector, as shown in Figure 7.1, consists of the following parts: a 70-litre cylindrical stainless steel detection chamber, a silicon PIN photodiode,

electronics associated with the detector, and two valves — inlet and outlet — for gas flow. To minimise the background, the chamber is electro-polished after welding to reduce the surface area onto which radioactive particles can be deposited. In addition, metallic valves coated with Styrene butadiene rubber (SBR) are used to prevent radon diffusion. The PIN photodiode is electrically isolated from the chamber by a perspex sheet and feedthrough, and is connected to the electronics, which include a high voltage divider and a pre-amplifier housed in the lid of the detector, separated from the chamber. The aim of this design is to provide shielding from external noise as well as to reduce the length of the signal cable before the pre-amplifier. Negative high-voltage, typically -1500 V, is applied to the P-layer of the PIN photodiode while the chamber is grounded, to generate the electrostatic field. Simultaneously, -100 V is separated to provide the inverse bias voltage to the PIN diode through a high voltage divider.

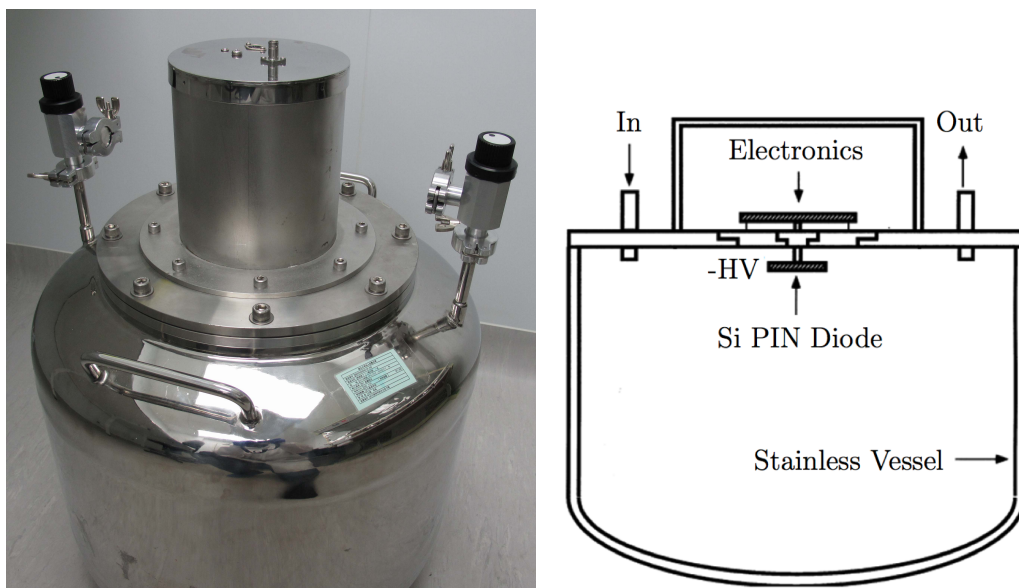


Figure 7.1: (a) The electrostatic detector used for all the radon emanation measurements along with the RnCL and the emanation chamber. (b) The electrostatic radon detector schematic as shown in [106].

The daughter nucleus of ^{222}Rn decay are predominately positively charged. A measurement taken in 1913 shows that 88% of the ions and compounds from radon decay are positively charged [108], which is consistent with the most recent measurement result, $87.3 \pm 1.6\%$ [109].

Due to the applied electric field, positive ions from radon decay are attracted onto the PIN photodiode. When these ions undergo α decay, they can be detected by the photodiode, and distinguished by the energy deposited on the PIN: 6.1 MeV, 7.9 MeV, and 5.4 MeV for ^{218}Po , ^{214}Po , and ^{210}Po respectively. ^{214}Po has a higher detection efficiency and is generally considered as a measure of radon level. Ideally, one may expect that the collection efficiencies for ^{214}Po and ^{218}Po to be the same; however, not 100% of decay daughters are collected due to neutralisation. The ^{218}Po which has a higher ionisation potential, is more easily to be neutralised in the environment where only trace amount of impurities are present. ^{210}Pb has a relatively long half-life of 22.3 yrs; hence its daughter nuclei ^{210}Po , will not reach equilibrium with the ^{222}Rn within the time frame of a typical measurement, and it will not characterise the radon concentration.

7.1.1 Detector Signal

The detector signal is passed to the DAQ system: a Nuclear Electronics Miniature box (Wiener NEMbox SU706), which is a field-programmable gate array (FPGA) designed to function as a NIM crate in a small, stand-alone desktop unit. The NEMbox is used to trigger and digitise the pulses for storage, and at the same time, can prevent re-triggering from the afterpulse. The dead time for this system while recording the full signal pulses to disk for offline analysis is ~ 17 ms. A calibrated source of known frequency was used to measure the response of the DAQ system, and the results are as shown in Figure 7.2. In normal data-taking modes, the dead time should contribute a negligible effect, however, for high activity measurement such as a calibration run, it must be taken into account [31].

7.1.2 Detector Efficiency Calibration

The detection efficiency of the electrostatic detector was calibrated to investigate the response of the detector to a known activity of radon. A 1.32 kBq ^{226}Ra

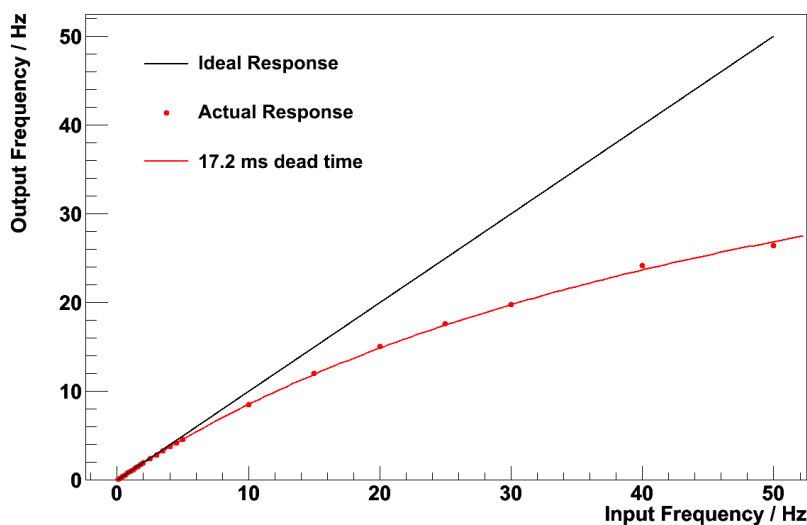


Figure 7.2: Response of the DAQ system for various input frequencies, where the red dots show the measured response, and the red line shows the expected response when the dead time between two pulses is 17.2 ms [31].

flowthrough standard source (Pylon Electronics, RN-1025) was procured for this calibration. The design of the source allows the gas to flow through the source material, which can ensure that all the emanated radon is exhausted and offer considerable flexibility in the amount of radon for different measurement uses. There are generally two separate methods to calibrate the detector. The first, dubbed the spike method, is to purge a known amount of radon into the detector and measure the activity with the detector. The second, the flowthrough method, is to measure the radon level inside the detector while continuously flushing the radon-carrying gas through the detector over 24 hours. Though both helium or nitrogen can be used as the carrier gas, helium is the preferred choice in this case as impurities in the nitrogen such as nitrous oxides may result in neutralisation of positive ions of radon progenies [110]. The detection efficiency was determined by taking the ratio of the measured activity of radon in the detector chamber over the calculated radon activity introduced from the flowthrough source. In the latest spike method calibration measurement (the spectrum for which is shown in Figure 7.3), for ^{214}Po , the detector can reach a relatively high detection efficiency of $33.3 \pm 1.6\%$ and for ^{218}Po the efficiency is $29.1 \pm 1.4\%$ (see Figure 7.4).

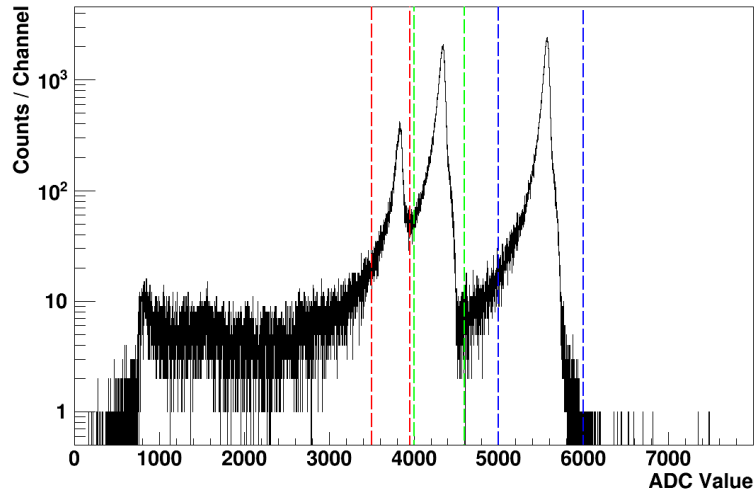


Figure 7.3: The energy spectrum with peaks of ^{210}Po , ^{218}Po , and ^{214}Po from left to right during the detector detection efficiency calibration run.

Comparing with the previous two efficiency calibrations summarised in Table 7.1, one can conclude that the detector performed stably over the years even after the High Voltage (HV) module upgrades in 2015.

Year of calibration	Efficiency for ^{214}Po	Efficiency for ^{218}Po
2012	$31.6 \pm 1.6\%$	$27.1 \pm 1.4\%$
2014	$31.5 \pm 1.3\%$	$28.14 \pm 1.1\%$
2016	$32.2 \pm 1.6\%$	$29.7 \pm 1.4\%$

Table 7.1: The results of the last three spike method detection efficiency calibrations.

Practically, the ^{218}Po efficiency can also be affected by peak proximity from the residential ^{210}Po , which is a decay product of ^{210}Pb in the ^{222}Rn decay chain. ^{210}Pb has a relatively long half-life of 22.2 years, which means it will deposit and accumulate on the PIN photodiode during the measurement. In normal low-activity measurements, the ^{210}Po peak is much higher than the ^{218}Po peak, as shown in Figure 7.5. Although the detector resolution is excellent, an overlap between the ^{210}Po and ^{218}Po tail is inevitable. Thus ^{214}Po is the ideal candidate as the measure of radon.

The assumption of the neutralisation effect caused by the extra impurities in the

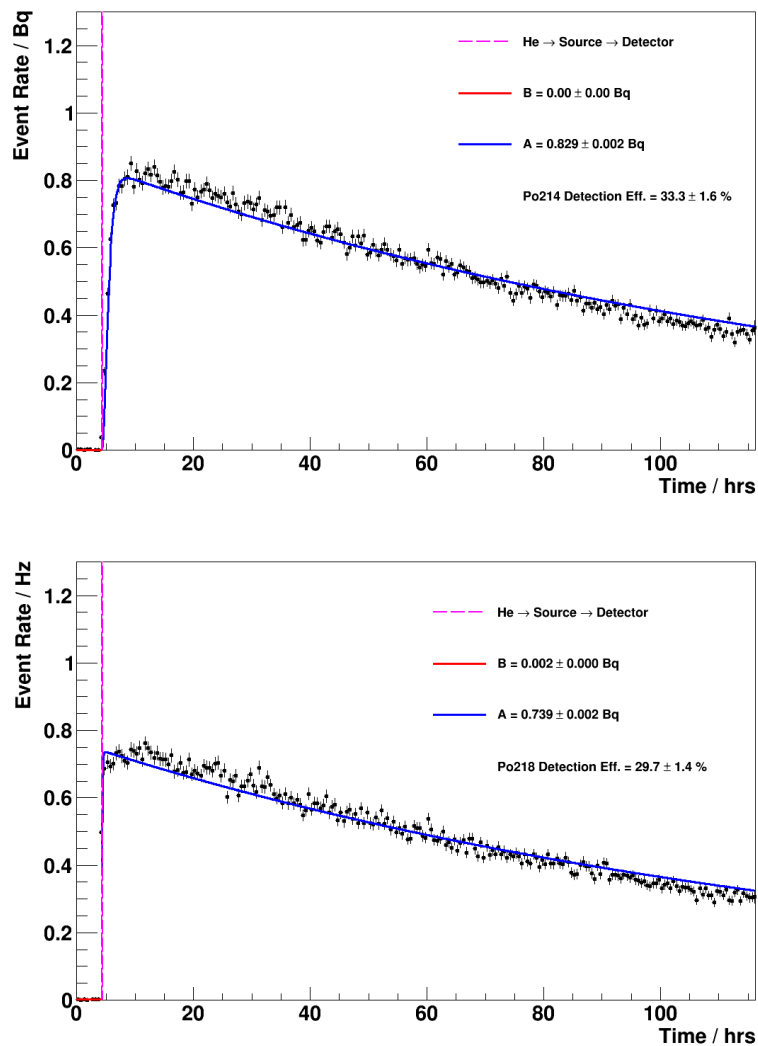


Figure 7.4: Event rates of ^{214}Po on the top and ^{218}Po on the bottom during the spike method detector detection efficiency calibration run, where blue curves show fit with the fixed half-life of ^{222}Rn . A is the detected activity of source introduced in to the detector. B is the intrinsic background level of the detector.

nitrogen environment, mainly trace nitrogen oxides, was confirmed by comparing the calibration results using helium and nitrogen. Lower efficiencies were indeed observed: $28.1 \pm 1.1 \%$ and $22.3 \pm 0.8 \%$ for ^{214}Po and ^{218}Po respectively [43].

The flowthrough method was generally used as a cross-check with the spike calibration. Nitrogen was chosen as the carrier gas flushing through the source and

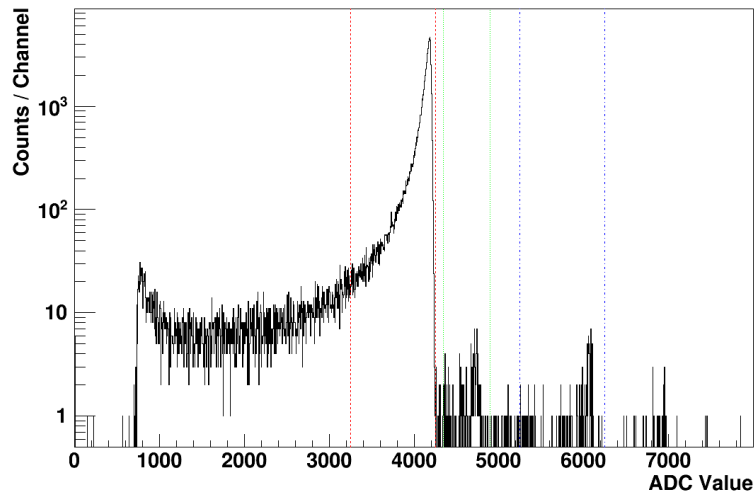


Figure 7.5: The energy spectrum with peaks of ^{210}Po , ^{218}Po , and ^{214}Po from left to right during a typical low-activity measurement.

the detector at 4.2 litres per minute (lpm). Taking the ratio of the observed radon level by the detector over the calculated equilibrium radon activity supplied by the source at this flowrate, the detection efficiency can be determined as $26.3 \pm 1.8\%$ and $22.2 \pm 1.6\%$ for ^{214}Po and ^{218}Po respectively. These agree well with the spike method results.

A summary of the most recent calibration results is shown in Table 7.2.

Calibration Method	Carrier Gas	Efficiency for ^{214}Po	Efficiency for ^{218}Po
Spike	Helium	$33.3 \pm 1.6\%$	$29.1 \pm 1.4\%$
Spike	Nitrogen	$28.1 \pm 1.1\%$	$22.3 \pm 0.9\%$
Flowthrough	Nitrogen	$26.3 \pm 1.8\%$	$22.2 \pm 1.6\%$

Table 7.2: Electrostatic radon detector detection efficiency calibration results using different carrier gases.

7.1.3 Detector Background and Anti-Radon Bag

A sensitive detector requires not only a high detection efficiency but also a low background counting rate. Prior to the measurement of the sample, to accurately estimate the background from the activity of observed radon and to make

sure the background is low and stable, a background measurement was carried out. Long-term background measurements were performed occasionally to ascertain the intrinsic activity of the detector. During these kinds of measurements, the detector works in a pure helium environment to maximise the detection efficiency. In a typical detector background measurement (as shown in Figure 7.6), the counting rate of ^{214}Po was found to be 6.5 ± 1.0 counts per day (cpd), translating into 0.23 ± 0.03 mBq or 3.23 ± 0.49 mBq/m³ given that the detector chamber is 70 L in volume.

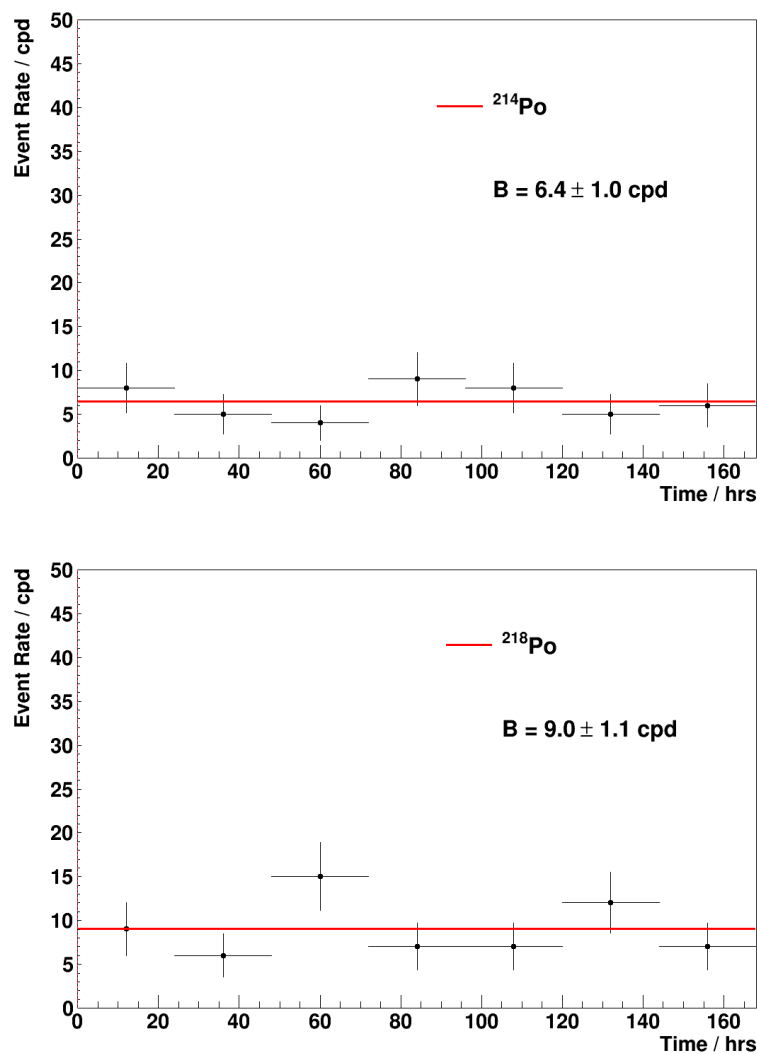


Figure 7.6: Event rates of ^{214}Po on the top and ^{218}Po on the bottom during a typical detector background run.

In a detector calibration run, high activity from the introduced source results in

spectral peaks arising from ^{214}Po and ^{218}Po decay. In a background measurement run, the spectra resemble those of low-activity sample measurements.

^{210}Po activity remains close to constant on account of the long half-life of its grandparent ^{210}Pb deposited on the PIN photodiode, except after a calibration run when its activity will increase. This property of ^{210}Po provides a very convenient way to check the stability of the detector, the power supply, and the DAQ. The detector and the whole system along with it were transported back to a clean room at UCL from the Mullard Space Science Laboratory (MSSL) in October 2017. After re-assembling, the results from the commissioning run showed that the detector was stable, and the background was low, as expected. A series of long background measurements were taken to verify the background level of the detector, and over a long period, the observed ^{214}Po counting rate remains 5 - 6 cpd, which is low and stable compared to the background level before the move. However, substantially higher background rates of ~ 15 cpd were observed later, which will reduce the sensitivity by a factor of $\sqrt{3}$.

One assumption for this increase was the higher radon diffusion effect caused by the abnormal environmental radon level in the cleanroom. The SBR used to coat the seal between the chamber and the lid of the detector as a radon barrier could have aged over seven years. A commercial electrostatic radon detector, RAD7, was then installed to monitor the environmental radon level. Some consistency between the detector background and the environmental radon level was found by comparing the detector data and the RAD7 data during the same period. In addition, the radon level in the room was too high for a clean room (see Figure 7.7).

Two strategies exist for the attempted mitigation of the high background. The first strategy is to re-coating the seals with SBR, which will inevitably require the opening and re-sealing of the detector, during which process fragile electronic components run the risk of being damaged. In addition, despite being opened in a cleanroom, proper cleaning of the detector chamber post-unsealing to ensure

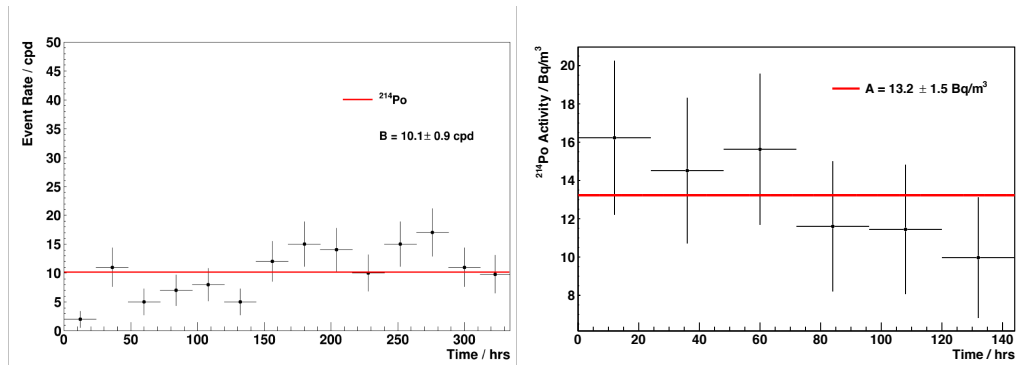


Figure 7.7: Electrostatic detector background (left). B is the background rate in the detector. The environmental radon level measured by RAD7 during the last six days (right). A is the detected radon progeny (^{214}Po) activity in RAD7.

it is sufficiently uncontaminated is a non-trivial process.

The second solution was chosen as it is both reliable and more convenient than the first one, which is to provide the detector with a clean working environment by housing it in a compatibly sized anti-radon bag where nitrogen is continuously flushed through to suppress radon (as shown in Figure 7.8).

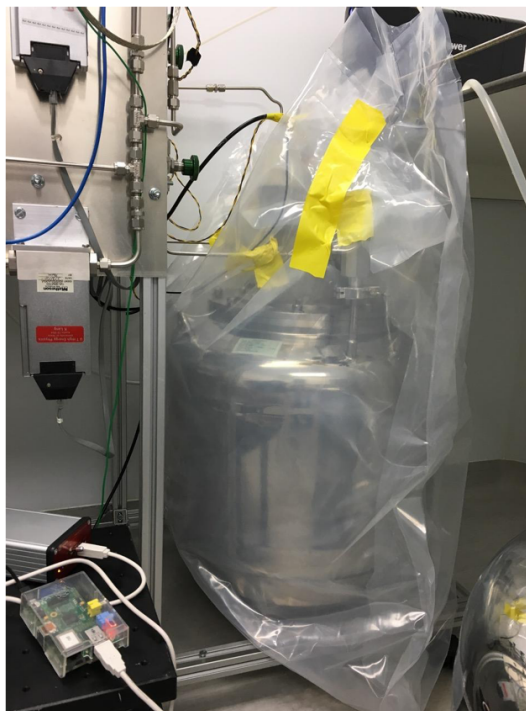


Figure 7.8: Radon detector housed in the anti-radon bag.

Double-layer transparent polythene foil was heat-sealed to build the anti-radon

bag housing the detector, and two gas feedthroughs were attached to the bag for the gas inlet and outlet. Flushing at 1.0 lpm, which is the lowest flowrate the ball-flowmetre can achieve, an improvement on the intrinsic background level was observed, with the ^{214}Po rate dropping down to 2.5 - 3.0 mBq/m³ as usual.

7.1.4 Analysis Method

For offline analysis, each signal is stored via the NEMbox DAQ system as an event in which the date and time together with 1000 sample points of the digitised pulse are recorded in text format. 1000 events fill up a text file, and then the files are analysed using ROOT.

The data file is processed in two steps. Firstly, a peak-finding algorithm determines the number of peaks in each pulse, their amplitude, and the time — this process is called signal identification. With amplitude and time information, all the pulses can be classified into four different types of events: signal events, BiPo events, pile-up events, and noise events (as shown in Figure 7.9).

A signal event contains only one peak, and therefore processing proceeds straight to the next step. The BiPo event refers to the double peak as a result of the electron from ^{214}Bi decay and the alpha from ^{214}Po decay, with an average gap of 164.3 μs , which is the half-life of ^{214}Po . To be detected and identified as a BiPo event, the two particles must deposit energy on the PIN photodiode within the 15 μs pre-trigger window. Thus, this kind of event is rarely observed and contributes only ~1% of the ^{214}Po events. The pile-up event is also a rare, double-peak event, which contains two alpha peaks. It is distinguishable from the BiPo event as the magnitude of the electron peak in a BiPo event is visibly smaller than the alpha peak due to the decay energy. Pile-up events are typically only observed during calibrations when the activity inside the detector chamber is high. The last type of event is the electronic noise which consists of many peaks of similar magnitude in a single pulse. Their amplitude is usually low; however, very occasionally, one can be large enough to mimic a signal event.

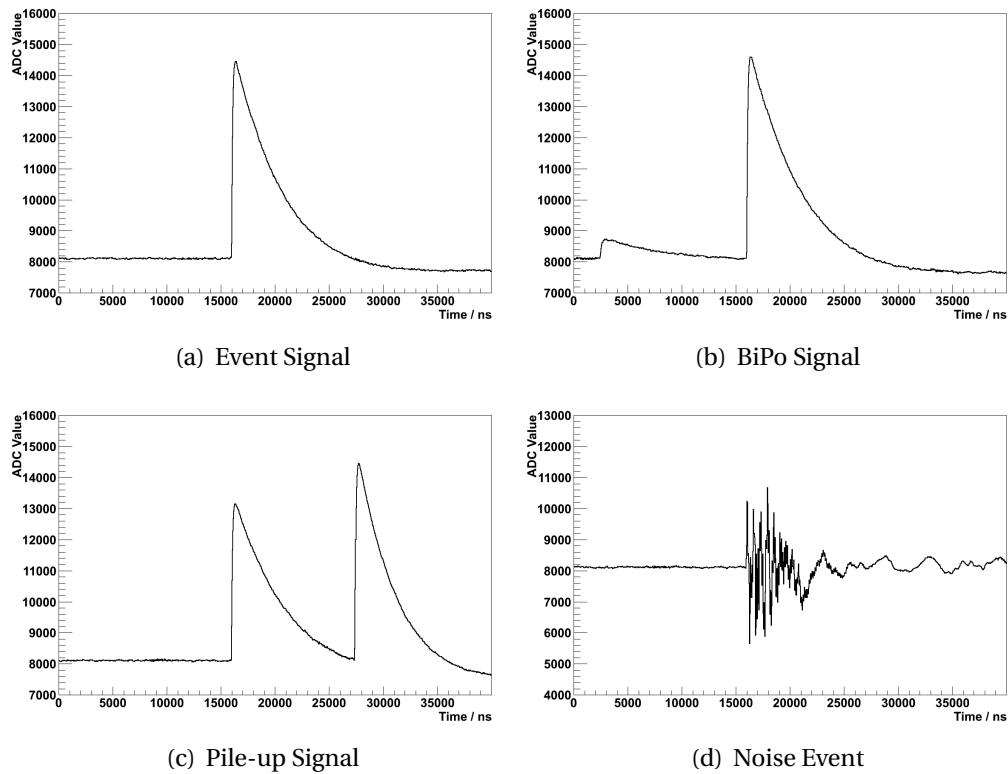


Figure 7.9: Examples of the four types of events identified at the filtering stage.

Signal events are then processed to the next, pulse-fitting step. For optimisation of extracting the best value of amplitude, each signal pulse is fitted with a function defined as the ideal form of a signal coming from the PIN photodiode and processed through the pre-amplifier. This signal form can be determined via the observation of the output from the pre-amplifier while injecting light from an LED into the photodiode. The study shows that the signal pulse can be described as a sharp linear rise followed by an exponential decay (see Figure 7.10 as an example).

7.2 Sensitivity of the Radon Detector

The sensitivity of the radon detector system is quantified by the Minimum Detectable Activity (MDA), as defined in 'Radiation Detection and Measurement' by

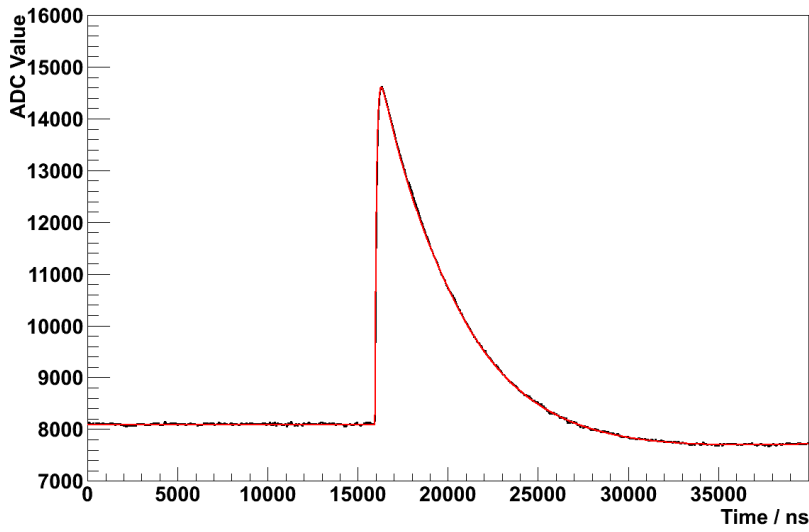


Figure 7.10: A typical signal event (black) with the pulse fitting function (red) superimposed [31].

G. F. Knoll [111]. In this thesis, the MDA represents the detector sensitivity at 90% C.L. unless specifically stated. This definition is based on the binary decision of whether the output of the detector is signal with background or background only. There is the possibility of a false-positive event where a background event is indicated as a signal, in addition to the possibility of a false-negative event where a signal is misidentified as a background only. A critical number of counts, n_c , is predefined, where if more counts than this number are observed, one can claim that the signal presents. n_c is found for the expected number of background events, B , and the measurement confidence level, CL . The probability of false positive is less than $1 - CL$. If B follows the Poisson distribution, to meet the above criterion, n_c is increased until the following inequality is satisfied:

$$P_B(n \geq n_c) = \sum_{n=n_c}^{\infty} Pois(n; B) = 1 - \sum_{n=0}^{n_c-1} e^{-B} \frac{B^n}{n!} \leq 1 - CL \quad (7.1)$$

When n_c has been set high enough to reduce the false-positive probability to $1 - CL$, the probability for false negatives can be used to calculate the minimum expected number of signal events, S , that satisfies the MDA requirement. Thus,

S must be increased to satisfy the following inequality:

$$P_{S+B}(n < n_c) = \sum_{n=0}^{n_c-1} \text{Pois}(n; S+B) = \sum_{n=0}^{n_c-1} e^{-(S+B)} \frac{(S+B)^n}{n!} \leq 1 - \text{CL} \quad (7.2)$$

In Figure 7.11, the black curve is the Poisson-distributed background expectation, from which n_c has been set so that the black-shaded area corresponding to the false-positive equals $1 - \text{CL}$. The red line represents the distribution for the minimum signal on the same background, where S has been set such that the red-shaded area also corresponding to the false-negative equals to $1 - \text{CL}$. The minimum signal can be converted into an activity which is referred to as the MDA.

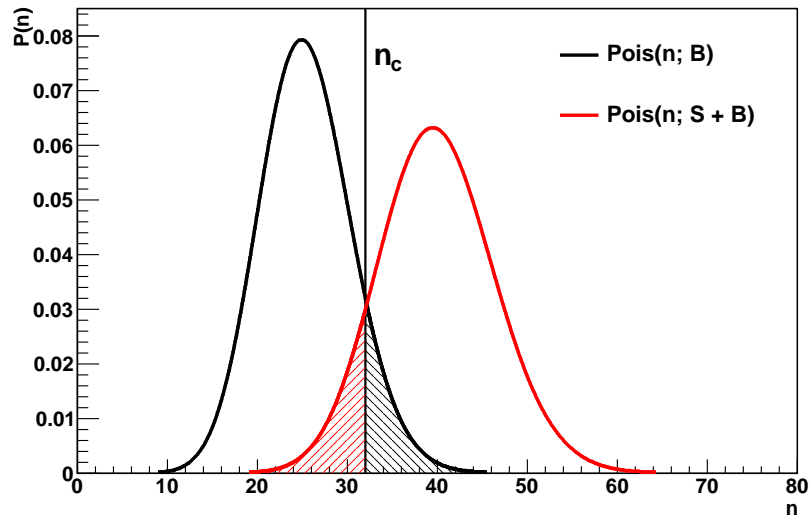


Figure 7.11: Probability distributions for two Poisson distributed variables. n_c has been increased until the false-positive result corresponding to the black-shaded area has sufficiently low probability. S has then been increased until the red-shaded area corresponding to the false-negative result which also has area $1 - \text{CL}$.

7.2.1 Normal Approximation

As it is difficult to work with the Poisson distributions analytically, simplification is applied based on the normal approximation for a sufficiently large sample size,

λ .

$$Pois(\lambda) \approx Norm(\mu = \lambda, \sigma = \sqrt{\lambda}) \quad (7.3)$$

The continuity correction $n_c \rightarrow n_c - \frac{1}{2}$ can be used to further improve the approximation. Therefore Equation 7.1, where $\lambda = B$, becomes:

$$P_B(n \geq n_c) \approx \int_{n_c - \frac{1}{2}}^{\infty} \frac{1}{\sqrt{2\pi B}} e^{-\frac{(x-B)^2}{2B}} dx = \frac{1}{2} - \frac{1}{\sqrt{\pi}} \int_0^{\frac{n_c - \frac{1}{2} - B}{\sqrt{2B}}} e^{-t^2} dt \quad (7.4)$$

Introduce the error function defined as:

$$\text{erf}(x) = \frac{2}{\sqrt{\pi}} \int_0^x e^{-t^2} dt \quad (7.5)$$

Using this definition and Equation 7.1 and 7.4 it can be seen that:

$$P_B(n \geq n_c) \approx \frac{1}{2} \left(1 - \text{erf} \left(\frac{n_c - \frac{1}{2} - B}{\sqrt{2B}} \right) \right) \leq 1 - \text{CL} \quad (7.6)$$

The equivalent procedure can be applied to Equation 7.2 to give:

$$P(n < n_c) \approx \frac{1}{2} \left(1 + \text{erf} \left(\frac{n_c - \frac{1}{2} - (S+B)}{\sqrt{2(S+B)}} \right) \right) \leq 1 - \text{CL} \quad (7.7)$$

As the MDA definition provides the smallest possible value of S for a given B , n_c can be eliminated. Combining Equation 7.6 and 7.7, it can be found that:

$$S - \sqrt{2BE} \geq \sqrt{2(S+B)E} \quad (7.8)$$

where E is a positive number defined as:

$$E = \text{erf}^{-1}(2\text{CL} - 1) \quad (7.9)$$

The unphysical solution where $S \leq 0$ should be excluded, so that:

$$S \geq 2E(E + \sqrt{2B}) \quad (7.10)$$

When the inequality is equal, S can reach its minimum value. The MDA can be calculated from the minimum number of signal events that are detectable, S_0 , given by:

$$S_0 = 2E(E + \sqrt{2B}) \quad (7.11)$$

7.2.2 Detector Sensitivity

To estimate the detector sensitivity, we assume that a sample with activity A_S is introduced into a detector of which intrinsic background activity is A_D . The number of radon atoms in the detector, N , is given as:

$$\frac{dN}{dt} = -\lambda N + A_D \quad (7.12)$$

Therefore:

$$\frac{d}{dt}(e^{\lambda t} N) = e^{\lambda t} \left(\frac{dN}{dt} + \lambda N \right) = e^{\lambda t} A_D \quad (7.13)$$

and:

$$e^{\lambda t} N = \int e^{\lambda t} A_D dt = \frac{A_D}{\lambda} e^{\lambda t} + C \quad (7.14)$$

The detector is flushed to remove residual radon before a measurement, so $N = A_S/\lambda$ at $t=0$. Thus, C can be determined as $C = A_S/\lambda - A_D/\lambda$, and the number of the radon atom can be calculated as:

$$N = \frac{A_D}{\lambda} (1 - \lambda e^{\lambda t}) + \frac{A_S}{\lambda} e^{-\lambda t} \quad (7.15)$$

Equation 7.15 contains two terms: the background and the signal. When the measurement time is much longer than the half-lives of intermediate isotopes in the decay chain of ^{222}Rn to ^{214}Po , one can make the approximation that the signal events are all from ^{222}Rn since ^{214}Po can reach equilibrium after 4.5 hours, see Figure 7.12.

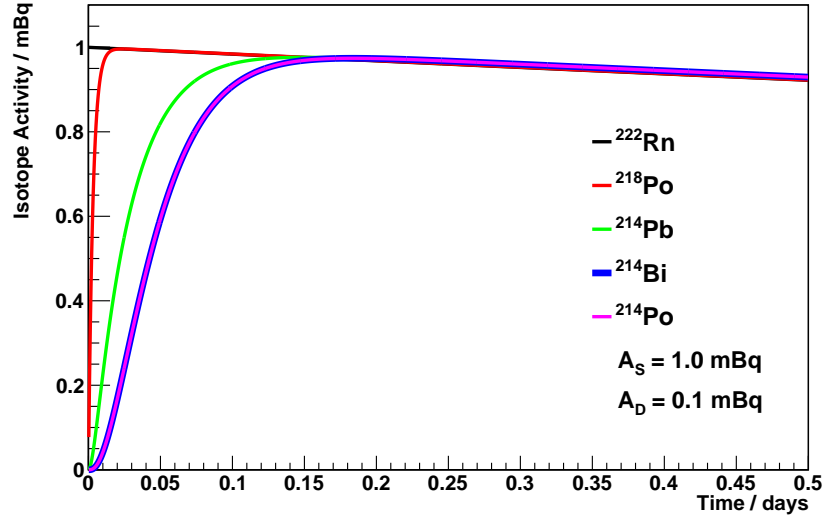


Figure 7.12: Activities of different isotopes in the ^{222}Rn decay chain with respect to time after introducing 1 mBq of ^{222}Rn into a detector with 0.1 mBq background [31].

For a zero background detector with the detection efficiency, ϵ , when sample activity is A_S introduced, the number of signal events after a time T , is given as:

$$S = \epsilon \int_0^T \lambda N dt = \epsilon \int_0^T A_S e^{-\lambda t} dt = \epsilon \frac{A_S}{\lambda} (1 - e^{-\lambda T}) \quad (7.16)$$

Similarly, if the detector has an intrinsic background of A_D , when no sample is introduced, the pure background is measured as:

$$B = \epsilon \int_0^T \lambda N dt = \epsilon \int_0^T A_D (1 - e^{-\lambda t}) dt = \epsilon A_D T - \epsilon \frac{A_D}{\lambda} (1 - e^{-\lambda T}) \quad (7.17)$$

From this the MDA for the detector can be calculated by first finding B using Equation 7.17, then S_0 which is the minimum number of signal events detectable

for a given confidence level. So S_0 can be converted into the MDA using Equation 7.16. The detector MDA as a function of the measurement time T is shown in Figure 7.13.

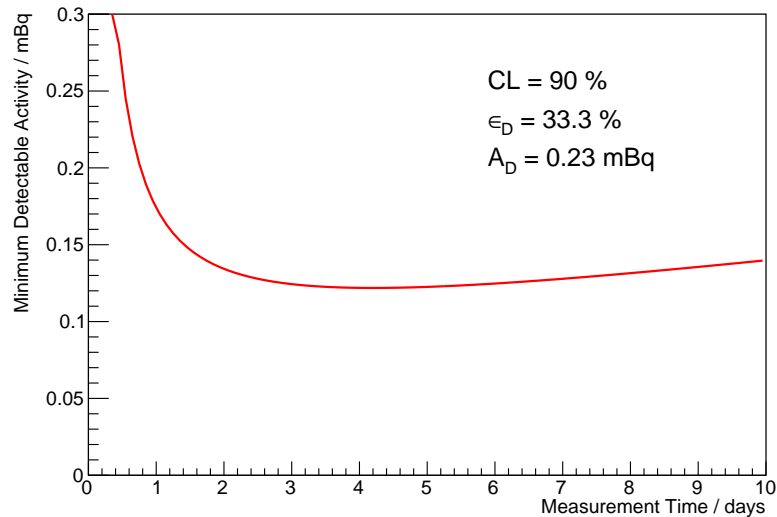


Figure 7.13: MDA for the electrostatic detector as a function of the measurement time.

7.3 Emanation Chambers

In the radon emanation measurements for small samples, the emanation chambers were used to house the sample while isolating it from the environment. Two emanation chambers were built in the US with stainless steel to ensure radiopurity, and then assembled and tested for the intrinsic radon emanation level at UCL.

The emanation chambers (as seen in Figure 7.14) are both 152.4 mm in length and 146 mm in diameter, and each a resulting ~ 2.6 litres in volume. Two flanges are sealed to the tubular body on both sides, using copper gaskets. The chamber was cleaned, assembled, and leak tested at UCL. A typical leak test contains two stages. In the first stage, helium was used for flushing the chamber to remove residual air once the chamber was assembled, and during flushing, a helium sniffer (GasCheck Tesla Helium Leak Detector, Ion Science) was used to check all the connections to ensure that there were no significant leaks above 10^{-6} cc/s. The

leak checking was then repeated after the chamber was sealed under 0.5 bar overpressure, to ensure there were no leaks above 10^{-6} cc/s. The chamber was transported to MSSL for further cleaning, reassembling, and connecting to the gas line, together with the radon detector for further tests (as shown in the schematic Figure 7.15). Leak tests are also carried out each time when it is opened and re-sealed for a sample insertion. .

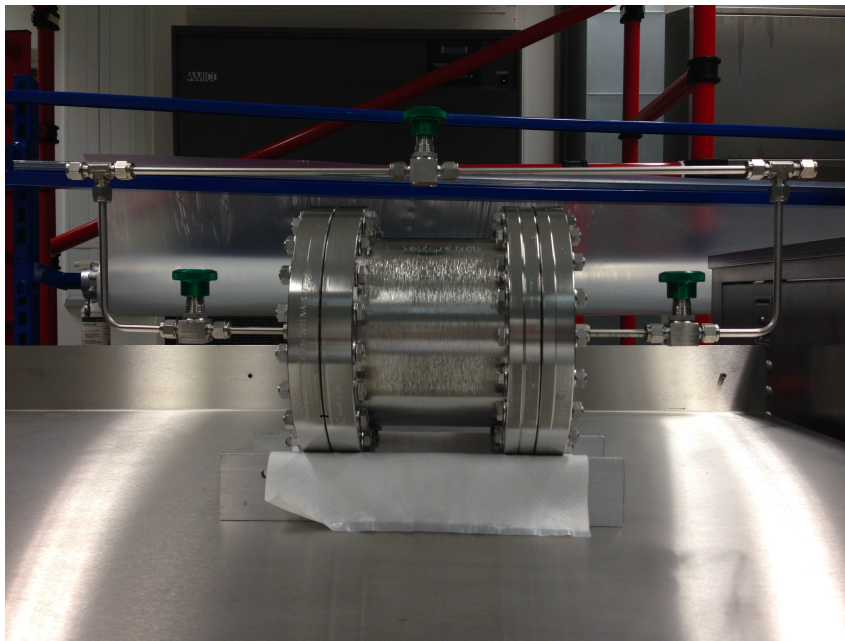


Figure 7.14: The second emanation chamber fully assembled at MSSL.

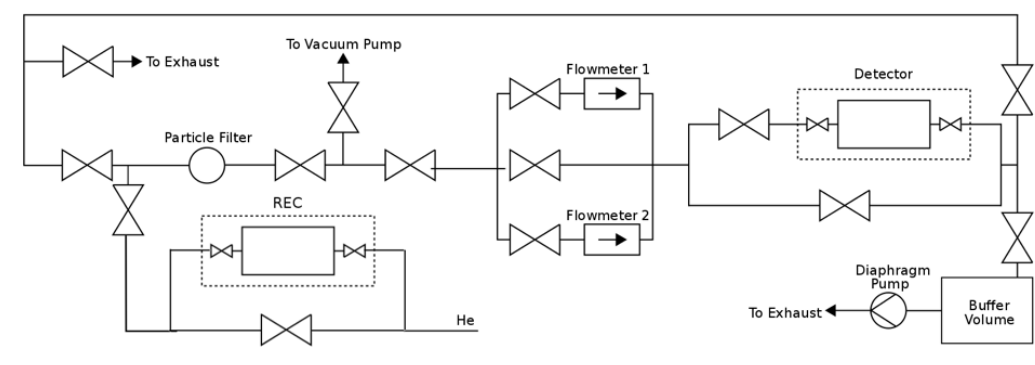


Figure 7.15: Schematic of the gas line with the emanation chamber connected [43].

7.3.1 Background of the Emanation Chambers

The intrinsic background of the chamber determines the sensitivity, and as such it is very important to monitor it by performing the chamber self radon emanation measurement. To prepare for this measurement, the chamber was flushed with 100 volumes of helium to remove residual gases, while the helium sniffer was used to carry out a leak test again to ensure for airtightness. After flushing, the chamber was then sealed under atmospheric pressure and left to emanate over 30 days, equivalent to 8 radon half-lives, to reach equilibrium before being transferred into the detector. Meanwhile, prior to the transfer, the detector was cleaned by flushing 10 volumes of clean helium and sealed under atmospheric pressure, followed by a 5-day detector background measurements to not only to ensure the background was low and stable but also to provide an accurate background level during the period. The gas sample was then transferred into the detector for a measurement, carried by 25 litres of helium, resulting in an increase of the operational pressure of the detector from 1 bar to 1.36 bar. The first emanation chamber which was assembled in 2014 has an intrinsic background of $< 90 \mu\text{Bq}$ at 90% CL [112]. The measurement result of the second chamber over 8 days is shown in Figure 7.16. Data of the detected signal events each day is plotted with an error bar. The red vertical dashed line indicating the time of sample transfer divides the plots into two parts. The data on the left, referring to the detector background measurement, is fitted with a polynomial to extract the detector background B . For the right side, corresponding to the chamber measurement, an exponential fit based on the radon decay with a half-life of 3.8235 days was applied. The radon activity, A , can be determined by extrapolating back to the moment of transfer. The intrinsic background of the chamber can be calculated by:

$$A_C = \frac{A \text{ (cpd)} \times 1000 \text{ (mBq)}}{\epsilon_D \times (1 - e^{-N_V}) \times (1 - e^{-\lambda t}) \times 86400 \text{ (secs/day)}} \quad (7.18)$$

where A_C is the radon activity in mBq, ϵ_D is the detection efficiency of the de-

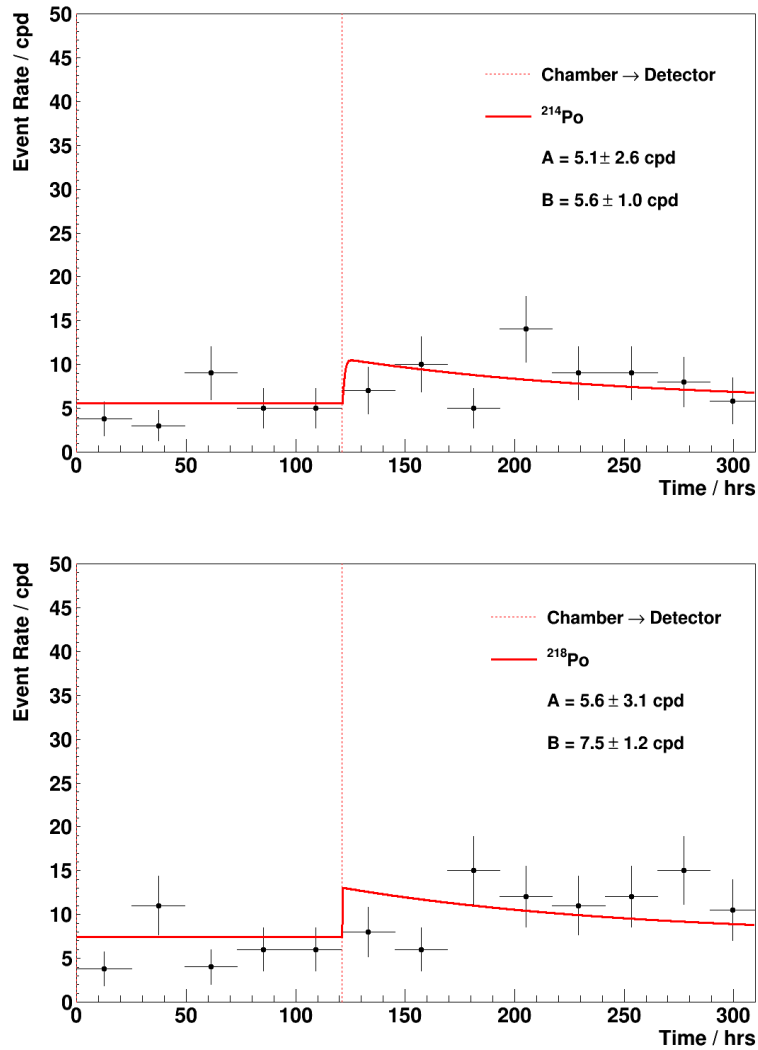


Figure 7.16: Event rates of ^{214}Po (on the top) and ^{218}Po (on the bottom) of the back-ground measurement of the second chamber.

tector, $1 - e^{-\lambda t}$ is the correction of initial activity levels from equilibrium, and N_v is the number of volumes of the chamber flushed into the detector, thus $1 - e^{-N_v}$ gives correction on transfer efficiency.

Hence, the sensitivity (90% CL) of the second emanation chamber is:

$$\begin{aligned} A_{214\text{Po}} &< 170 \mu\text{Bq} \\ A_{218\text{Po}} &< 223 \mu\text{Bq} \end{aligned} \tag{7.19}$$

7.3.2 Radon Harboursing Hypothesis

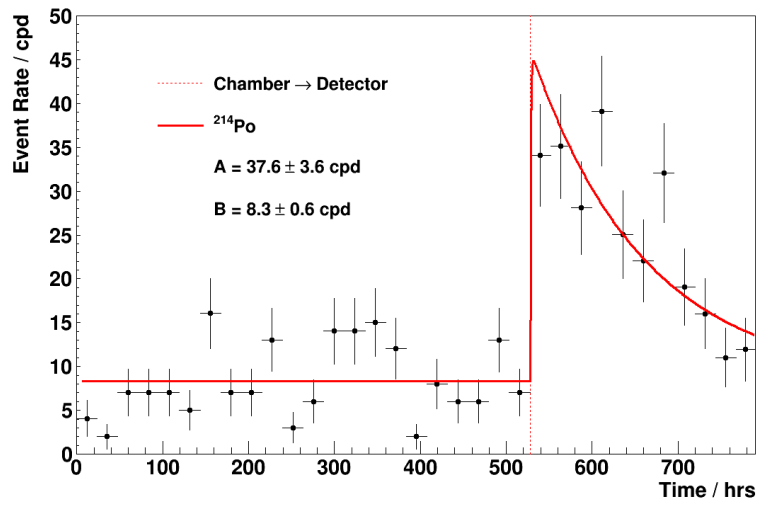
For most sample radon emanation measurements, at least a second measurement is carried out to confirm the result. In some of the cases, higher activities were observed in the first radon emanation measurement compared to further repeat measurements. One possible explanation is the radon harboursing hypothesis. Environmental radon can diffuse into the materials, and this residual radon can not be removed by flushing, and will eventually contribute to the final result.

One good demonstration of this hypothesis is the radon emanation measurement of Room Temperature Vulcanizing Silicone (RTV), which was one of the proposed materials for the SuperNEMO detector. The sample was cleaned and placed into an emanation chamber. The chamber was then flushed with 200 volumes of clean helium to remove residual radon and sealed.

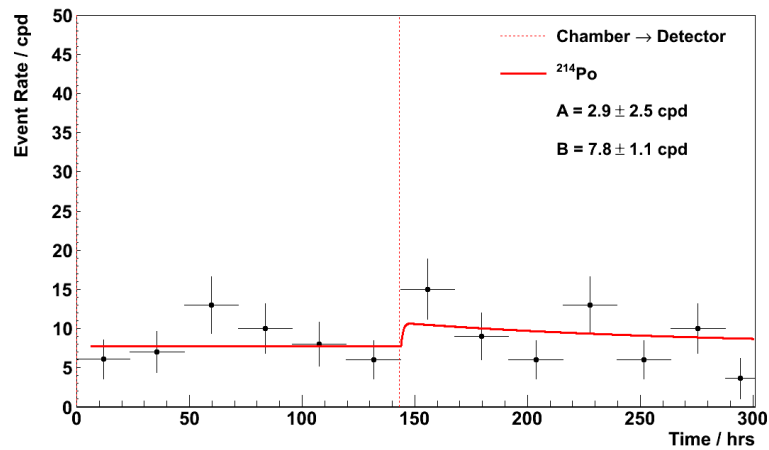
After 30 days' emanation, the gas sample was transferred into the detector for the first measurement by purging with 25 litres of clean radon-free helium. After the transfer, the chamber was kept closed, flushed again, and sealed to prepare for a second measurement. After a further 16-day emanation (total time in the chamber), the gas sample was transferred into the detector. The result was found that the first measurement was surprisingly much higher than the second one. As such, a third transfer was carried out. This time, the material was kept inside the chamber for over 80 days, and the emanation since flushing after the second transfer was 20 days. The results from the three measurements are close the second one, as shown in Figure 7.17.

7.4 Radon Concentration Line

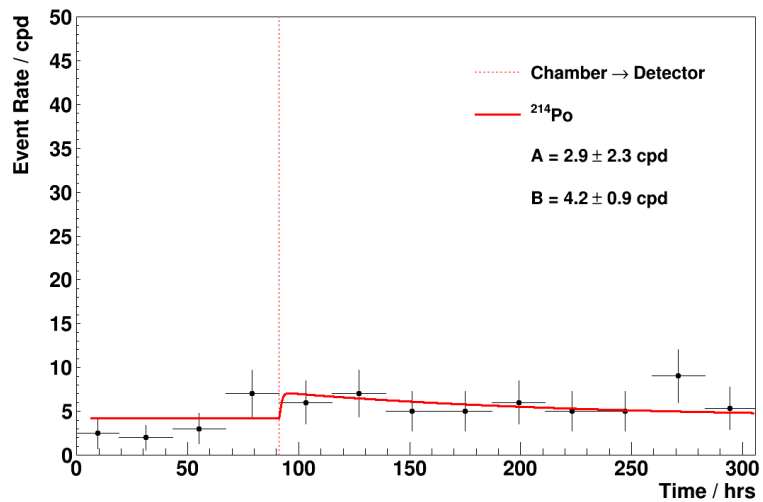
The sensitivity of the electrostatic radon detector at UCL is one of the best in the world. However, it is still not enough to measure the SuperNEMO target radon background level $150 \mu\text{Bq}/\text{m}^3$. The detector is 70 litres in volume and cannot



(a) Black Mumba Measurement 1



(b) Black Mumba Measurement 2



(c) Black Mumba Measurement 3

Figure 7.17: Event rates of ^{214}Po during the first, second, and third measurement of RTV sample shown in (a), (b), and (c) respectively.

be operated with too much overpressure, and is thus almost impossible to improve the sensitivity by increasing the gas sample volume purged into the detector. However, there is still another possibility which is to increase the radon concentration level so that the total amount of radon can be detectable for the electrostatic detector.

A Radon Concentration Line (RnCL) has been developed and built at UCL, which can concentrate and store radon from large volumes of gas and then sends the sample to the electrostatic detector for measurements. The RnCL working in conjunction with the electrostatic radon detector can reach a sensitivity of as low as $5 \mu\text{Bq}/\text{m}^3$ [31]. The design of RnCL is based on previous work of MoREx at Heidelberg [113], but has been modified to be more portable. The real-life set-up of RnCL is shown in Figure 7.18.

7.4.1 Setup of the RnCL

The essential part of RnCL is a stainless steel trap containing 52.5 g of radio-pure activated carbon (from Carbo-Act international). In order to improve radon absorption efficiency of the activated carbon, an immersion cooler (the EK90 Immersion Cooler from Thermo Scientific, capable of cooling to a minimum temperature of -90°C) was used to cool the carbon trap to -50°C [43].

While flushing gas through the system, radon will be captured in the trap, and this is called the trapping stage. After the trapping stage, the trap will be sealed and warmed to room temperature, then heated to over 220°C to release radon in preparation for the transfer of the radon sample into the detector. The volume of the trap is 0.5 litres in volume, thus in a typical run, 25 litres of flushing gas is assumed to be enough to transfer all the released radon into the detector.

To avoid any particles entering the electrostatic detector, a series of Swagelok stainless steel filters are installed before and after the trap on the gas line. The setup of RnCL is shown in Figure 7.18.

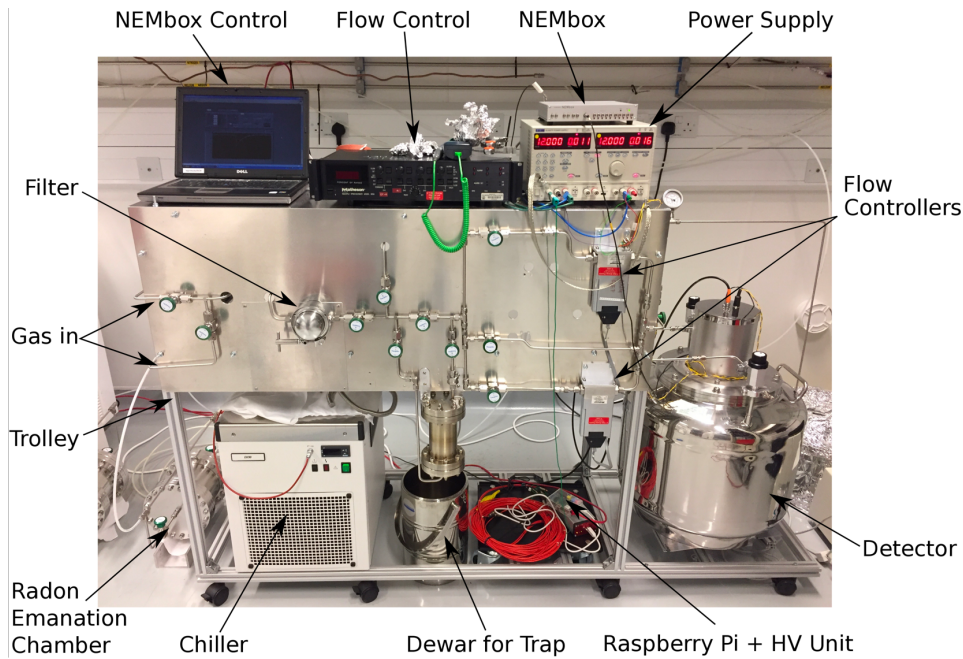


Figure 7.18: The setup of Radon Concentration Line in real-life [43].

7.4.2 Calibration

The trapping and transfer efficiency of RnCL must be determined so that the system can offer meaningful measurement results. The RnCL can be calibrated with the flowthrough method. The radon emanation of the SuperNEMO quarter tracker modules (also called C-Section due to its C shape) are also measured using the RnCL via the flowthrough method, thus calibrating the RnCL under same conditions of the C-Section measurement can provide reliable results. The calibration procedure is described as follows.

1. First, flush the RnCL and detector with nitrogen to remove the residual radon and seal the detector afterwards. Attach the calibration radon source (same source as detector calibration) to the RnCL and then continuously flush nitrogen at 3 lpm through the source to the exhaust over at least 4 hours. This flushing procedure lasts for at least 4 hours, with the aim of clearing the residual radon and to wait for the residual polonium to decay away.
2. After 4 hours of zeroing the source, increase the flowrate to 7 lpm and divert the gas flow through the detector to the exhaust over ~ 24 hours, to monitor

the activity through the detector. The activity should remain stable after several hours' radon build-up until the end of the 24 hours' flushing. The flowrate of 7 lpm is selected in particular because it is the flowrate used in the real C section measurement, and it is also the highest achievable flowrate due to leaks on the C section at this stage. The event rates of this stage during the most recent calibration measurement is shown in the first ~ 24 hours (between the red dashed lines) of Figure 7.20 and Figure 7.21.

3. After 24 hours' flushing, start the trapping stage by diverting the gas to flow from the source through the cold trap (typically < -50 °C in the central part of the trap) and detector to exhaust. The trap is cooled down via immersion in isopropanol inside a Dewar, and cooled by the refrigerator cooler (EK90 Immersion Cooler from Thermo Scientific). The event rates of the trapping stage is shown in Figure 7.20 and Figure 7.21 (between the green dashed lines).

4. After 24 hours, seal the trap and source to stop trapping, and then remove the source. Also, stop cooling the trap and wait until the trap is warmed back to room temperature.

5. Start heating the trap to release radon and in the meantime flush the detector with 700 litres of helium to remove residual radon and replace the nitrogen environment inside the detector. As mentioned previously (see Section 7.1), the detector has a better detection efficiency working under a helium atmosphere.

6. When the trap is heated to over 200 °C, transfer the gas sample from the trap into the detector for measurement. The event rates after transfer is shown in Figure 7.21 (after the pink dashed line).

The specific activity at the output of the source can be calculated by Equation 7.20.

$$a_S^{eq} = \frac{A_S}{f_S/\lambda} = \frac{1.32 \pm 0.05 \text{ kBq}}{55.7 \pm 2.7 \text{ m}^3} = 23.7 \pm 1.5 \text{ Bq/m}^3 \quad (7.20)$$

where A_S is the activity of the source and f_S is the flowrate through the source,

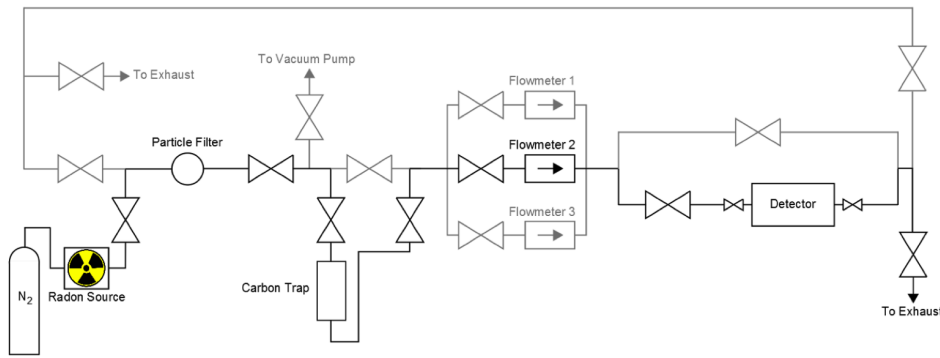


Figure 7.19: Schematic diagram of the setup during a flowthrough calibration of the RnCL.

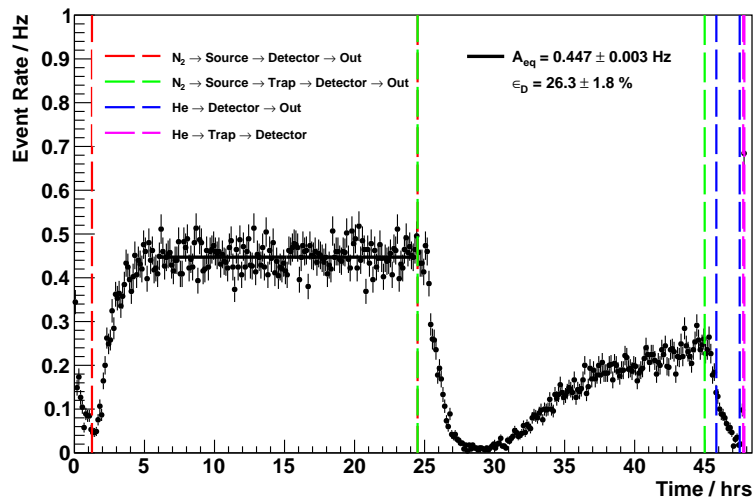


Figure 7.20: Typical ^{214}Po rates measured in the detector during the trapping stage of the RnCL flowthrough calibration measurement, with nitrogen as the carrier gas and a trap temperature of $-50\text{ }^{\circ}\text{C}$.

here is 7 lpm. The equilibrium activity in the detector A_D^{eq} during first ~ 24 hours can be determined by by Equation 7.21

$$A_D^{eq} = \frac{A_S}{1 + f_S/\lambda V_D} = 1.7 \pm 0.1 \text{ Bq/m}^3 \quad (7.21)$$

where V_D is the detector volume 70 L. The measured event rate inside the detector at equilibrium was $0.447 \pm 0.003 \text{ Hz}$, translating into the detector efficiency of $26.3 \pm 1.8\%$.

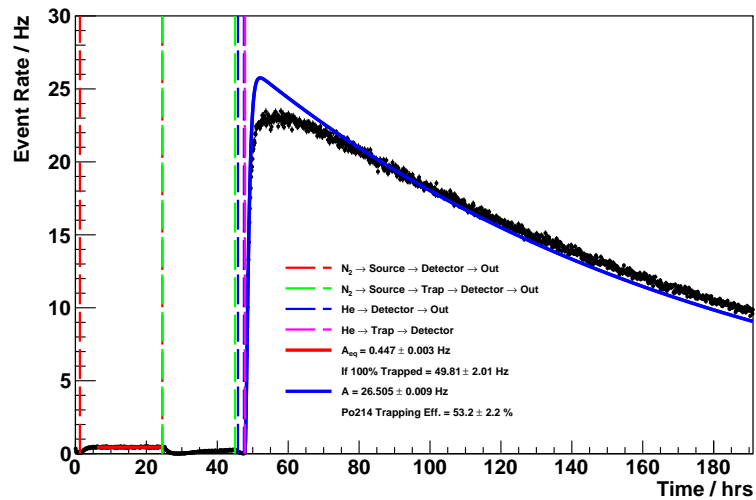


Figure 7.21: Typical ^{214}Po rates measured in the detector during the trapping and transfer stage of the RnCL flowthrough calibration measurement, with nitrogen flushing at 7 lpm.

The activity in the trap during the calibration is shown in Figure 7.21 and the calibration result is shown in Figure 7.22 and Figure 7.23.

It can be seen that the trapping efficiency decreases over time. There is a hypothesis for this loss of trapping efficiency that the activated charcoal becomes saturated with radon over time so that the radon is released into the detector and then detected. By keeping the trap in low temperature, the charcoal can adsorb more radon and hence takes longer to become saturated.

7.4.3 Sensitivity of RnCL

The MDA of the electrostatic detector was defined in Section 7.2.2. The RnCL is able to improve upon this MDA in terms of Bq/m^3 by allowing the measurement of the concentrated radon sample from a large volume of gas with the electrostatic detector. The MDA improves as a function of the volume of gas [31], as shown in Figure 7.24.

A significant improvement can be seen, and sensitivities as low as $5 \mu\text{Bq}/\text{m}^3$ can be achieved. The volume of gas required to improve the MDA increases expo-

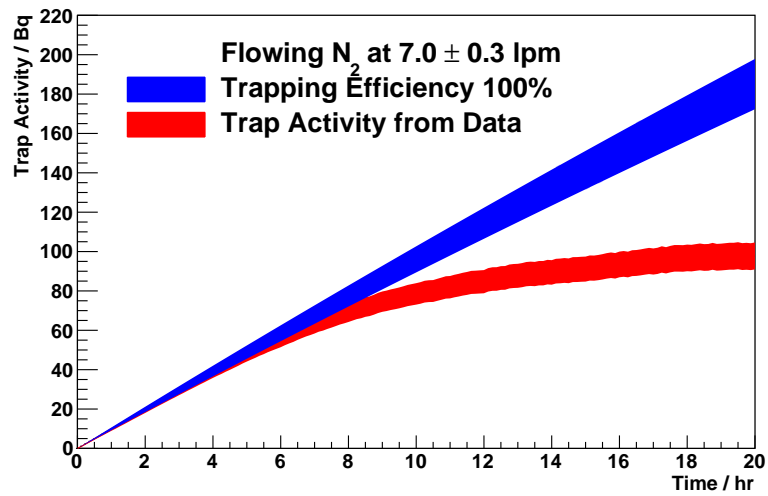


Figure 7.22: Radon activity inside the carbon trap during the flowthrough calibration of RnCL. The activity is calculated by measuring the trap output (red) and in the ideal trapping efficiency case (blue).

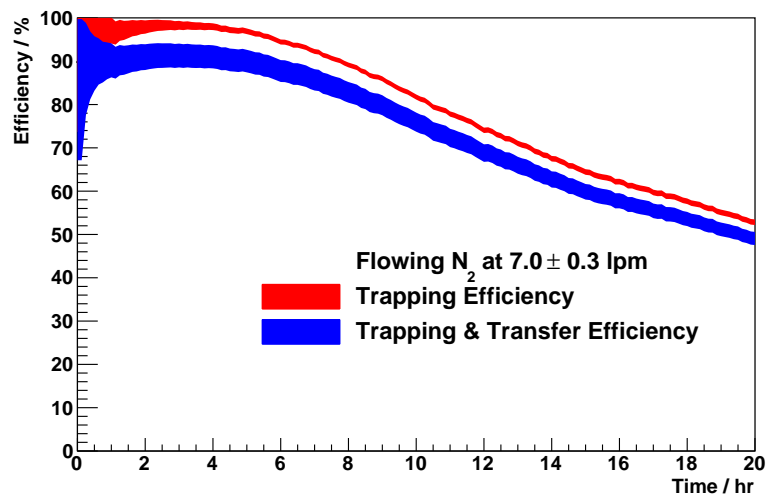


Figure 7.23: Ratio of the two lines in Figure 7.22 giving the trapping efficiency (red) and the trapping and transfer efficiency (blue).

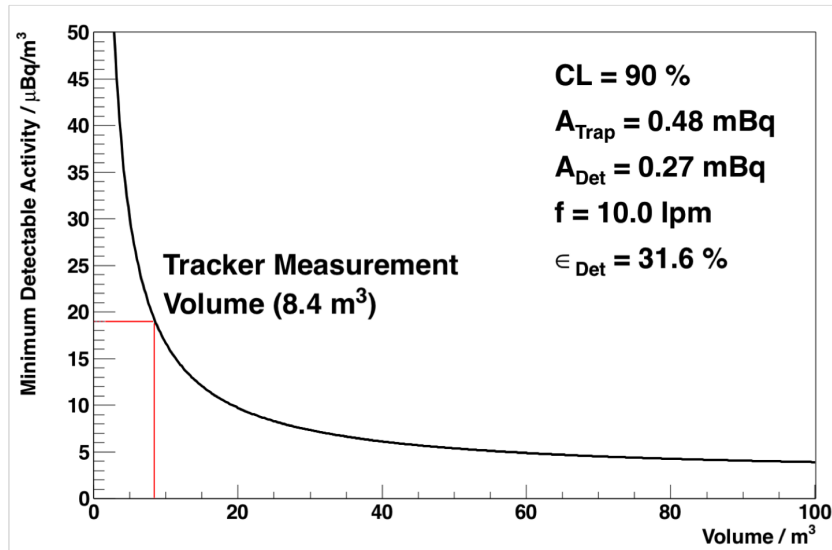


Figure 7.24: The Sensitivity (MDA) of RnCL for the C-Section measurement, as a function of the sample gas volume [43].

nentially. For a typical C-Section measurement, where 8.4 m^3 of gas is sampled, a sensitivity of $< 20 \mu\text{Bq}/\text{m}^3$ can be reached, which is more than enough to meet the SuperNEMO radon target.

7.5 J-trap

The J-trap is a gas purification system developed and built at Centre de Physique des Particules de Marseille (CPPM) by J. Busto [114], which is designed to supply carrier gas with ultra-low and stable radon contamination by removing radon in the gas. Since all commercial gases contain relatively high and variable amounts of radon, the J-trap can remove the greatest sources of systematic uncertainties in measurement.

The J-trap is estimated to suppress the radon by a factor of 20 for nitrogen and 2×10^{10} for helium [114]. The trap consists of two freezers operating at $-50 \text{ }^\circ\text{C}$ and $-80 \text{ }^\circ\text{C}$ containing 3 and 1 stainless steel cartridge respectively, each housing 0.5 kg of active charcoal. The schematic of the J-trap is shown in Figure 7.25.

When the carrier gas flows through the system, the active charcoal can adsorb

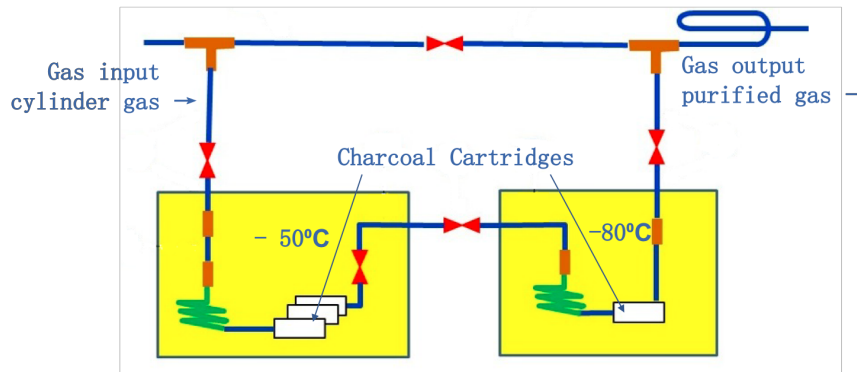


Figure 7.25: The schematic of the J-trap developed at CPPM [114].

radon. The low temperature improves the radon trapping efficiency of the charcoal as well as suppressing the radon emanation of the charcoal itself. The system does not require very radio-pure charcoal to work, thus reducing the cost of building it. The charcoal cartridges can be replaced when needed, which provide more portability. The J-trap was delivered to MSSL and installed in May 2014, then moved to UCL and reassembled in October 2017. The temperature was monitored regularly to ensure it remained stable.

The principle of measuring the radon suppression of the J-trap is similar to a C-Section measurement [115], as described in Section 8.3. The results of the radon contamination level of nitrogen after the J-trap are listed in Table 7.3 in comparison with cylinder nitrogen gas and cylinder helium.

There can be considerable variation of the radon activity among cylinders, and even within the same cylinder but different remaining activity [31]. With the J-trap, one of the most significant systematic uncertainties of the measurement involving a large volume of gas can be removed.

Gas	Source	Radon Level ($\mu\text{Bq}/\text{m}^3$)
He	Cylinder	70-100
N ₂	Cylinder	400-1000
N ₂	J-trap	20

Table 7.3: Measurements of cylinder helium and cylinder nitrogen and nitrogen from the J-trap [116].

Chapter 8

Radon Emanation Measurements

The radon detector and the RnCL have both demonstrated excellent performance and, when used in conjunction, the capability to reach and surpass the target radon sensitivity required for the SuperNEMO demonstrator. All the radon measurements are carried out for two main purposes: screening to select the cleanest possible material; and building up the background model based on measurements obtained from individual components. The RnCL allows the monitoring of radon emanation from quarter trackers during and after construction providing essential information on meeting the radiopurity requirement. The ability to measure a fully instrumented tracker volume is a key aim as radon emanation is area and geometry dependent. Some key measurements carried out using the radon detector alone, and in combination with the RnCL, are detailed here, including the measurement of three demonstrator quarter trackers, and radon emanation from the SuperNEMO gas system. The radon emanation measurement facility has also been used to measure samples for the LZ experiment.

8.1 Sample Measurements

Having established the background levels of the emanation chamber in Section 7.3, the chamber was then used for sample emanation tests of SuperNEMO and

LZ detector components and construction materials.

8.1.1 Feedthrough Emanation Measurements

Feedthroughs are used to deliver HV to the tracker cells and connect the anodes and cathodes of the cells to the tracker front-end electronics. Each feedthrough consists of a stainless steel frame, and CuBe pins held by the injected Duracon. There are 170 feedthroughs in the Demonstrator's tracker, and 28 of them were used as a sample to test the radon emanation level. The feedthrough sample was cleaned using Isopropyl alcohol (IPA) in the cleanroom laboratory and then inserted into the emanation chamber. The feedthroughs were arranged loosely to make sure all the surfaces can be easily flushed (see Figure 8.1). The flange was then sealed using a new copper ring and flushed with helium at 20 lpm for 15 minutes — 300 litres of helium in total, which is more than 100 volumes replacement of the 2.6-litre chamber. After the flush, the chamber was sealed under atmospheric pressure and left for emanation.

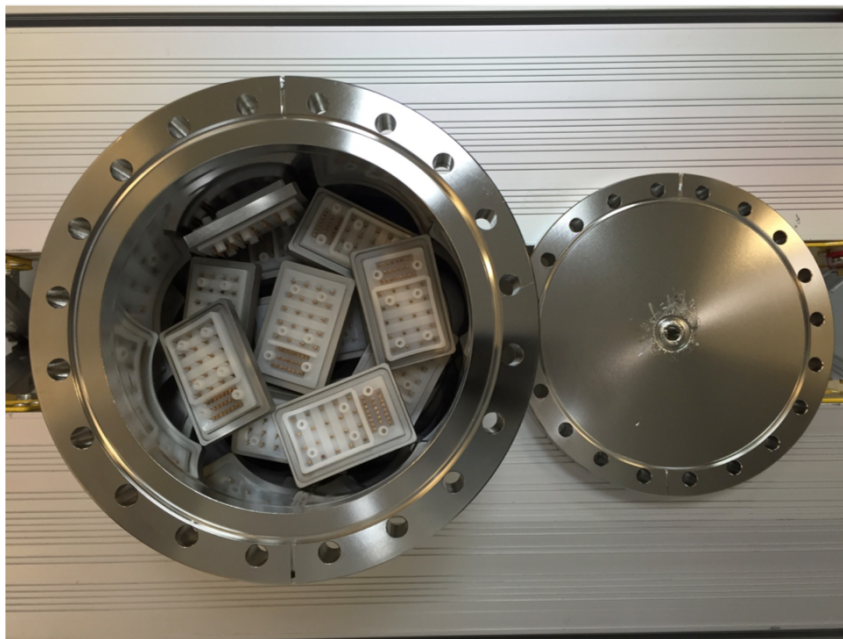


Figure 8.1: The insertion of feedthroughs into the emanation chamber.

Before starting the new background measurement, the detector was flushed with clean helium to remove any residual radon. Then, after 10 days, the gas inside the

chamber was flushed into the detector for measurement. Due to the low activity of emanated radon, a period of at least one week was required to gather statistics in order to determine the radon emanation level of the feedthrough as shown in Figure 8.2.

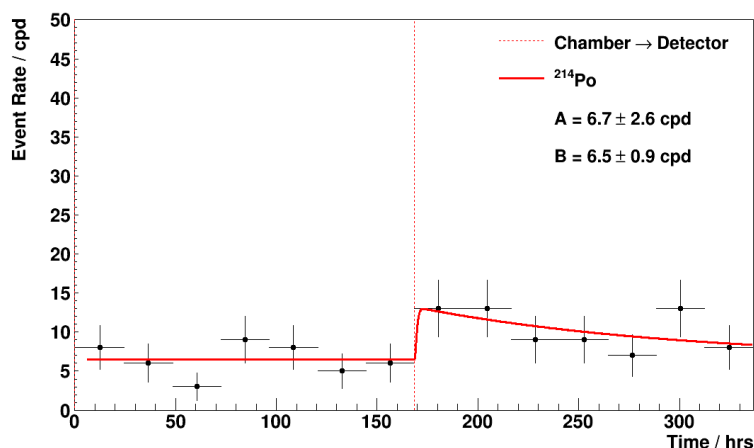


Figure 8.2: Event rates of ^{214}Po during the first feedthrough radon emanation measurement.

Due to the low activities of the samples, there are always fluctuations observed during a measurement. Also due to the radon harbouring effect as explained in Chapter 7.3.2, a second measurement should always be carried out. The emanation chamber is flushed again with 300 litres of helium and sealed under atmospheric pressure for emanation over another two weeks. Then a second transfer was made for the measurement following the similar procedures as the first measurement. The second measurement shows a result consistent with the first one (see Figure 8.3).

8.1.2 A List of Sample Emanation Measurements

To measure the radon activity of the SuperNEMO detector during the construction, all materials and detector components are screened for their radon emanation level. The UCL electrostatic radon detector has also been used for measuring samples for the LZ experiment. The final results of the sample measurements carried out by the author are listed in Table 8.1.

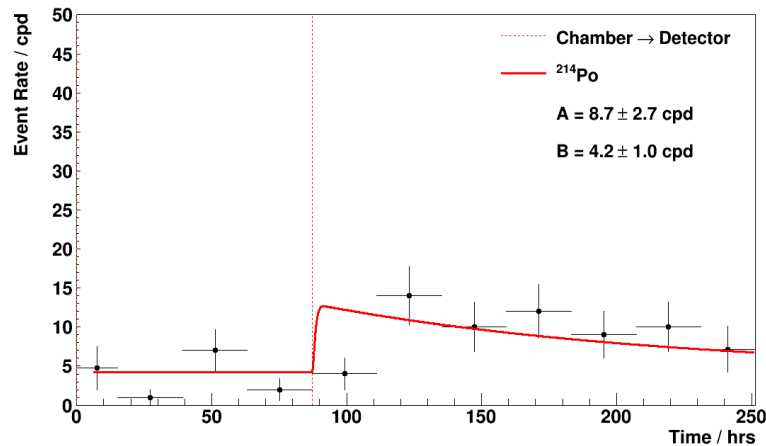


Figure 8.3: Event rates of ^{214}Po during the second feedthrough radon emanation measurement.

Experiment	Sample	Radon emanation
SuperNEMO	Feedthrough	0.18 ± 0.06 (mBq/kg)
SuperNEMO	Black Mumba (RTV strips)	0.10 ± 0.08 (mBq/kg)
SuperNEMO	Protective Mylar	0.75 ± 1.20 (mBq/m ³)
LZ	Delrin Disks	5.6 ± 1.8 (μBq /each)
LZ	O-rings	15.2 ± 1.4 (μBq /each)
LZ	PMT base	5.0 ± 0.9 (μBq /each)
LZ	resistors	17.9 ± 5.7 (μg)

Table 8.1: The results of radon emanation measurements from detector components and construction materials of SuperNEMO and the LZ experiment, all measured by the electrostatic detector.

8.2 Gas System Measurement

The tracker gas of SuperNEMO is made up of 95% helium, 1% argon and 4% ethanol. To obtain the accurate proportions, a dedicated gas supply system has been developed at UCL. It is compact and transportable such that it can be used both for the commissioning of the tracker and for running the experiment in its final configuration at LSM.

The biggest part of the gas system is a 50-litre cylinder bubbler made of stainless

steel for better radiopurity. As a carbon radon trap similar to the RnCL trap to filter the output from the gas system cannot be installed, as it would result in the removal of ethanol as well, the gas system is instead connected directly to the tracker. The volume of the gas system is relatively small, so that at the proposed flushing rate (1 - 2 m³/h), all ²²²Rn emanated from the gas system components or diffused into the gas will be flushed into the tracker volume within the half-life of ²²²Rn. Hence, it is strictly required that radon emanation from the gas system is < 0.2 mBq, corresponding to 10% of the total tracker radon budget 2 mBq.

In order to verify the radon emanation level of the Gas System — three different measurements, spike measurement, flowthrough measurement and the RnCL measurement — were carried out.

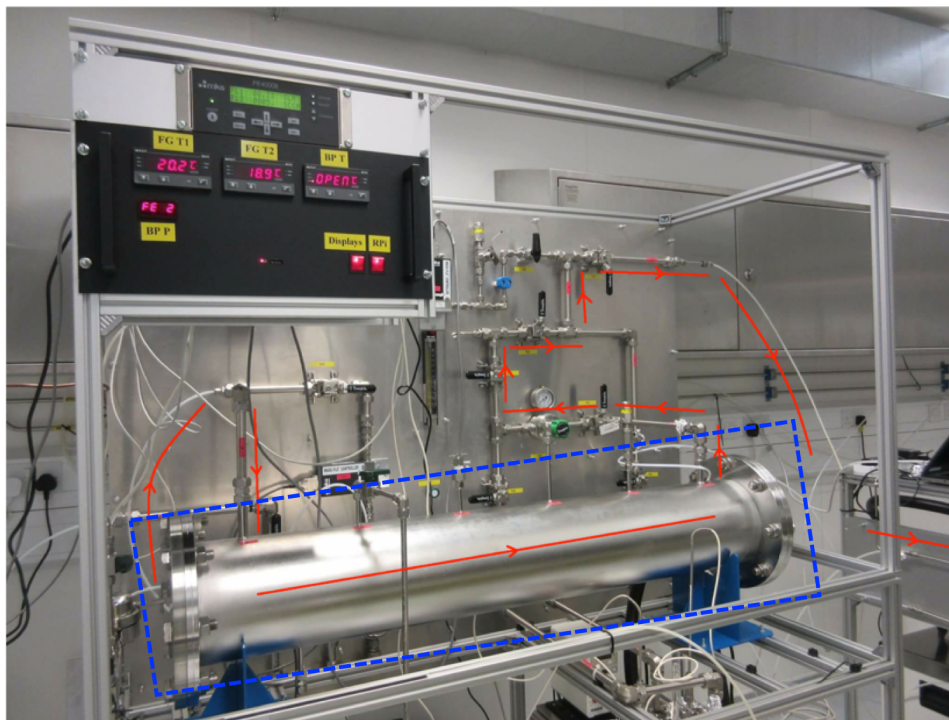


Figure 8.4: The gas system in real-life. The primary region for the radon emanation test is labelled in red [117], and the chamber in blue dashed box is the main bubbler.

8.2.1 Removing Ethanol

Ethanol can affect radon emanation. Ethanol can affect radon emanation. Ethanol can also be absorbed onto activated carbon, thus cause saturation in the

trap of the RnCL. As such, prior to carrying out the radon emanation measurement of the gas system, it is essential that all the ethanol inside the gas system is removed. The requirement of the residual ethanol level for carrying out the RnCL measurement is stringent, < 10 ppm, hence a residual gas analyser (RGA) was used to monitor the content of the output gas from the gas system. The main bubbler was drained and then flushed with nitrogen and helium to remove ethanol [43].

8.2.2 Flowthrough Measurement

The primary purpose of the flowthrough measurement is a quick check to ensure that there is no major emanation, but required sensitivity cannot be reached with this method. In this measurement, the gas system was set up to flow at 4.2 lpm rather than mimicking the real operation flowrate 14 lpm, taking advantage of the low flowrate to reach better sensitivity.

The procedures are as below:

1. Nitrogen was first used to flush the gas system for 24 hours prior to starting the measurement.
2. Use 500 litres of zero grade helium (10 volumes of the gas system) purging through the gas system to replace the nitrogen before starting the measurement for better detection efficiency.
3. Helium was flown from the gas system directly through the detector to exhaust at 4.2 lpm over 3 days.

Results of the flowthrough method measurement are shown in Figure 8.5.

No increase of radon level activity was observed in this measurement; thus, only a limit could be extracted. Since the measurement was carried out while flushing, the flow suppression factor has been taken into account.

$$A_D = \frac{A_0}{1 + \frac{\phi}{\lambda V}} + A_B \quad (8.1)$$

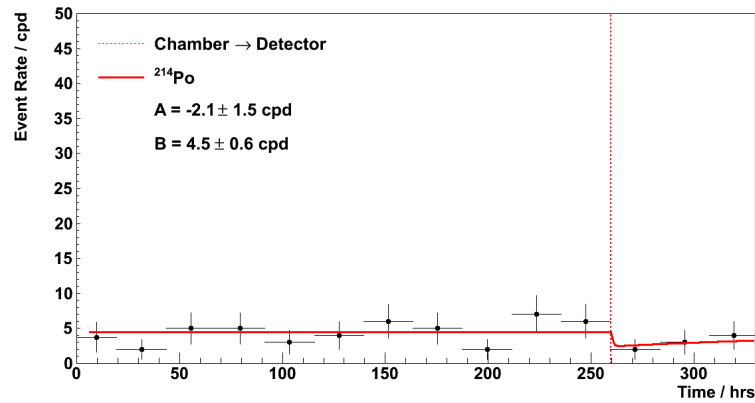


Figure 8.5: Event rates of ^{214}Po during the radon emanation measurement of the gas system using the flowthrough method [43].

where A_D is the observed activity;

A_0 is the true activity;

A_B is the background activity of the detector;

λ is the decay constant of ^{222}Rn ;

$1 + \frac{\phi}{\lambda V}$ is the suppression factor.

Taking the flowrate ϕ of 4.2 lpm and a volume, V , of 120 litres (the 50-litre gas system and the 70-litre radon detector), the suppression factor is calculated to be 280. From the uncertainty of the observed ^{214}Po activity, a limit can be placed at < 25 mBq at 90% CL. The quick flowthrough measurement confirmed that no significant radon emanation was observed.

8.2.3 Spike Measurement

The gas system can be seen as a big emanation chamber so that a spike measurement of the gas system is similar to the measurements of samples in the emanation chamber. However, it is slightly different from the sample emanation measurement due to the large volume of the bubbler. The detector is calibrated at 1.35 bar, and also it is not certified above 2 bar in terms of sealing. To avoid too much overpressure inside the detector, only 25 litres of gas will be transferred

into the detector as usual, which means the sample volume is smaller than the volume of the gas system.

Procedures of the measurement are as below:

1. Flush the gas system with helium from the J-trap at 20 lpm for 30 mins, totally purging 12 volumes of gas as replacements and then seal it under atmospheric pressure. In the meantime, a leaking test is carried out using a Helium sniffer. The gas system is then left for radon build-up over 17 days to reach equilibrium.
2. Flush the gas line and clear the radon detector to start the background measurement.
3. After the emanation period, check the detector background to ensure it is low and stable and flush the entire gas line except the gas system to remove residual radon in the gas line and then immediately transfer 25 litres of helium from the gas system into the radon detector.

Results from the spike measurement are shown as in Figure 8.6.

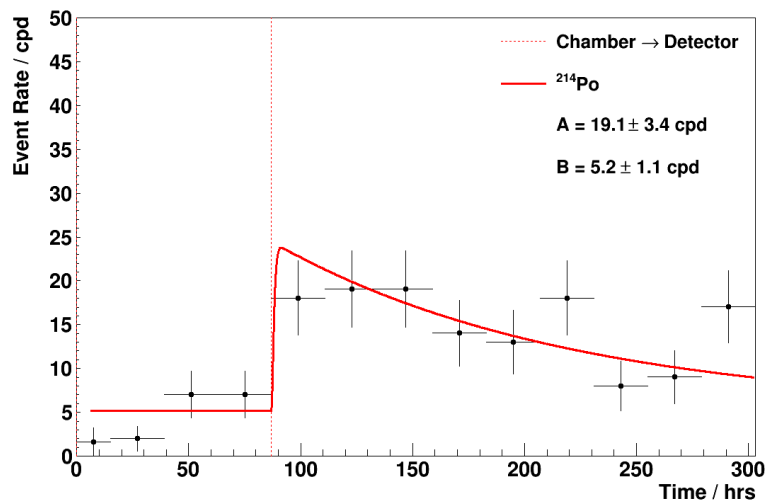


Figure 8.6: Event rates of ^{214}Po and ^{218}Po during the spike method radon emanation measurement of the gas system.

It should be noted that the transfer efficiency and the proportion of the volume should be counted in when extracting the activity. The transfer efficiency, ϵ_{trans} ,

was previously measured to be $70.1 \pm 0.9\%$ [118], and the proportion of the volume transferred is 50% (25 litres of helium transferred V_{trans} over the 50-litre gas system V_G). From the ^{214}Po result, the radon activity can be extracted as 1.97 ± 0.31 mBq using Equation 8.2.

$$A_C = \frac{A \text{ (cpd)} \times 1000 \text{ (mBq)}}{\epsilon_D \times (\epsilon_{trans} \times \frac{V_{trans}}{V_G}) \times (1 - e^{-\lambda t}) \times 86400 \text{ (secs/day)}} \quad (8.2)$$

8.2.4 RnCL Measurement

The RnCL measurement of the gas system is similar to the C-Section measurement as seen in Section 8.3, and the schematic of the measurement setup is shown in Figure 8.7. The volume of the gas system is dominated by the large bubbler, which has comparable size to the 70-litre electrostatic detector. The trapping transfer efficiency (Section 7.4.2) can be reliably used if the same flowrate, trap temperature and timing conditions are replicated. and the schematic of the measurement setup is shown in Figure 8.7.

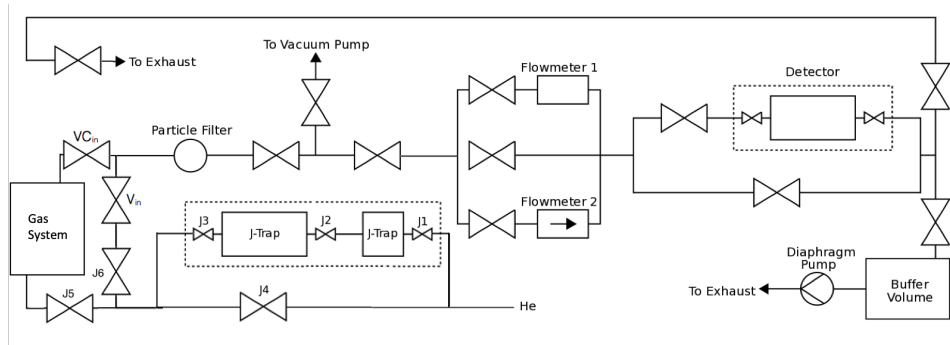


Figure 8.7: The system setup for the RnCL method measurement of the gas system.

The activity of radon introduced right after the transfer is [31]

$$A_D = \epsilon_{tr} A_C (1 - e^{-\lambda T_C}) + \frac{\epsilon_{tr} \epsilon_T (T_f) f a_{GS}^{eq}}{\lambda} (1 - e^{-\lambda T_C}) e^{-\lambda T_{trans}} \quad (8.3)$$

where:

λ is the decay constant of ^{222}Rn ;

ϵ_{tr} is the transfer efficiency;

ε_T is the trapping efficiency;

T_C is the time between clearing the trap and detector transfer (1705 min);

T_f is the time that the line is in contact with the trap (1200 min);

T_{trans} is the time between stopping trapping collection and detector transfer (240 min);

A_D is the radon activity in the electrostatic detector;

A_C is the radon activity of the carbon trap;

A_{GS}^{eq} is the equilibrium activity inside the gas system, given by [31]

$$a_{GS}^{eq} = \frac{A_{GS} + f_{in}a_G/\lambda}{V_{GS} + f_{in}/\lambda} \quad (8.4)$$

f_{in} is the input flowrate of gas;

A_{GS} is the radon activity of the gas system;

V_{GS} is the volume of the gas system.

The carrier gas radioactivity a_G are suppressed by the J-Trap. The measurement details of a_G were described in [119].

In the most recent calibration, the results of the transfer efficiency is 92.3% and the trapping transfer efficiency is 73.58%. The radon activity of the carbon trap, A_C , was measured as 0.48 ± 0.14 mBq (based on ^{214}Po results) with a carrier gas radioactivity a_G of 20.2 ± 12.5 $\mu\text{Bq}/\text{m}^3$ [119]. The radioactivity of the gas system can be calculated as 1.21 ± 0.38 mBq.

$$A_{GS} = \left(1 + \frac{f_{in}}{\lambda V_{GS}}\right) V_{GS} a_{GS}^{eq} - \frac{f_{in} a_G}{\lambda} \quad (8.5)$$

The result from the RnCL measurement and result from the spike method are consistent at 1.5 sigma level. Moreover, all results measured by three different methods have confirmed that the radon emanation of the gas system is < 2 mBq, considering the flow suppression factor 9.71 (at $1 \text{ m}^3/\text{h}$, see flow suppression), this number can be further reduced to < 0.2 mBq, which takes $\sim 10\%$ of the demonstrator radon budget.

8.3 Quarter Tracker (the C-Section) Measurements

The radon radiopurity budget for the SuperNEMO Demonstrator Tracker gas is $< 0.15 \text{ mBq/m}^3$. The sensitivity of the RnCL is calibrated at 8.4 m^3 is $< 20 \text{ } \mu\text{Bq}$ (see Section 7.4.3), which is more than enough to meet the requirement of measuring the radon emanation level of the SuperNEMO C-Section. All C-Sections were built and then sealed for radon emanation test at MSSL before they were eventually sent to LSM. Each tracker contains a stainless steel frame, 504 octagonal drift cells and 48 5-inch PMTs of which 32 are on the x-walls, and the other 16 are gamma vetos. Figure 8.8 shows the drift cell cassettes insertion completed for a C-Section.

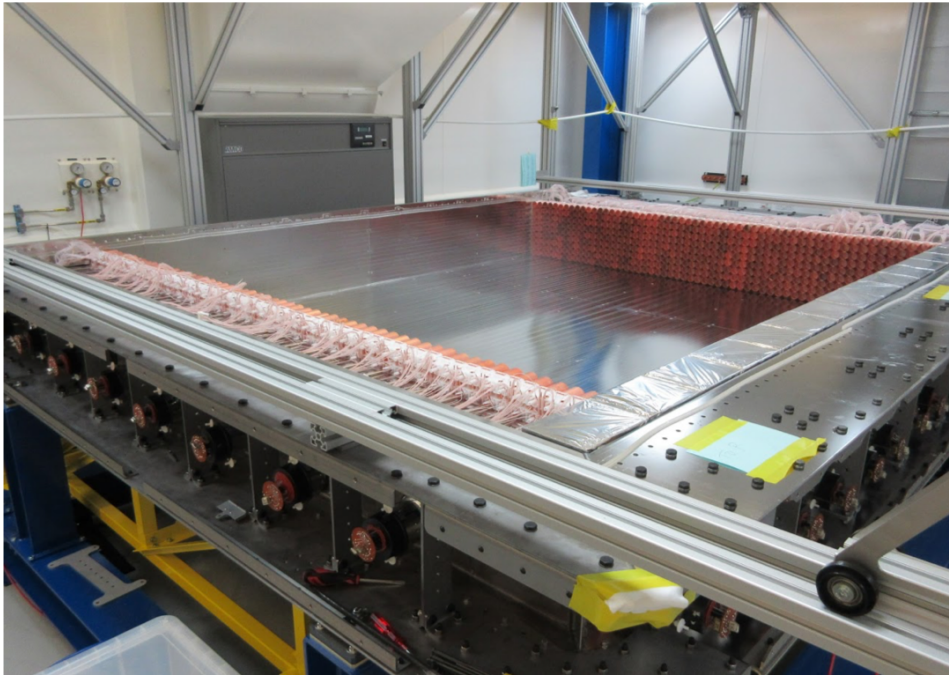


Figure 8.8: A C-Section (quarter tracker) under construction in the cleanroom lab at MSSL.

The main purpose of doing the radon emanation measurements of C-Sections is to obtain the activity from the tracker to build up the background model. The measured activity of the whole tracker is used in the simulation and analysis in Chapter 9. In addition, the first two C-Sections, C0 and C1, were not only measured after insertion was completed, but also tested before the cassette insertion

and halfway during the insertion, to help to monitor the radon level and to point out any positive radon contribution from components so that the contaminated parts can be removed. C-Sections were temporarily sealed with customised gas-sealing plates for the radon emanation test, tracker cell commissioning and transportation, prior to the final full demonstrator assembly when the all four C-Section were joined together with the source frame and calorimeter walls.

8.3.1 Measurement Starting Point

Ideally, the C-Section should be sealed perfectly and left for radon to emanate before the measurement; however, there were always small leaks at this stage. To prevent radon diffusion from the outside, a constant small overpressure supplied by a constant rate of gas flow must be kept inside the C-Section chamber. The C-Section was exposed to the cleanroom air during construction; thus, the components are expected to contain some radon as indicated by the radon harbouring hypothesis. As part of the preparation for the measurement, the sealed C-Section must be continuously flushed at 3 lpm using cylindered nitrogen over 18 days to remove residual radon [43]. In addition, the gas purging offered a 2 mbar overpressure inside the C-Section to prevent radon diffusion. Before starting a measurement, the flowrate was increased from 3 lpm to 14 lpm, which can maximise gas flow through the RnCL while keeping a secure overpressure inside the C-Section. Considering no external radon entering the C-Section, the number of radon atoms inside C-Section, N_T can be described by a model:

$$\frac{dN_T}{dt} = A_T + A_G - \lambda N_T - \frac{f_{in}N_T}{V_T} + \frac{f_{in}a_G}{\lambda} \quad (8.6)$$

where

A_T is the intrinsic activity of the C-Section;

A_G is the intrinsic activity of the gas supply line;

λ is the decay constant of ^{222}Rn ;

f_{in} is the flowrate of input gas;

V_T is the volume of a C-Section which is 3.8 m^3 ;

a_G is the activity of gas per unit volume from a specific cylinder or the J-trap, depending on the source of the gas.

So the activity of the output gas after the flushing time, t , can be modelled as:

$$A(t) = \frac{A_G + A_T + f_{in}a_G/\lambda}{\lambda'_T/\lambda} (1 - e^{-\lambda'_T t}) + A_0 e^{-\lambda'_T t} \quad (8.7)$$

where A_0 is the measured activity, and λ' is the modified decay constant defined by:

$$\lambda'_T = \lambda + \frac{f_{in}}{V_T} \quad (8.8)$$

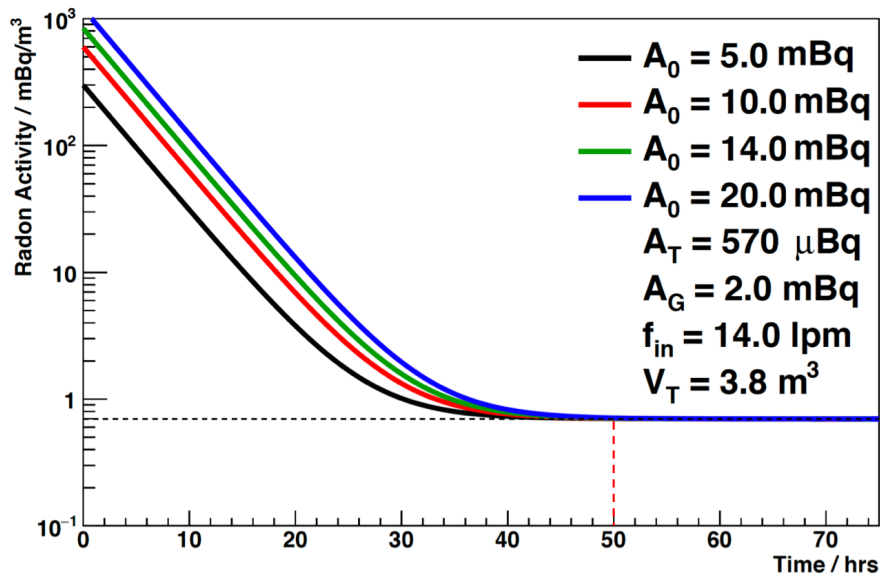


Figure 8.9: Activity inside the C-Section whilst flushing at 14 lpm prior to the radon measurement.

The measurement should only start after the output activity from C-Section reaches an equilibrium. Thus prior to the measurement, the C-Section was flushed for at least 50 hours. And during this stage, the output flowrate was only 7 lpm due to leaks.

8.3.2 Anti-radon Tent

It has been observed that the radon level of the cleanroom air fluctuated from 2 - 3 Bq/m³ to 10 - 20 Bq/m³, which is not low and stable enough and as such it is necessary to isolate the C-Section inside an anti-radon tent under a constant gas-flow to provide a cleaner environment. Double-layer transparent polyethene sheets were heat sealed together and then taped onto the ground to build the anti-radon tent. There are four flushing points installed at equal intervals on the tent and purged at 60 lpm to provide a small overpressure in the tent to prevent radon diffusion [120]. A RAD7 detector was installed to monitor the background level of radon in the anti-radon tent during the C-Section measurement. The result, ~ 0.1 Bq/m³, shows a reduction of 2 orders of magnitude, indicating the anti-radon tent successfully reduced radon from outside.



Figure 8.10: C2 in the annti-radon tent during the measurement.

8.3.3 Procedures of the C-Section Measurement

During the 50 hours' flushing RnCL was connected to the C-Section using 6 mm nylon pipe which has been tested of no positive radon emanation contribution.

A diaphragm pump was installed at the exhaust of the RnCL to promote gas purging because the low overpressure inside the C-Section chamber is not enough to maintain the required flowrate.

After 50 hours of flushing, the measurement can be started. Firstly, the RnCL trap was heated to release residual radon and flush radon away. Once the trap was cleaned, it was then sealed under atmospheric pressure, and the time zero of t_C is set. The trap was then cooled down to prepare for the radon trapping stage. When the temperature reached $-40\text{ }^\circ\text{C}$, start trapping by diverting nitrogen from the C-Section through the trap, at 7 lpm, and out to exhaust. This trapping stage lasts for 20 hours. After trapping, the trap was sealed again under atmospheric pressure, left to warm up to room temperature and then heated to release the absorbed radon. Upon reaching $220\text{ }^\circ\text{C}$, transfer radon from the trap into the electrostatic radon detector by purging 25 litres of helium through the trap.

8.3.4 C-Section Activity Extracting

As mentioned, there were leaks in the C-Section, through which radon can be lost. To extract the real intrinsic activity of the C-Section, it is necessary to model the observed radon. Prior to the start of the measurement, the C-Section is flushed at 14 lpm for 50 hrs to reach equilibrium. The activity inside the C-Section a_T^{eq} can be described by [31]:

$$a_T^{eq} = \frac{A_T + A_G + f_{in}a_G/\lambda}{V_T + f_{in}/\lambda} \quad (8.9)$$

such that activity A_T of the C-Section is

$$A_T = \left(1 + \frac{f_{in}}{\lambda V_T}\right) V_T a_T^{eq} - A_G - \frac{f_{in}a_G}{\lambda} \quad (8.10)$$

8.3.5 C-Section Measurement Results

During the radon emanation measurements of the first two C-Sections, C0 and C1, the Delrin caps used as the Geiger cell carriers showed an excess contribution of 4 ± 1 mBq for each C-Section. These components were replaced for the construction of the C2 and C3. The measurement result of the completed C2 is shown in Figure 8.11.

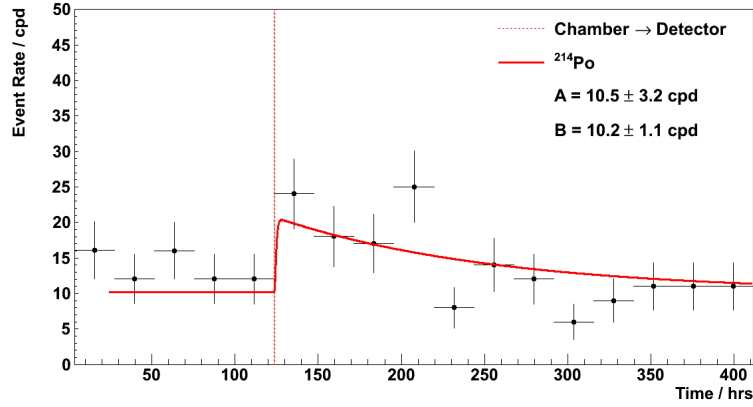


Figure 8.11: Results from the radon emanation measurements of the completed C2 [43].

The a_T^{eq} was calculated to be 0.057 ± 0.017 mBq based on the ^{214}Po result. And through Equation 8.10, the activity of of C2 was calculated:

$$A_T = 4.36 \pm 1.31 \text{ mBq} \quad (8.11)$$

which translates to

$$a_T = 1.15 \pm 0.34 \text{ mBq/m}^3 \quad (8.12)$$

The results of the first three C-Sections are summarised in Table 8.2. Assuming the radon emanation level of C3 is an average of the first three C-Sections, the activity of the entire SuperNEMO Demonstrator tracker is:

$$A_D = 41.3 \pm 4.7 \text{ mBq} \quad (8.13)$$

	activity (mBq)
C0	11.37 ± 1.44
C1	$15.26^{+2.50}_{-4.00}$
C2	4.36 ± 1.31

Table 8.2: Summary of C-Section measurement results.

translate to

$$a_D = 2.7 \pm 0.3 \text{ mBq} \quad (8.14)$$

This result shows that a radon activity of $0.28 \pm 0.07 \text{ mBq/m}^3$ can be achieved for the SuperNEMO Demonstrator by continuously flushing with clean tracker gas at $1 \text{ m}^3/\text{hr}$, providing a suppression factor of 9.71. This activity number is used to model the the SuperNEMO background in simulation and analysis described in Chapter 9.

Chapter 9

SuperNEMO Demonstrator

Sensitivity to Radon Background

Measurement

Neutrinoless double beta decay is a very rare process. As such, for experiments that involve the search for $0\nu 2\beta$ decay, it is particularly essential to mitigate the background. As the half life sensitivity of the SuperNEMO experiment is directly related to the background, it is vital to measure the background level accurately in situ. It is possible for any process that is capable of producing two electrons of high total energy close to $Q_{\beta\beta}$ (2.998 MeV for ^{82}Se) to mimic $0\nu 2\beta$ decay, and thus contribute to the background. These processes originate mainly from isotopes capable of emitting high energy electrons or photons, in the natural ^{238}U and ^{232}Th decay chains.

Simulation studies have been done to choose the best-suit topologies and variables to measure the main background. These variables are used to fit background contributions in a large number of pseudo-experiments in order to estimate the statistical and systematic uncertainties of different exposure times. In this chapter, the analysis strategy of characterising the background model of the SuperNEMO experiment is explained.

9.1 Radon as SuperNEMO Background

The signature of the $0\nu 2\beta$ event is two electrons with energies that add up to the total decay energy $Q_{\beta\beta}$. There is an irreducible background from the high-energy tail of the $2\nu 2\beta$. In addition, there are background events caused β -decaying isotopes: if the total energy released in a β decay is higher than the $Q_{\beta\beta}$ (2.99 MeV for the ^{82}Se used in this experiment), a second electron can be produced near the decay vertex via Møller or Compton scattering, or internal conversion, mimicking a $0\nu 2\beta$ decay. The β decay background mainly comes from two sources: ^{214}Bi , ^{208}Tl within the source foil, and radon in the tracker gas. ^{214}Bi and ^{208}Tl are both β decaying isotopes with Q_{β} values of 3.27 MeV and 4.99 MeV, from the natural ^{238}U and ^{232}Th decay chains, respectively, see Figure 9.1. Due to their high Q_{β} , their decay can mimic the $0\nu 2\beta$ signal, and experimentally this can be observed as a wide bump centred at 2.99 MeV ($Q_{\beta\beta}$ of ^{82}Se) when considering the energy resolution of the calorimeter, and the energy loss of the electron as it leaves the foil and travels through the detector. Radon (^{222}Rn) is a supply of ^{214}Bi due to its long half-life and diffusion properties as a noble gas. While several approaches have been applied to ensure the radiopurity of the detector, a tiny amount of radon may still be present within the detector. For this reason, it is essential to implement analysis tools for the identification and subsequent rejection of background events.

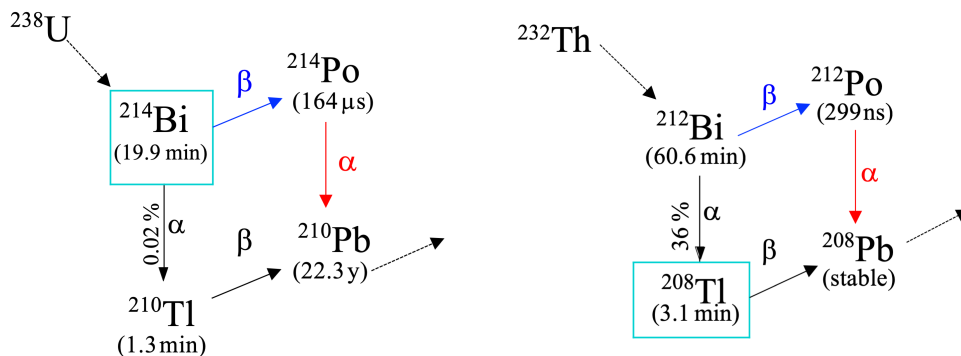


Figure 9.1: Beta decay of ^{214}Bi and ^{208}Tl are major backgrounds of $0\nu 2\beta$ searching experiments.

9.2 Radon Background Sensitivity Estimation

The background model of the experiment is built on the measurements of contributions from each part of the detector. The analysis is based on studying a large number of events with selected pure topology, which can provide an accurate determination of the contributions. The event of interest is the decay of ^{214}Bi nuclei on the field wire surface within the tracker volume. The ^{214}Bi contamination was measured by the delayed coincidence signature, where ^{214}Bi β -decays to ^{214}Po , and then ^{214}Po quickly to α -decays to ^{210}Pb .

9.2.1 Event Topology

One significant advantage of the SuperNEMO tracker-calorimeter design is its ability to provide full reconstruction of individual particle tracks in order to identify the event topologies, which offers useful information on measuring the background. The most interesting topology for the SuperNEMO experiment are: $2e$, $1e$, $1eN\gamma$, $2eN\gamma$, $1eN\alpha$ and, to a lesser extent $1e1p$ (one electron and one positron) [82]. Among them, the $1eN\alpha$ topology is one of the most important analysis channels to measure the background of the SuperNEMO experiment.

To estimate the ^{214}Bi background in the tracker, a clean channel needs to be found to measure the ^{214}Bi . The BiPo decay chain, where ^{214}Bi β -decays to ^{214}Po , and then quickly to α -decays to ^{210}Pb (half-life $164.3 \mu\text{s}$), can be a clear signal in the identification of ^{214}Bi background events. These events can also be associated with no gammas, corresponding to a standard BiPo event where ^{214}Bi decays to the ground state of ^{214}Po , or N gammas ($N > 0$), corresponding to ^{214}Bi decaying to an excited state of ^{214}Po with one or a cascade of gammas emitted, see Figure 9.1.

Since only ^{214}Bi events contribute to the $1e1\alpha$ topology, it would be one golden channel to measure the ^{214}Bi decay. The $1e1\alpha$ topology requires one electron track within an associated calorimeter, and one alpha track with at least one Gei-

ger hit. In addition, the vertex separation of the two particles should be less than 30 cm.

All events can be classified into two selections based on the position of the reconstructed event vertex: the tracker selection in which the vertex locates in the tracker volume, and the source selection in which the event vertex is extrapolated to the source foil. As Falaise extrapolates the track to the foil during reconstruction, it is impossible to distinguish events with a vertex in the first layer of tracker and events from the foil, (see Figure 9.2). The reconstructed vertex is at the end of the electron track by definition.

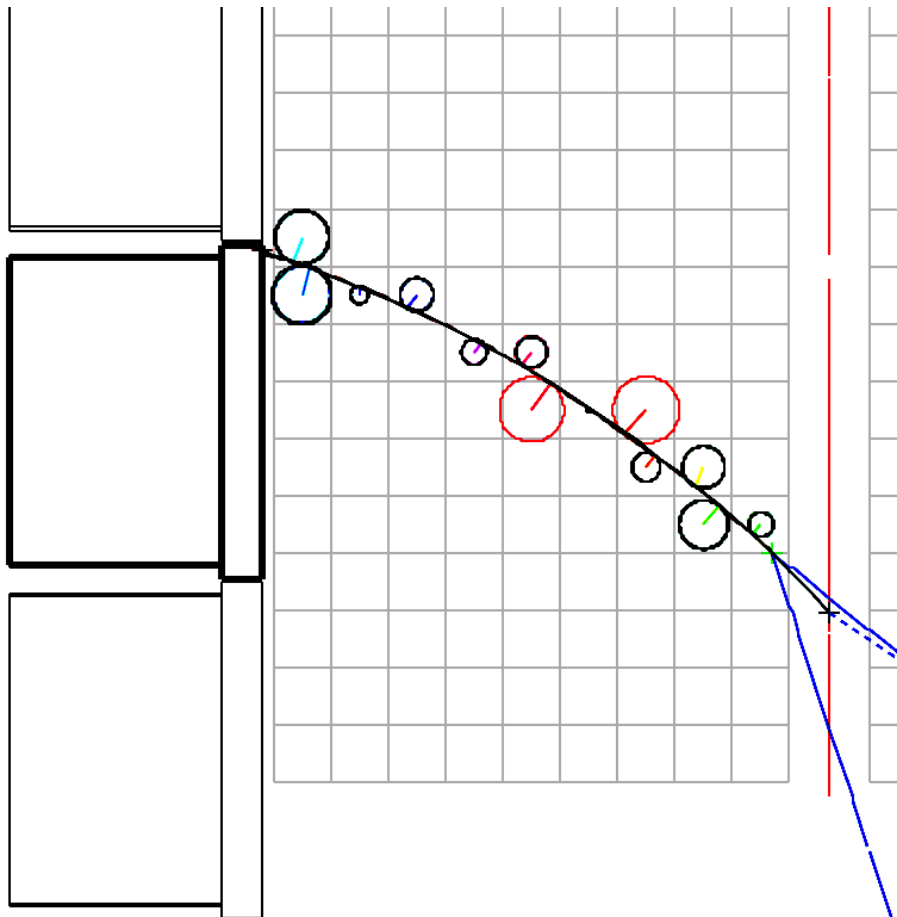


Figure 9.2: An event on the first layer of tracker was extrapolated to the foil during reconstruction, where the green cross is the true vertex and the black cross is the reconstructed vertex.

9.2.2 Event Number Estimation

The expected number of events N_i^{cut} depends on the activity A_i , detector acceptance and selection efficiency e_i^{cut} , and the exposure time T :

$$N_i^{cut} = e_i^{cut} \times A_i \times T \quad (9.1)$$

where i is the selection and can be either tracker or source selection, and the cut is normally made on topology which here is $1e1\alpha$.

9.2.3 Activity

The background of the source foil comes mainly from contamination of ^{214}Bi from the natural ^{238}U decay chain. The BiPo Detector [121] gives an upper limit of 4.94 mBq for the activity of Mylar, ^{82}Se source, and Polyvinyl acetate (PVA) in the source foils, and this value is used as the source foil bulk activity in the analysis. The BiPo detector was developed by the collaboration particularly to measure the impurities (^{214}Bi and ^{208}Tl contamination) in the source foils, where the foil is sandwiched by two thin layers of polystyrene scintillators and PMTs. C-Section Measurements using the RnCL have produced a tracker activity result of 41.3 ± 4.7 mBq without flushing. For the SuperNEMO Demonstrator, by flushing at $1 \text{ m}^3/\text{hr}$, a radon suppression factor of 9.71 can be achieved, as shown in Section 6.4. These result in the tracker activity (with flushing) decreasing to 4.25 ± 0.48 mBq, or 0.28 ± 0.07 mBq/ m^3 . Since the decay daughters of radon are positively charged, due to the electric field, positive ^{214}Bi ions in the tracker gas are attracted to the tracker field wires rather than to the anode wires. In addition, it is assumed that positive ^{214}Bi ions in the gap (between the foil and the tracker first layer) are deposited on the surface of the source foil.

The total activity in the tracker gas is then split into two parts based on the gap and tracker volume ratio: 7.8% of the positive ^{214}Bi ions as deposited on the source surface and the other 92.2% on wires, corresponding to an activity of 3.92

± 0.44 mBq from the tracker wires and 0.34 ± 0.04 mBq from the surface of the source foil. Since the Mylar used as the source foil cover in SuperNEMO is different from that used in NEMO3, it is unclear how much radon will stick to it in real-life operation. As such, it is necessary to test various methods of splitting radon activity between the source foil surface mylar and the tracker field wires. These activities are summarised in Table 9.1.

detector components	activity	measured by detector
^{214}Bi in source foil bulk	4.94 mBq (upper limit)	BiPo detector
^{214}Bi in source foil surface	0.34 ± 0.44 mBq	RnCL
^{208}Tl in field wire surface	3.92 ± 0.44 mBq	RnCL

Table 9.1: ^{214}Bi and ^{208}Tl activities in the detector region. Results are from external measurements measured by the RnCL or the BiPo detector [121].

9.2.4 Samples

The three samples used in this study are ^{214}Bi events of which vertices are simulated randomly in source foil bulk, on source foil surface, and the tracker field wire surface. Each sample contains 1E6 events. It should be noted that the ^{214}Bi events from source foil bulk are from the contamination in the foil, and the ^{214}Bi events from the source foil surface and the tracker field wire surface are from radon deposited on the surface areas. Two scenarios for the magnetic field are considered in the work of this thesis: 25 Gauss, and no field. Several cuts are applied to remove events from the data set if any of the following criteria is not satisfied:

- $1e1\alpha$ reconstructed topology requiring the event has only one electron, one alpha, and n gammas ($n \geq 0$). In addition, at least one Geiger hit of the alpha particle must be within 30-cm distance from the reconstructed vertex of the electron.
- An electron/positron candidate requires a reconstructed track with the as-

sociated calorimeter hit.

- Negative electron charge required for the 25 Gauss magnetic field scenario. No charge requirement for the no magnetic field scenario.
- An alpha candidate is defined by the delayed ($> 10 \mu\text{s}$) cluster of ≥ 1 tracker hit without associated calorimeter hit.
- Tracker selection, meaning the reconstructed event vertex should not be extrapolated to the source.

For the 25 Gauss magnetic field scenario, the magnetic field can bend electrons thus they can leave curved tracks, but not strong enough to bend alphas. Also, for high energy electrons ($> 2 \text{ MeV}$) the bend is often indistinguishable. The negative or positive charge of the electron or positron can be determined by the helices of the track (positive charge curved, negative charge curved, or straight). For the no magnetic field scenario, it is impossible to tell the charge of an electron/positron candidate which has a reconstructed track with the associated calorimeter hit. Thus all the candidates which have one reconstructed track and an associated calorimeter hit, are accepted as electrons. The SuperNEMO calorimeter has an instrumental energy threshold of 50 keV. The cut flow efficiencies are summarised in Table 9.2 to 9.7. In these table, 1 e and 1 α means the event has only 1 electron candidate, 1 alpha candidate and no extra track of other particle. And the $1e1\alpha$ topology has further requirement on the vertex separation of the electron and alpha particle to be a less than 30 cm.

9.2.5 Alpha Track Length Distribution

The SuperNEMO demonstrator detector can measure the background contributions independently from previous external measurements, such as the RnCL, Germanium detector, and BiPo detector measurements. Finding a suitable discriminating variable will be essential in enabling the measurement of background levels within the detector. The reconstructed alpha track length is chosen

events true vertex region	number of events	efficiency
≥ 1 calorimeter hit	849663	84.97%
≥ 1 reconstructed track	702078	70.21%
1 electron/positron candidate	451161	45.12%
1 e (negative charged)	404640	40.46%
1 e and ≥ 1 delayed tracker hit	37843	3.78%
1 e and 1 α (no other track)	27108	2.71%
1 e 1 α topology	20731	2.07%
1 e 1 α & electron vertex in tracker	656	0.07%

Table 9.2: 1 e 1 α channel cut flow of the selection efficiency for 25 Gauss magnetic field Tracker ^{214}Bi from source bulk. 1E6 events are generated for each component.

events true vertex region	number of events	efficiency
≥ 1 calorimeter hit	846445	84.64%
≥ 1 reconstructed track	783841	78.38%
1 electron/positron candidate	452729	45.27%
1 e (negative charged)	404187	40.42%
1 e and ≥ 1 delayed tracker hit	129185	12.92%
1 e and 1 α (no other track)	98591	9.86%
1 e 1 α topology	92569	9.26%
1 e 1 α & electron vertex in tracker	2251	0.23%

Table 9.3: 1 e 1 α channel cut flow of the selection efficiency for 25 Gauss magnetic field Tracker ^{214}Bi from source surface. 1E6 events are generated for each component.

events true vertex region	number of events	efficiency
≥ 1 calorimeter hit	849876	84.99%
≥ 1 reconstructed track	787558	78.76%
1 electron/positron candidate	398650	39.87%
1 e (negative charged)	299084	29.91%
1 e and ≥ 1 delayed tracker hit	157978	15.80%
1 e and 1 α (no other track)	80278	8.03%
1 e 1 α topology	72447	7.24%
1 e 1 α & electron vertex in tracker	54342	5.43%

Table 9.4: 1 e 1 α channel cut flow of the selection efficiency for 25 Gauss magnetic field Tracker ^{214}Bi from field wire surface. 1E6 events are generated for each component.

events true vertex region	number of events	efficiency
≥ 1 calorimeter hit	861045	86.10%
≥ 1 reconstructed track	712993	71.30%
1 electron candidate	497653	49.77%
1 e and ≥ 1 delayed tracker hit	46094	4.60%
1 e and 1 α (no other track)	34415	3.44%
1 e 1 α topology	26054	2.61%
1 e 1 α & electron vertex in tracker	534	0.05%

Table 9.5: 1 e 1 α channel cut flow of the selection efficiency for no magnetic field Tracker ^{214}Bi from source bulk. 1E6 events are generated for each component.

events true vertex region	number of events	efficiency
≥ 1 calorimeter hit	857906	85.79%
≥ 1 reconstructed track	788478	78.85%
1 electron candidate	486201	48.62%
1 e and ≥ 1 delayed tracker hit	155159	15.52%
1 e and 1 α (no other track)	122533	12.25%
1 e 1 α topology	115248	11.52%
1 e 1 α & electron vertex in tracker	1927	0.19%

Table 9.6: 1 e 1 α channel cut flow of the selection efficiency for no magnetic field Tracker ^{214}Bi from source surface. 1E6 events are generated for each component.

events true vertex region	number of events	efficiency
≥ 1 calorimeter hit	851205	85.12%
≥ 1 reconstructed track	786418	78.64%
1 electron candidate	401313	40.13%
1 e and ≥ 1 delayed tracker hit	209349	20.93%
1 e and 1 α (no other track)	112666	11.27%
1 e 1 α topology	98435	9.84%
1 e 1 α & electron vertex in tracker	75891	7.59%

Table 9.7: 1 e 1 α channel cut flow of the selection efficiency for no magnetic field Tracker ^{214}Bi from field wire surface. 1E6 events are generated for each component.

as the discriminating observable to distinguish the background events from different detector regions. Alpha particles emitted from the tracker wire surface do not need to travel through the dense source, in contrast to alphas within the source. For this reason, alphas emitted in the source bulk will lose some energy as they pass through the source material prior to detection by the tracker, resulting in shorter tracks than those by alphas emitted within the tracker. The alpha track length distribution of three different components are studied, as shown in Figure 9.3..

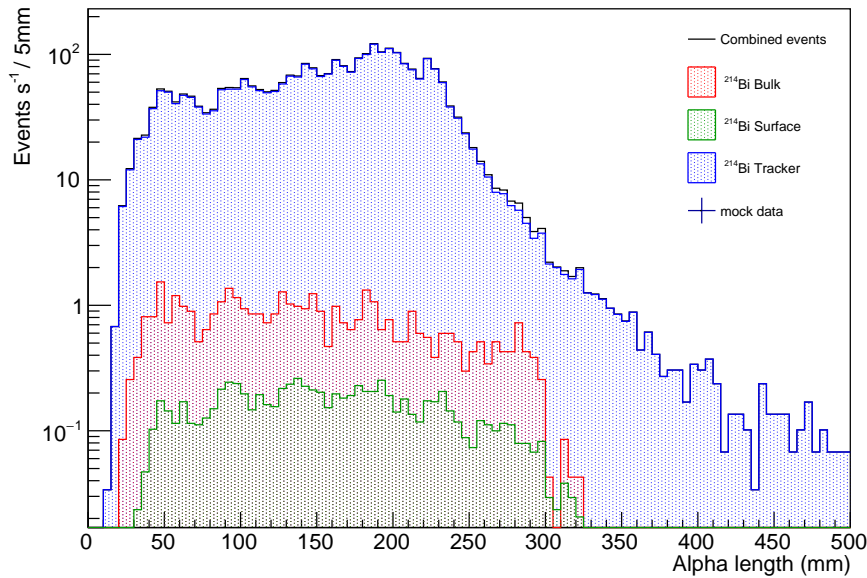


Figure 9.3: A Monte-Carlo simulation of α track length distributions from three locations of the ^{214}Bi background corresponding to 60 days of data taking.

The three distributions of alpha track lengths are normalised to their respective activities provided by external measurements. The alpha track length distribution can be further normalised to the specific exposure of a pseudo experiment to obtain a final distribution.

9.2.6 Pseudo-experiments

To identify how much data would be required to carry out a radon measurement in the tracker with a particular accuracy, 5% here, pseudo-experiments are generated from the final alpha track length distribution in order to provide datasets similar to what will be measured during real operation of the demonstrator detector. To mimic the real data, the number of expected events is a random number in accordance with the Poisson distribution. The pseudo-experiment datasets are fitted with the three distributions from the three components, using a binned normalisation fit to return the activity of each component. Here, we focus on events on the tracker field wire surface. An example of pseudo-experiment with the best fit is shown in Figure 9.4.

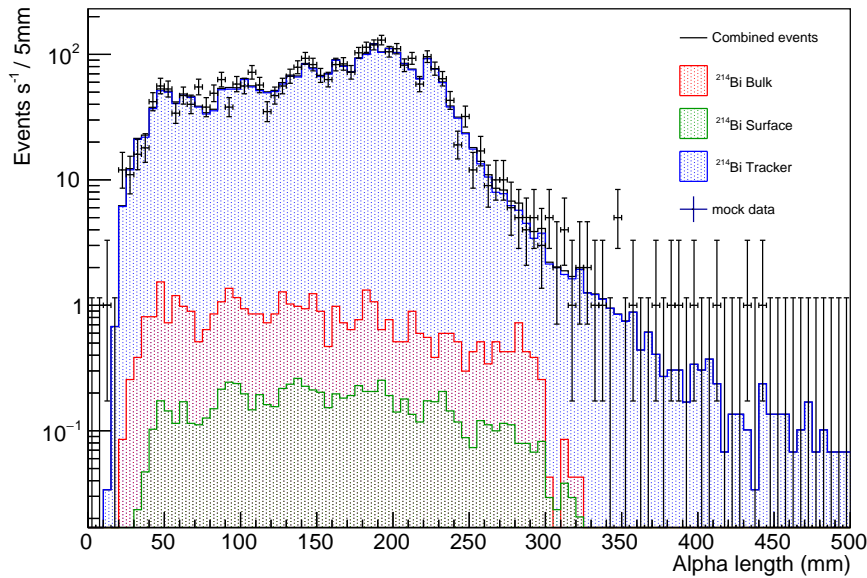


Figure 9.4: Data from a pseudo-experiment fitted with α track length distributions for $1e1\alpha$ events.

9.2.7 Activity Measurement

The pseudo experiment is repeated a large number times ($1E5$ times here), in order to evaluate the stability of the approach and determine the statistical uncertainty. The distribution of the activities measured for each pseudo-experiment, running for specific exposure times, are presented in Figure 9.5 for the ^{214}Bi component on the tracker field wire surface. The distributions of the measured ^{214}Bi activities on the field wire surface for each pseudo experiment are fitted with Gaussian functions, with one standard deviation taken as the uncertainty on the measurement. The mean ^{214}Bi activities are well within 1% of their expected values which are provided using inputs from independent measurements with external detectors such as the RnCL, the HPGe [43] and the BiPo detector.

9.2.8 Sensitivity Dependence on the Exposure Time

To investigate the evolution of the relative errors with time, the pseudo-experiments can be generated for various exposure times. For the tracker se-

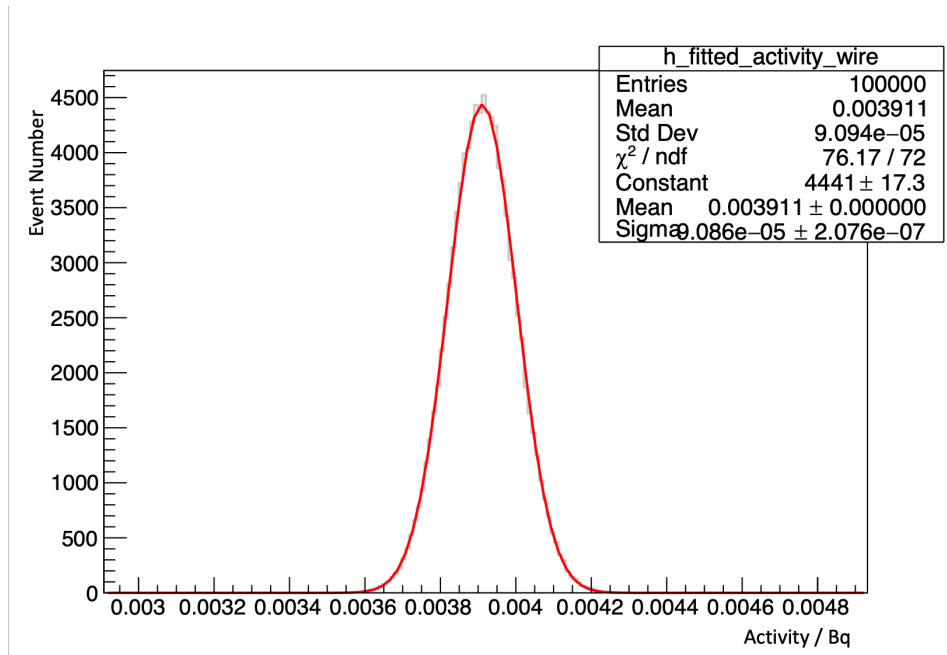


Figure 9.5: Distribution of the ^{214}Bi activities in the tracker measured from the pseudo-experiments (after 100 days measurement). The true value of the ^{214}Bi activities is 3.92 mBq.

lection, the relative error as a function of exposure time is shown in Figure 9.6, and Figure 9.7 for 25 Gauss magnetic field, and no magnetic field respectively.

Using the efficiency from the reconstruction of the $1e1\alpha$ channel and the externally measured activities of the detector components, the expected background level due to ^{222}Rn can be computed. The level of ^{222}Rn coming from the tracker can be determined at 5% after 12 days of measurement with magnetic field turned on or after 11 days of measurement without magnetic field; it can thus be measured reasonably quickly via the $1e1\alpha$ channel. The results do not show the necessity of the magnetic field for the radon background measurement; however, it can be very important for the measurement of $0\nu2\beta$ event. The influence of $0\nu2\beta$ event reconstruction with/without the magnetic field currently being studied by the collaboration.

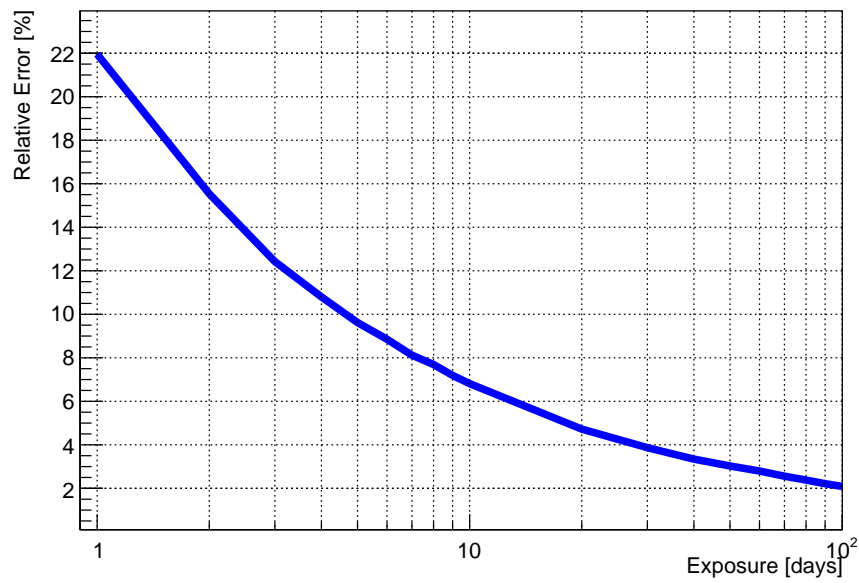


Figure 9.6: Relative error on the radon content measurement in the SuperNEMO tracker as a function of the exposure (measurement time) using $1e1\alpha$ channel for the case of a 25 Gauss magnetic field.

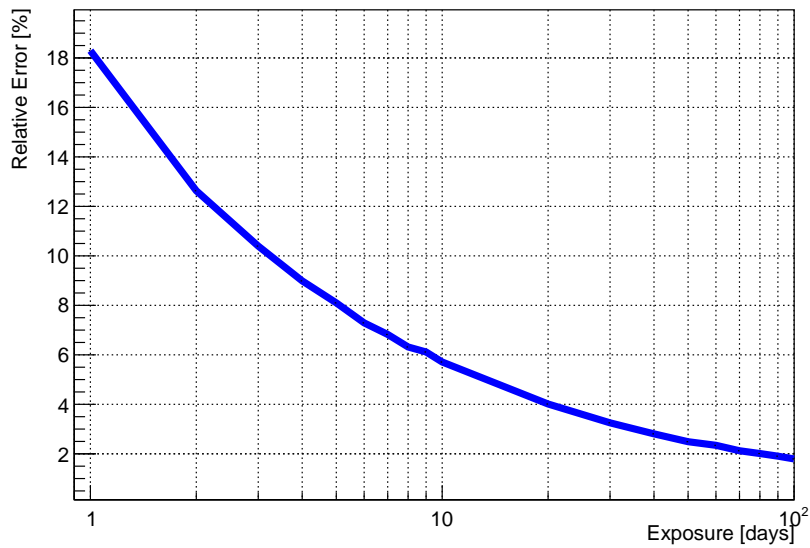


Figure 9.7: Relative error on the radon content measurement in the SuperNEMO tracker as a function of the exposure (measurement time) using $1e1\alpha$ channel for the case of no magnetic field.

Chapter 10

Conclusions

Neutrinoless double beta decay ($0\nu 2\beta$) is a hypothesised decay where two β decays occur simultaneously, emitting two electrons but no anti-neutrinos. It is clear that this process violates the lepton number and is thus forbidden in the SM. If this process were observed, it would imply the Majorana nature of the neutrino, and in addition, it allows the extraction of the absolute mass scale of the neutrino (model-dependently). Searching for $0\nu 2\beta$ is one of the highest priority items on the modern particle physics agenda. There is a range of experimental techniques currently employed and proposed to search for $0\nu 2\beta$.

SuperNEMO is a next-generation $0\nu 2\beta$ experiment capable of reaching a half-life sensitivity of $T_{1/2} > 10^{26}$ years, equivalent to an effective Majorana neutrino mass of $\langle m_{\beta} \rangle < 40 - 100$ meV. The baseline design of SuperNEMO envisages 20 identical planar modules, housing 100 kg of source isotope (^{82}Se) in total. The Demonstrator module, which is about to be commissioned at the Laboratoire Souterrain de Modane (LSM), will search for $0\nu 2\beta$ in 7 kg of ^{82}Se source with the aim of reaching zero background in the region of interest. Its unique tracker-calorimeter technology allows for the reconstruction of the 3D topology of the detected event, providing both a powerful background rejection method and evidence for the underlying decay process.

As the decay daughter of ^{222}Rn , ^{214}Bi contributes a large part to the background

due to their high β decay Q_{beta} values of 3.27 MeV and 4.99 MeV respectively. All materials are naturally contaminated with traces of the ^{232}Th and ^{238}U . Radon, as a highly diffusive radioactive gas with a relatively long half-life, can enter the SuperNEMO detector generally via emanation from the detector construction material and diffusion from the environment.

To achieve the target sensitivity of SuperNEMO, the activity of radon in the tracker activity needs to be $< 150 \mu\text{Bq}/\text{m}^3$, which has imposed a very challenging requirement on the radio-purity of the detector components, construction materials, and the tracker gas. Commercial detectors are not sensitive enough; therefore, a custom-made electrostatic detector was commissioned for SuperNEMO, which is capable of measuring radon down to a level of 1 -2 mBq/m³. The radon concentration line (RnCL) was developed to be used in conjunction with the electrostatic radon detector, which allowed for the measurement of ultra-low level activity of large gas volumes. The RnCL has demonstrated that it can achieve a sensitivity of $20 \mu\text{Bq}/\text{m}^3$ using 8.4 m^3 of gas which is the volume used for a typical quarter-tracker module radon measurement. A gas purification system called J-trap was used to provide carrier gas of ultra-low and stable radon contamination, for radon measurements.

Using the RnCL, three quarter-tracker modules have been measured for their radon emanation level before and after tracker wire cell installation. Measurements of radon emanation of detector components and construction materials were carried out to screen and select the cleanest possible materials for SuperNEMO, and to build up the background model based on measurements obtained from individual components. Two radon emanation chambers were used for radon emanation measurements of small samples. The sensitivity of chamber 1 and chamber 2 are $< 0.09 \text{ mBq}$ and $< 0.19 \text{ mBq}$ (at 90% CL) respectively. A number of samples have been measured for SuperNEMO as well as for the LZ experiment.

The demonstrator sensitivity to its radon backgrounds has been studied via

Monte Carlo simulations performed with the SuperNEMO software. Using the $1e1\alpha$ event topology, it is shown that the ^{214}Bi target contamination originating from radon (4 mBq in the tracker volume of 15 m^3) could be measured with a 5% precision within 12 days of data taking.

Bibliography

- [1] W. Pauli. Dear radioactive ladies and gentlemen. *Phys.Today*, 31N9:27, 1978.
- [2] E. Fermi. An attempt of a theory of beta radiation. *Z.Phys.*, 88:161–177, 1934.
- [3] H. Bethe and R. Peierls. The "Neutrino". *Nature*, 133:532, 1934.
- [4] C.L. Cowan, F. Reines, F. B. Harrison, H. W. Kruse, and A. D. McGuire. Detection of the free neutrino: A Confirmation. *Science*, 124:103–104, 1956.
- [5] R. Davis and D. S. Harmer. Attempt to Observe the Cl37 Ar37 Reaction Induced by Reactor Antineutrinos. *Bull. Am. Phys., Soc* 4:217, 1959.
- [6] E. J. Konopinski and H. M. Mahmoud. The Universal Fermi Interaction. *Phys. Rev.*, 92:1045–1049, 1953.
- [7] L. Grodzins M. Goldhaber and A. W. Sunyar. Helicity of neutrinos. *Phys. Rev.*, 109:1015–1017, Feb 1958.
- [8] University of Zurich. Standard Model. modified on 25 April 2015.
- [9] G. Aad et al. Observation of a new particle in the search for the standard model higgs boson with the atlas detector at the lhc. *Physics Letters B*, 716(1):1 – 29, 2012.
- [10] G. Danby et al. Observation of High-Energy Neutrino Reactions and the Existence of Two Kinds of Neutrinos. *Phys.Rev.Lett.*, 9:36–44, 1962.

- [11] S. Schael et al. Precision electroweak measurements on the Z resonance. *Phys.Rept.*, 427:257–454, 2006.
- [12] D. S. Harmer R. Davis and H. C. Hoffman. Search for neutrinos from the sun. *Phys.Rev.Lett.*, 20:1205–1209, 1968.
- [13] B. Pontecorvo. Mesonium and anti-mesonium. *Sov.Phys.JETP*, 6:429, 1957.
- [14] B. Pontecorvo. Inverse beta processes and nonconservation of lepton charge. *Sov.Phys.JETP*, 7:172–173, 1958.
- [15] Z. Maki, M. Nakagawa, and S. Sakata. Remarks on the unified model of elementary particles. *Prog.Theor.Phys.*, 28:870–880, 1962.
- [16] Q. R. Ahmad et al. Direct evidence for neutrino flavor transformation from neutral current interactions in the Sudbury Neutrino Observatory. *Phys.Rev.Lett.*, 89:011301, 2002.
- [17] A. B. Balantekin and F Loreti. Solar and supernova neutrino physics with sudbury neutrino observatory. *Phys. Rev. D*, 45:1059–1065, Feb 1992.
- [18] A.Yu. Smirnov. The MSW effect and matter effects in neutrino oscillations. *Phys. Scripta T*, 121:57–64, 2005.
- [19] J. Beringer et al. Review of Particle Physics (RPP). *Phys.Rev.*, D86:010001, 2012.
- [20] M. Tanabashi et al. Review of particle physics. *Phys. Rev. D*, 98:030001, Aug 2018.
- [21] E. Majorana. Theory of the Symmetry of Electrons and Positrons. *Nuovo Cim.*, 14:171–184, 1937.
- [22] S.F King. Neutrino mass models. *Rept. Prog. Phys.*, 67:107–158, 2004.
- [23] G. Racah. On the symmetry of particle and antiparticle. *Nuovo Cim.*, 14:322–328, 1937.

- [24] P.F. De Salas, S. Gariazzo, O. Mena, C.A. Ternes, and M. Tórtola. Neutrino Mass Ordering from Oscillations and Beyond: 2018 Status and Future Prospects. *Front. Astron. Space Sci.*, 5:36, 2018.
- [25] Zykure. Energy spectrum of tritium beta decay used by the KATRIN neutrino experiment. modified on 25 April 2012.
- [26] M. Aker et al. Improved upper limit on the neutrino mass from a direct kinematic method by katrin. *Phys. Rev. Lett.*, 123:221802, Nov 2019.
- [27] N. Aghanim et al. Planck 2018 results. VI. Cosmological parameters. 2018.
- [28] A. Gando et al. Search for majorana neutrinos near the inverted mass hierarchy region with kamland-zen. *Phys. Rev. Lett.*, 117:082503, Aug 2016.
- [29] Carlo Giunti. Light sterile neutrinos: Status and perspectives. *Nuclear Physics B*, 908:336 – 353, 2016. Neutrino Oscillations: Celebrating the Nobel Prize in Physics 2015.
- [30] B. Monreal and J. A. Formaggio. Relativistic cyclotron radiation detection of tritium decay electrons as a new technique for measuring the neutrino mass. *Phys. Rev. D*, 80:051301, Sep 2009.
- [31] J. E. Mott. *Search for double beta decay of ^{82}Se with the NEMO-3 detector and development of apparatus for low-level radon measurements for the SuperNEMO experiment.* PhD thesis, University College London, 2010.
- [32] S. Pascoli E. Previtali R. Saakyan K. Schaeffner A. Giuliani, J. J. Gomez Cadenas and S. Schoenert. Double Beta Decay APPEC Committee Report, 2019.
- [33] C.F.V. Weizsacker. Zur Theorie der Kernmassen. *Z.Phys.*, 96:431–458, 1935.
- [34] M. Goeppert-Mayer. Double beta-disintegration. *Phys.Rev.*, 48:512–516, 1935.

- [35] W. H. Furry. On transition probabilities in double beta-disintegration. *Phys. Rev.*, 56:1184–1193, Dec 1939.
- [36] H. Ejiri J. D. Vergados and F. Simkovic. Theory of Neutrinoless Double Beta Decay. *Rept.Prog.Phys.*, 75:106301, 2012.
- [37] H. Nishiura M. Doi, T. Kotani and E. Takasugi. DOUBLE BETA DECAY. *Prog.Theor.Phys.*, 69:602, 1983.
- [38] C.S. Aulakh and Rabindra N. Mohapatra. Neutrino as the Supersymmetric Partner of the Majoron. *Phys.Lett.*, B119:136, 1982.
- [39] M. Hirsch, H.V. Klapdor-Kleingrothaus, and S.G. Kovalenko. Supersymmetry and neutrinoless double beta decay. Osaka 1995, Weak and electromagnetic interactions in nuclei, 1995.
- [40] F. T. Avignone, S. R. Elliott, and J. Engel. Double Beta Decay, Majorana Neutrinos, and Neutrino Mass. *Rev.Mod.Phys.*, 80:481–516, 2008.
- [41] R. Arnold et al. Probing new physics models of neutrinoless double beta decay with supernemo. *Eur.Phys.J.*, C70:927–943, 2010.
- [42] J. Menéndez, A. Poves, E. Caurier, and F. Nowacki. Disassembling the nuclear matrix elements of the neutrinoless $\hat{I}^2\hat{I}^2$ decay. *Nuclear Physics A*, 818(3):139 – 151, 2009.
- [43] X. R. Liu. *Low background techniques for the SuperNEMO experiment*. PhD thesis, University College London, 2017.
- [44] J. Terasaki. Many-body correlations of quasiparticle random-phase approximation in nuclear matrix elements of neutrinoless double $-\beta$ decay. *Phys. Rev. C*, 91:034318, Mar 2015.
- [45] J. Barea and F. Iachello. Neutrinoless double- β decay in the microscopic interacting boson model. *Phys. Rev. C*, 79:044301, Apr 2009.

- [46] P. K. Rath et al. Uncertainties in nuclear transition matrix elements for neutrinoless $\beta\beta$ decay within the projected-Hartree-Fock-Bogoliubov model. *Phys. Rev. C*, 82:064310, Dec 2010.
- [47] T. R. Rodríguez and G. Martínez-Pinedo. Energy Density Functional Study of Nuclear Matrix Elements for Neutrinoless $\beta\beta$ Decay. *Phys. Rev. Lett.*, 105:252503, Dec 2010.
- [48] A. Smolnikov and P. Grabmayr. Conversion of experimental half-life to effective electron neutrino mass in decay. *Phys.Rev.*, C81:028502, 2010.
- [49] W. Rodejohann. Neutrinoless double beta decay and neutrino physics. *J.Phys.*, G39:124008, 2012.
- [50] Y. ALHASSID A. J. LANKFORD et al. An Assessment of the Deep Underground Science and Engineering Laboratory (DUSEL). *tech. rep.*, 2011.
- [51] M. Anderson et al. Measurement of the ^8B solar neutrino flux in SNO+ with very low backgrounds. *Phys. Rev. D*, 99:012012, Jan 2019.
- [52] H. V. Klapdor-Kleingrothaus et al. Latest results from the HEIDELBERG-MOSCOW double beta decay experiment. *The European Physical Journal A - Hadrons and Nuclei*, 12(2):147–154, Oct 2001.
- [53] C. E. Aalseth et al. Recent results of the IGEX 76Ge double-beta decay experiment. *Physics of Atomic Nuclei*, 63(7):1225–1228, Jul 2000.
- [54] C. Cuesta et al. Background Model for the Majorana Demonstrator. *Physics Procedia*, 61:821 – 827, 2015. 13th International Conference on Topics in Astroparticle and Underground Physics, TAUP 2013.
- [55] N. Abgrall et al. The large enriched germanium experiment for neutrinoless double beta decay (LEGEND). *AIP Conference Proceedings*, 1894(1):020027, 2017.

- [56] K. H. Ackermann et al. The Gerda experiment for the search of $0\nu\beta\beta$ decay in ^{76}Ge ", journal="The European Physical Journal C. 73(3):2330, Mar 2013.
- [57] M. Agostini et al. Improved Limit on Neutrinoless Double- β Decay of ^{76}Ge from GERDA Phase II. *Phys. Rev. Lett.*, 120:132503, Mar 2018.
- [58] N. Abgrall et al. The Majorana Demonstrator Neutrinoless Double-Beta Decay Experiment. *Adv. High Energy Phys.*, 2014:365432, 2014.
- [59] S. I. Alvis et al. Search for neutrinoless double- β decay in ^{76}Ge with 26 kg yr of exposure from the Majorana Demonstrator, collaboration = Majorana Collaboration. *Phys. Rev. C*, 100:025501, Aug 2019.
- [60] J. Ebert et al. Results of a search for neutrinoless double- β decay using the cobra demonstrator. *Phys. Rev. C*, 94:024603, Aug 2016.
- [61] J. R. Wilson. Double beta decay measurement with COBRA. *Nucl.Phys.Proc.Suppl.*, 221:313–316, 2011.
- [62] S. Junpei. Kamland-zen: Status and future. *Nuclear Physics B - Proceedings Supplements*, 237-238:28 – 30, 2013. Proceedings of the Neutrino Oscillation Workshop.
- [63] A. Gand et al. Limit on Decay of ^{136}Xe from the First Phase of KamLAND-Zen and Comparison with the Positive Claim in ^{76}Ge . *Phys.Rev.Lett.*, 110(6):062502, 2013.
- [64] A. Gando et al. Limits on Majoron-emitting double-beta decays of ^{136}Xe in the KamLAND-Zen experiment. *Phys.Rev.*, C86:021601, 2012.
- [65] A. Gando et al. Limits on majoron-emitting double- β decays of ^{136}Xe in the kamland-zen experiment. *Phys. Rev. C*, 86:021601, Aug 2012.
- [66] A. BiaÅek et al. A rope-net support system for the liquid scintillator detector for the sno+ experiment. *Nuclear Instruments and Methods in Physics Research Section A Accelerators Spectrometers Detectors and Associated Equipment*, 827:152–160, 08.

- [67] J. R. Wilson. Non-accelerator Neutrino Physics. IoP HEPP & APP Group Meeting, 2013.
- [68] I. Ogawa R. Hazama S. Umehara, T. Kishimoto, H. Miyawaki, et al. Neutrino-less double-beta decay of ^{48}Ca studied by $\text{CaF}_2(\text{Eu})$ scintillators. *Phys.Rev.*, C78:058501, 2008.
- [69] M. Nomachi S. Yoshida K. Matsuoka S. Umehara, T. Kishimoto et al. Search for neutrino-less double beta decay with CANDLES. *AIP Conf.Proc.*, 1441:448–450, 2012.
- [70] D. Poda and A. Giuliani. Low background techniques in bolometers for double-beta decay search. *International Journal of Modern Physics A*, 32(30):1743012, 2017.
- [71] F. Avignone E. Andreotti, C. Arnaboldi et al. ^{130}Te Neutrinoless Double-Beta Decay with CUORICINO. *Astropart.Phys.*, 34:822–831, 2011.
- [72] C. Alduino et al. First results from cuore: A search for lepton number violation via $0\nu\beta\beta$ decay of ^{130}Te . *Phys. Rev. Lett.*, 120:132501, Mar 2018.
- [73] O. Azzolini et al. Final Result of CUPID-0 Phase-I in the Search for the ^{82}Se Neutrinoless Double- β Decay. *Phys. Rev. Lett.*, 123:032501, Jul 2019.
- [74] E. Armengaud et al. The cupid-mo experiment for neutrinoless double-beta decay: performance and prospects. *The European Physical Journal C*, 80:44, 01 2020.
- [75] J. B. Albert et al. Searches for double beta decay of ^{134}Xe with EXO-200. *Phys. Rev. D*, 96:092001, Nov 2017.
- [76] J. B. Albert et al. Search for neutrinoless double-beta decay with the upgraded exo-200 detector. *Phys. Rev. Lett.*, 120:072701, Feb 2018.
- [77] S. Al Kharusi et al. nexo pre-conceptual design report, 2018.

- [78] J. Martín-Albo et al. Sensitivity of NEXT-100 to neutrinoless double beta decay. *Journal of High Energy Physics*, 2016(5):159, May 2016.
- [79] L. Simard. The NEMO-3 results after completion of data taking. *J.Phys.Conf.Ser.*, 375:042011, 2012.
- [80] R. Saakyan. Tracking-based Experiments in Double Beta Decay. *Nucl.Phys.Proc.Suppl.*, 229-232:135–140, 2012.
- [81] H. Gómez and SuperNEMO Collaboration. Bipo: A dedicated radiopurity detector for the supernemo experiment. *AIP Conference Proceedings*, 1549(1):94–97, 2013.
- [82] S. Calvez. *Development of reconstruction tools and sensitivity of the SuperNEMO demonstrator*. PhD thesis, l'Université Paris-Saclay préparée à l'Université Paris-Sud, 2017.
- [83] A. D. Frad. Low Radioactivity and Multidisciplinary Underground Laboratory of Modane (LSM). May 2016. paper presented, Low Radioactivity Techniques 2017, Seoul, Korea.
- [84] C. Bourgeois. Shielding Design. *Internal Note*, DocDB:4878, 2019.
- [85] <https://github.com/supernemo-dbd/homebrew-cadfael>.
- [86] <https://github.com/bxcppdev/bayeux>.
- [87] <http://doc.qt.io/qt-5/>.
- [88] <http://www.boost.org>.
- [89] <https://root.cern.ch/>.
- [90] <https://github.com/tegesoft/camp>.
- [91] <http://proj-clhep.web.cern.ch/proj-clhep>.
- [92] <http://xerces.apache.org/xerces-c>.

- [93] <http://geant4.cern.ch>.
- [94] <http://www.stack.nl/~dimitri/doxygen/>.
- [95] <http://doc.qt.io/qt-5/>.
- [96] V. I. Tretyak O. A. Ponkratenko and Yu. G. Zdesenko. Event generator DECAY4 for simulating double-beta processes and decays of radioactive nuclei. *Physics of Atomic Nuclei*, 63(7):1282–1287, Jul 2000.
- [97] <https://github.com/supernemo-dbd/sensitivitymodule>.
- [98] J. R. Partington. Discovery of Radon. *Nature*, 179:912, 1957.
- [99] W. Ramsay and J. N. Collie. The Spectrum of the Radium Emanation. *Proc.Roy.Soc.Lond.*, 73:470–476, 1904.
- [100] W. Ramsay and R. Whytlaw-Gray. La densité de l'émanation du Radium. *Comptes rendus hebdomadaires des séances de l'Académie de Sciences*, 151:126–128, 1910.
- [101] Tosaka. Uranium Decay chain. modified on 21 November 2014.
- [102] Tosaka. Thorium Decay chain. modified on 15 October 2009.
- [103] Public Health England. Uk national radon action plan: response to public consultation. *PHE publications*, Gateway number:GW-286, 04 2019.
- [104] V. Vasiliev. Radon in SuperNEMO. *Internal Note*, DocDB:297, 2008.
- [105] S. De Capua and P. Guzowski. Flow rate study. *Internal Note*, DocDB:3146, 2014.
- [106] E. Choi et al. Highly sensitive radon monitor and radon emanation rates for detector components. *Nucl.Instrum.Meth.*, A459:177–181, 2001.
- [107] C. Mitsuda et al. Development of super-high sensitivity radon detector for the Super-Kamiokande detector. *Nucl.Instrum.Meth.*, A497:414–428, 2003.

- [108] E.M. Wellisch. The distribution of the active deposit of radium in an electric field. *Philosophical Magazine Series 6*, 26(154):623–635, 1913.
- [109] P. Pagelkopf and J. Porstendörfer. Neutralisation rate and the fraction of the positive ^{218}Po -clusters in air. *Atmospheric Environment*, 37(8):1057 – 1064, 2003.
- [110] P K Hopke. The initial atmospheric behavior of radon decay products. *Journal of Radioanalytical and Nuclear Chemistry*, 203:353–375, 1996.
- [111] G. F. Knoll. Radiation Detection and Measurement. ISBN-9780470131480, 2000.
- [112] X. R. Liu. Radio-purity Strategy for the SuperNEMO Experiment. *Internal Note*, DocDB:3986, 2016.
- [113] B Freudiger M Laubenstein M Balata T Kirsten G Heusser, W Rau. ^{222}Rn detection at the range in nitrogen gas and a new Rn purification technique for liquid nitrogen. *Applied Radiation and Isotopes*, 52(3):691 – 695, 2000.
- [114] J. Busto. Design of a Preliminary Anti-Radon System. *Internal Note*, DocDB:3117, 2014.
- [115] J. E. Mott. First radon measurements of C0, Internal SuperNEMO Technical Report. *Internal Note*, DocDB:2957, 2013.
- [116] X. R. Liu. Ultra-low level radon assays in gases. *AIP Conference Proceedings*, 1672(1):070002, 2015.
- [117] X. R. Liu. Gas System Radon Emanation Measurement. *Internal Note*, DocDB:4161, 2016.
- [118] B. Soule. Emanation Setup Status and 5 Inch PMT Measurements. *Internal Note*, DocDB:3270, 2014.
- [119] X. R. Liu. Gas Measurement Using Radon Purification System. *Internal Note*, DocDB:3593, 2014.

- [120] X. R. Liu. First Complete C-Section Measurement. *Internal Note*, DocDB:3579, 2015.
- [121] S. Cebrian. The BiPo detector. *Internal Note*, DocDB:894, 2009.